Dark Energy and Growth of Structure in Modified-Gravity Theories

by

Yuewei Wen

A dissertation submitted in partial fulfillment
of the requirements for the degree of
Doctor of Philosophy
(Physics)
in the University of Michigan
2023

Doctoral Committee:

Professor Dragan Huterer, Chair
Professor Fred C. Adams
Professor Lia Corrales
Professor G. Scott Watson

Yuewei Wen

ywwen@umich.edu

ORCID iD: 0000-0003-2579-7039

ACKNOWLEDGEMENTS

I am greatly grateful for all the support, help and love I have received during graduate school. The past five years have been a transformative experience — I have learned, grown and gained a lot, been at critical junctures of life and made important decisions.

I would like to express special thanks to my advisor, Dragan Huterer for being a role model in his most serious and dedicated attitude towards research, for his patience and support throughout grad school, and for his mentorship and the fostering of professional growth. Many thanks to my office mates, my colleagues in the cosmology group, my cohorts, and the Department of Physics. I am thankful for the support and resources from the Student Service Office, the Leinweber Center for Theoretical Physics, and the LSA Technology Services.

When I arrived at Ann Arbor on a summer night in 2018, I was by myself and hardly knew anyone here. Five years later, Michigan feels like home to me. A huge thank you to Runxue Yu who is always there for me through all the happy and sad days of grad school. Thank you to Ziyi Zhang and Yichuan Song for all the happy moments we spent together as roommates and for lightening up my days even after you graduated and are half a world away. Thank you to Thu Le for your company, especially during the difficult and isolated days under COVID. And many many love and thanks to all my friends and family who accompanied me through this sometimes bumpy journey — I would have been so lost and definitely not where I am without you all.

PREFACE

This dissertaion is based on the research I conducted between 2019 and 2023 at the University of Michigan. It includes three works that I led or contributed to. All of them are either published in or submitted to academic journals.

Chapter 2 is based on Ref. [211], a work done in collaboration with Eva Nesbit, Dragan Huterer and Scott Watson. It has been published on *Journal of Cosmology and Astroparticle Physics*.

Chapter 3 is based on Ref. [149] in which I collaborated with Nhat-Minh Nguyen and Dragan Huterer. It has been submitted to *Physical Review Letter*.

Chapter 4 is based on Ref. [212], a work co-led by Nhat-Minh Nguyen and in collaboration with Dragan Huterer. This work has been submitted to *Journal of Cosmology and Astroparticle Physics*.

TABLE OF CONTENTS

LIST OF FIGURES

FIGURE

LIST OF TABLES

TABLE

LIST OF APPENDICES

ABSTRACT

The past two decades have witnessed the emergence and flourishing of precision cosmology. Vast amount of high-quality observational data, especially those of the large scale structure and the cosmic microwave background, have been taken and analyzed. Rich information of the history, composition and structure of the Universe is still to be mined from them. Higher resolution surveys, larger coverage of the sky, better modeling of systematics, incorporation of more mature statistical and numerical tools — all of those have laid the foundation for a data-driven investigation of fundamental questions, in particular the crucial one of dark energy. What gives rise to the late-time accelerated expansion of the Universe? In this dissertation, we investigate different ways to make use of the present very-rich observational resources to probe proposed dark energy models and modifications to general relativity that incorporate a late-time cosmic acceleration.

We first present a quantitative study of the question: if modifications to general relativity are (mis-)interpreted as a phenomenological dark energy model, how will this bias our cosmological analysis results? We develop, for the first time to our knowledge, a quantitative schematic to address this question and find that modified gravity models masquerading as standard gravity can lead to very specific biases in standard-parameter spaces.

In the next study, we present evidence showing that growth of structure is suppressed at late times. Constraining the "growth index" γ that parameterizes the linear growth rate of matter density perturbations through $f(z) = \Omega_M(z)^\gamma$ with the cosmic microwave background data from Planck and the large-scale structure data from weak lensing, galaxy clustering, and cosmic velocities, we find that data favors a value of γ 3.7σ higher than the $\gamma = 0.55$ prediction from general relativity assuming a flat ΛCDM cosmology.

In the third work, we present a new parameterization of the linear growth rate for the Horndeski class of modified-gravity theories by generalizing the constant γ parameterization into a two-parameter redshift-dependent one. The new parameterization $\gamma(z) = \gamma_0 + \gamma_1 z^2/(1+z)$ is validated assuming stringent constraints from Stage IV and V large-scale structure surveys and is shown to improve the median χ^2 of the fit to viable Horndeski models by a factor of ~ 40 relative to that of a constant γ.

CHAPTER 1

Introduction

The present epoch is undoubtedly the age of precision cosmology. Over the period of a few decades, observations are able to reach far back into the early Universe up to a redshift of $z \simeq 10$; concordance cosmology has been established and can describe the Universe almost immediately after the Big Bang; constraints on key cosmological parameters are tightened more and more by each generation of cosmological surveys. Without exhausting the list of major achievements, one can still confidently conclude that enormous progress has been made in the field of cosmology.

The replacement of photographic plates with CCD cameras since the 1980s hugely improved the sensitivity of telescopes when capturing incident light; rapid developments in astronomy beyond the visible band made possible research into earlier periods and more diverse physical processes; the famous Hubble Space Telescope unprecedentedly probed the high redshift Universe and made contributions in measuring the Hubble constant; vast amount of data for a diverse set of cosmological probes have been acquired and analyzed as real advances are made in data science and computational tools [205]. Next generation of cosmological surveys, such as Stage-IV cosmic microwave background or Dark Energy Spectroscopic Instrument (DESI), will provide even richer data and tighter constraints on cosmological parameters.

It is within this broad context that the work in this dissertation is carried out. The advances in precision cosmology and the optimistic forecasts from future surveys have provided the basis for a data-driven investigation into the vast space of potential new physics, especially the open question of the physical nature of dark energy. This dissertation includes work using current and future surveys of dark energy and cosmic growth to study their implications on classes of modified-gravity theories that incorporated the effects of dark energy and to test the concordance cosmological model.

1.1 Fundamentals

Discovery of the accelerated expansion of the Universe in the late 1990s is a critical juncture in the development of cosmology. This observed acceleration requires the introduction of a new and strongly negative-pressured component into the concordance cosmological model, but the physical nature of it, which is not included in Einstein's theory of general relativity, remains unknown up till today.

1.1.1 Friedmann Equations

In general relativity, Einstein's field equations are

$$R_{\mu\nu} - \frac{1}{2}Rg_{\mu\nu} = 8\pi G T_{\mu\nu}, \tag{1.1}$$

where $R_{\mu\nu}$ and R are respectively the Ricci tensor and the Ricci scalar describing spacetime curvature, G is the gravitational constant, $T_{\mu\nu}$ is the energy-momentum tensor and $g_{\mu\nu}$ is the metric tensor that determines distance and geometry of spacetime. Assuming a homogenous and isotropic Universe, solution to Einstein's equations, namely the Friedmann–Robertson–Walker (FRW) metric is

$$ds^2 = -dt^2 + a^2(t)R_0^2\left[\frac{dr^2}{1-kr^2} + r^2 d\Omega^2\right], \tag{1.2}$$

where $a = 1/(1+z)$ is the scale factor and k is the curvature parameter. Under this metric, the equations of motion, also known as the Friedmann equations, are

$$H^2 \equiv \left(\frac{\dot{a}}{a}\right)^2 = \frac{8\pi G}{3}\rho - \frac{k}{a^2 R_0^2} \tag{1.3}$$

$$\frac{\ddot{a}}{a} = -\frac{4\pi G}{3}(\rho + 3p). \tag{1.4}$$

A static solution requires $\dot{a} = 0$ in the first Friedmann equation, which can be achieved by setting the curvature k to be positive. However, in the second Friedmann equation, $\ddot{a}$ cannot be zero when both the energy density ρ and the pressure p are positive. Therefore, to produce a truly static Universe, Einstein introduced an extra term into Eq. 1.1 and modified it to be,

$$R_{\mu\nu} - \frac{1}{2}Rg_{\mu\nu} + \Lambda g_{\mu\nu} = 8\pi G T_{\mu\nu}. \tag{1.5}$$

The new free parameter Λ is the cosmological constant, first introduced not for the presence of dark energy but to impose a static cosmological solution to Einstein's field equations. After adding the Λ term, the second Friedmann equation (Eq.1.4) now becomes

$$\frac{\ddot{a}}{a} = -\frac{4\pi G}{3}(\rho + 3p) + \frac{\Lambda}{3}. \tag{1.6}$$

In this case, $\ddot{a} = 0$ is now possible even when ρ and p are both positive.

Later in 1929 when observations confirmed the expansion of the Universe [103], the cosmological constant became unnecessary in the field equations because the Universe is not static. However, this concept was not immediately abandoned but remained of interest to physicists because of its connection to the vacuum energy — the zero point energy in a quantum vacuum. The cosmological constant, having a dimension of length^{-2}, can be interpreted as the energy density of the vacuum, a perfect fluid with $p_{\rm vac} = -\rho_{\rm vac}$. The equation of state w of a given fluid is defined as the ratio between its pressure and density. In this way, the cosmological constant or the vacuum energy has an equation of state $w \equiv p/\rho = -1$.

1.1.2 Hubble's Law

As early as 1929, astronomer Edwin Hubble found a linear correlation between the redshift and distance of a group of galaxies. This relation is known as the Hubble's Law:

$$z = \frac{H_0}{c} r, \tag{1.7}$$

where c is the speed of light and H_0 is the Hubble's constant. If we employ the non-relativistic Doppler shift of $z = v/c$ where v is the radial velocity of an observed galaxy, Hubble's Law can also be interpreted as a relationship between a galaxy's velocity and distance

$$v = H_0 r. \tag{1.8}$$

Hubble found that almost all galaxies are receding from us, and as Eq. 1.8 indicates, the farther a galaxy is, the faster it is moving away from us. From here, Hubble concluded that our Universe undergoes an expansion, and the Hubble constant H_0 indicates the rate of this expansion today.

While spectroscopic techniques used to measure redshift was relatively well-developed back then, determining distances has always been a crucial and difficult question in astronomy even today, let alone during Hubble's time [181]. What Hubble used was Cephaids, a kind of pulsating stars whose luminosity can be inferred from their pulsation period, known as the Leavitt Law, named after the American astronomer Henrietta Leavitt [106].

The famously wrong value of the Hubble constant he arrived at is $H_0 = 500$ km s^{-1} Mpc^{-1}, about seven times larger than the currently accepted value of $H_0 \simeq 70$ km s^{-1} Mpc^{-1} [181]. The $\simeq$ sign indicates that we have not completely pinned down the value of H_0 today, and one main issue to be resolved is the Hubble tension — a statistically significant 4σ to 6σ disagreement between measurements from cosmic microwave background surveys and type Ia supernovae surveys. As the former favors a lower value (e.g. $H_0 = 67.4 \pm 0.5$ km s^{-1} Mpc^{-1} from Planck 2018 analysis [13]), the latter concludes a higher value (H_0 = 73.30 ± 1.04 km s^{-1} Mpc^{-1} from SH0ES collaboration in 2021 [173]). What contributes to the Hubble tension remains an open question and hot topic in cosmology, with potential solutions ranging from new physics to poorly modeled systematics. A comprehensive review of proposed solutions to the Hubble tension can be found, for example, in [73].

1.1.3 Discovery of Dark Energy

More precise measurements of distances of galaxies were made possible through the development of the distance ladder, especially after the introduction of type Ia supernovae (SNe Ia) as the "standard candles" in measuring extragalactic distances. SNe Ia are products of explosions of white dwarfs when their masses reach the Chandrasekhar limit (1.44 $M_\odot$). As a result, luminosities of type Ia supernovae events are known quantities and are near uniform.

However, a number of challenges still need to be overcome before SNe Ia can be effectively employed in distance measurements.

One obstacle has been the scarcity of well-measured supernovae events. These events are highly unpredictable, making it diffcult to prepare for follow-up observations in advance. This was addressed by the Calan/Tololo Supernova Search (CTSS) program that started in 1990. Through scanning across 25 fields twice a month over the course of three and a half years, the CTSS was able to obtain a high quality pool of 30 new supernovae light curves [161].

Another issue that has been resolved in the early 1990s is calibrating the intrinsic luminosity of SNe Ia. Their luminosities are nearly uniform, but not completely the same. Astronomer Mark Phillips discovered in 1993 that the decay time of a supernova's light curve, or equivalently its width, is strongly correlated with its luminosity, raising the precision of luminosity distance measurement to ~10% [163]. Later in the decade, various other methods in quantifying the luminosity of a supernova even were developed as well, including the multi-color light curve shape method (MLCS) from Riess et al. [174] and the "stretch method" from Perlmutter et al. [159, 160].

Equipped with the techno and scientific capability to accurately measure our distances to a set of galaxies through observing the lightcurves of a large number of SNe Ia, the Supernova Cosmology Project and the High z Supernova Search Team independently discovered in 1998 and 1999 that the more distant galaxies are, the more they would deviate from the linear relation predicted by Hubble's Law. In other words, objects that are further away are moving faster and the Universe is thus accelerating in its expansion. Later surveys from different probes — especially measurements of the cosmic microwave background (CMB) and baryon acoustic oscillations (BAO) — have also showed strong evidence for cosmic acceleration.

The observed accelerated expansion at late times is incompatible with a matter-only Universe

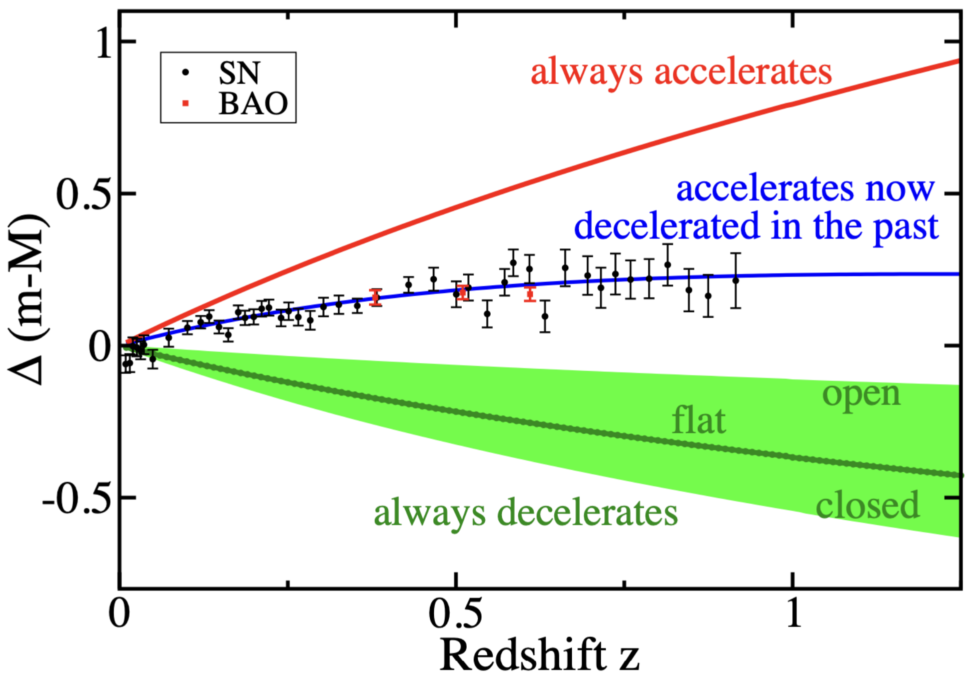

Figure 1.1: Distance modulus versus redshift. The black data points are from 870 SNe Ia [76]. The red data points are from baryon acoustic oscillations (BAO) measurements [15]. The colored curves are distances predicted by cosmological models of different expansion history. The red curve represents a Universe that has always been accelerating, the black one a Universe that always decelerates and the blue one a Universe that decelerated in the past but accelerates in later. The green shade surrounding the black curve represents a range of matter densities, $0.3 \leq \Omega_M \leq 1.5$, that encompasses different kinds of geometry of the Universe. Adopted from [109].

regardless of the value of matter density, indicating the need for a new negative-pressure component, namely the dark energy. Figure 1.1 further illustrates this point by contrasting SNe Ia data [76] with various cosmological models. Plotting the distance modulus (introduced in Eq. 1.12) of each supernova against its redshift, the SNe Ia data clearly favor an expansion history where the Universe decelerated in the past but accelerates now. It is also demonstrated in this figure that a matter-only Universe that always decelerates in its expansion, regardless of matter density and geometry, is ruled out. Current data favor a composition of the Universe of ~30% matter and ~70% dark energy.

The presence of a negative pressure component is required for realizing late-time cosmic acceleration, which means $\ddot{a} > 0$ in the second Friedmann equation. The cosmological constant with a negative equation of state ($w = -1$) is naturally re-introduced into Einstein's field equations as the candidate for dark energy. However, the energy scale of vacuum energy from quantum fluctuations, as predicted in particle physics, is about 120 orders of magnitude larger than what is necessary to explain the acceleration in expansion rate and to yield a flat geometry in late times [106], motivating alternative explanations to what dark energy really is.

Due to the lack of an established theoretical model for dark energy, parameterization of the dark energy component becomes crucial in observational work. The parameter space of dark energy usually has two key components, $\{\Omega_{\mathrm{DE}}, w\}$. The former is the energy density of dark energy relative to the critical density, defined as

$$\Omega_{\mathrm{DE}} = \frac{\rho_{\mathrm{DE},0}}{\rho_{\mathrm{crit},0}} = \frac{\rho_{\mathrm{DE},0}}{3H_0^2/(8\pi G)}. \tag{1.9}$$

And the latter is the previously defined equation of state of dark energy. Constraints from the second Friedmann equation ($\ddot{a} > 0$ for an accelerated expansion) require $w < -1/3$. Analysis from most current observations gives $w \simeq -1$, which indicates a component similar to the cosmological constant.

If we take into consideration that the dark energy component can have time variations, the most commonly accepted two-parameter parameterization of the equation of state is

$$w(z) = w_0 + w_a \frac{z}{1+z} = w_0 + w_a(1-a). \tag{1.10}$$

The major advantage of this parameterization is that it not only reduces to $w = w_0$ as $z \to 0$, but also plateaus to a finite upper bound as $z \to \infty$, avoiding any unphysical behaviors at high redshift.

1.1.4 Cosmological Probes of Dark Energy

Despite the lack of theoretical explanation for the physical nature of dark energy, over the past two decades, major progress has been made in measuring the property of dark energy and constraining dark energy parameters. We will give an overview in this section of main cosmological probes for dark energy, with an emphasis on the ones used in the works in included in this dissertation.

1.1.4.1 Type Ia Supernova (SNe Ia)

For a given bright object, its flux f and luminosity L follows the relation

$$f = \frac{L}{4\pi d_L^2}, \tag{1.11}$$

where d_L is the luminosity distance. If we have knowledge of both the flux and the luminosity, we can determine distance through Eq. 1.11. Flux, or how much light is received by Earth, is easily measurable, but the intrinsic luminosity, or how much light the object emits, is difficult to determine. This explains the need for standard candles (SNe Ia), whose instrinsic luminosity is known or can be effectively calibrated.

In practice, astronomers measure flux and luminosity in quantities known as the apparent magnitude m and the absolute magnitude M, and an often quoted quantity is the difference between the two, the distance modulus

$$m - M \equiv 5 \log_{10} \left(\frac{d_L}{10\,\mathrm{pc}} \right). \tag{1.12}$$

In cosmology with SNe Ia, the distance modulus is often written in the following form [106] with a nuisance parameter $\mathcal{M}$,

$$m = 5 \log_{10}(H_0 d_L) + \mathcal{M}, \tag{1.13}$$

where

$$\mathcal{M} = M - 5 \log_{10}(H_0 \times 1\,\mathrm{Mpc}) + 25. \tag{1.14}$$

Without knowledge of quantities entering $\mathcal{M}$ (i.e. the absolute magnitude M and the Hubble constant H_0), SNe Ia provides measurement of relative distances and in current surveys, $\mathcal{M}$ can be pinned down through Cephaids. What measurements of SNe Ia constrain is the luminosity distance d_L

$$H_0 d_L = (1 + z) r(z). \tag{1.15}$$

The $r(z)$ is the comoving distance sensitive to cosmological parameters:

$$r(z) = \frac{\sinh \sqrt{|\Omega_K|}}{\sqrt{|\Omega_K|}} \int_0^z \frac{dz'}{\sqrt{\Omega_M (1+z')^3 + \Omega_{\mathrm{DE}} (1+z')^{3(1+w)} + \Omega_R (1+z')^4 - \Omega_K (1+z')^2}}, \tag{1.16}$$

where Ω_K, Ω_M, Ω_{DE}, and Ω_R are the respective density parameters of curvature, matter, dark energy and radiation, defined in a similar way to Eq. 1.9.

One of the latest SNe Ia data sets is the Pantheon+ Analysis [191]. It contains 1701 light curves of 1550 unique SNe Ia that are spectroscopically confirmed. Figure 1.2 shows the redshift coverage of the collected SNe Ia samples. Compared to previous data sets, major improvements have been made in enriching the low-redshift region. Constraints on cosmological and dark energy parameters from the Pantheon+ data set, assuming a flat universe and a constant dark energy equation of state, is $w_0 = -0.90 \pm 0.14$ [49], consistent with a ΛCDM cosmology. When time variation of dark energy is incorporated using the (w_0, w_a) parameterization in Eq. 1.10, this SNe Ia data's constraint on these parameters is $w_0 = -0.93 \pm 0.15$ and $w_a = -0.1^{+0.9}_{-2.0}$ [49].

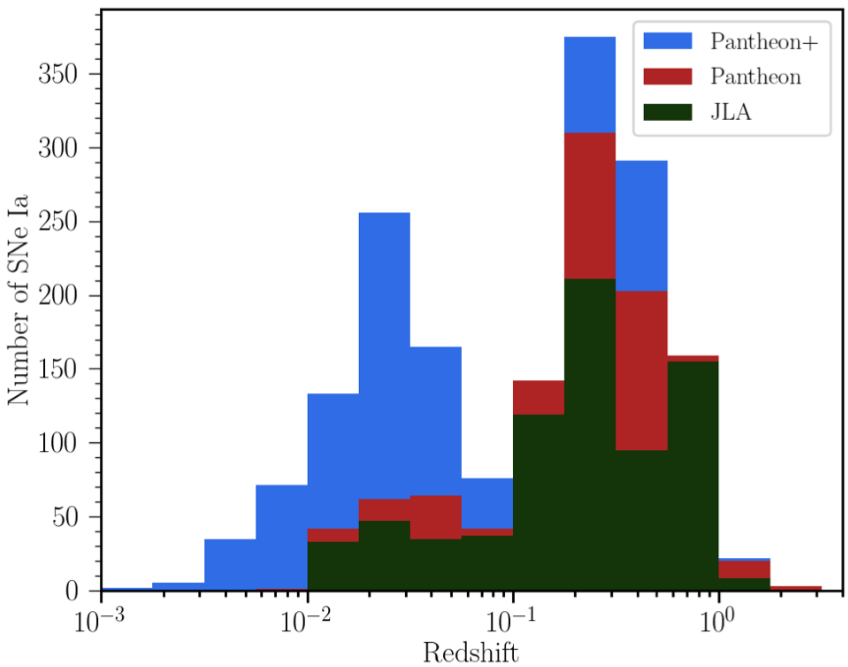

Figure 1.2: Histogram of number of type Ia supernovae (SNe Ia) samples from the Pantheon+ data set (blue) in each redshift bin. The figure also includes redshift distribution of SNe Ia data sets from the first Pantheon analysis (red) and the Joint Light-curve Analysis (black). Adopted from [191].

1.1.4.2 Baryon Acoustic Oscillations (BAO)

Baryon acoustic oscillations are oscillations of the photon-baryon fluid before recombination. Before photons, electrons and baryons decouple from each other, the photon-baryon fluid will fall to the center of gravitational potential wells of dark matter. This infalling process is counter-posed by the build-up of pressure in the fluid and the tendency to expand outward. After the fluid has expanded to a certain degree, the pressure drops and the infalling tendency will take over again. This process of continuous expansion and compression is referred to as the BAO and these oscillations are "frozen" into wiggles in the matter power spectrum $P(k)$ (which will be discussed in details in Section 1.2.2).

A consequence of the BAO effect is a higher likelihood of finding two galaxies separated by the sound horizon distance r_s, which is the distance travelled by sound waves from the Big Bang to recombination when protons combined with electrons to form hydrogen atoms at $z_* \simeq 1,100$ [106]

$$r_s \equiv \int_0^{t_*} \frac{c_s}{a(t)} dt = \frac{c}{\sqrt{3}} \int_0^{a_*} \frac{da}{a^2 H(a) \sqrt{1 + \frac{3\Omega_b}{4\Omega_\gamma} a}} \simeq 100\, h^{-1}\,\mathrm{Mpc}, \tag{1.17}$$

where $t_* \simeq= 50,000$ and $a_* \simeq 0.001$ are the age and scale factor at recombination, respectively; c_s is the speed of sound; and Ω_b/Ω_γ is the baryon-to-photon ratio.

If one has an independent knowledge of the sound horizon distance (for example, from the morphology of peaks in CMB angular power spectrum) as a "standard ruler", then BAO can be used in measuring angular diameter distances $d_A(z)$ and the Hubble parameter $H(z)$ at a certain redshift, both of which are sensitive to cosmological and dark energy parameters.

In the transverse direction, measurement of the subtended angle $\Delta\theta_s$ between galaxies at a redshift z is connected to the angular diameter distance through

$$\Delta\theta_s = \frac{r_s}{d_A(z)}, \tag{1.18}$$

where $d_A(z)$ is defined through the comoving distance as

$$d_A(z) = \frac{r(z)}{1+z}. \tag{1.19}$$

The comoving distance $r(z)$ follows Eq. 1.16 and depends on energy density of different components of the Universe and dark energy equation of state.

Likewise, in the radial direction, BAO feature's redshift extent Δz_s is connected to the Hubble parameter through

$$\Delta z_s = \frac{H(z)r_s}{c}, \tag{1.20}$$

where $H(z)$ is defined as

$$H(z) = H_0\sqrt{\Omega_M(1+z')^3 + \Omega_{\rm DE}(1+z')^{3(1+w)} + \Omega_R(1+z')^4 - \Omega_K(1+z')^2}. \tag{1.21}$$

Combining information on the transverse and radial direction, we can approach BAO with a single quantity:

$$D_v = \left(d_A^2(z)\frac{z}{H(z)}\right)^{1/3}. \tag{1.22}$$

BAO features can be extracted from photometric and spectroscopic galaxy surveys, such as Sloan Digital Sky Survey (SDSS; measurement results see e.g. [176, 41]) and the recently launched Dark Energy Spectroscopic Instrument (DESI; measurements from early data in [144]).

1.1.4.3 Cosmic Microwave Background (CMB)

The cosmic microwave background (CMB) encodes the information of the Universe at recombination when electrons and protons bound to form hydrogen atoms. Known as the Rosetta Stone of the Universe, the CMB contains rich information of cosmological parameters and expansion history, including properties of dark energy.

The CMB acts as a blackbody. It has a very uniform temperature $T = 2.725$ K today across the sky and only very tiny fluctuations on the order of $\langle(\delta T/T)^2\rangle^{1/2} \simeq 10^{-5}$. Figure 1.3 shows a map of CMB, where the red and blue color represent anisotropies in temperature.

The summary statisics we use to quantify the temperature fluctuations is the angular two-point correlation function

$$C(\theta) \equiv \langle\frac{\delta T}{T}(\hat{\vec{n}})\frac{\delta T}{T}(\hat{\vec{n'}})\rangle_{\hat{\vec{n}}\cdot\hat{\vec{n'}}=\cos\theta}, \tag{1.23}$$

describing the probabilities of finding two spots separated by an angle θ that have the same temperature fluctuation. Expanding $C(\theta)$ with the Legendre polynomial, one can obtain the CMB angular power spectrum C_ℓ:

$$C(\theta) = \sum_{\ell=2}^{\infty}\frac{2\ell+1}{4\pi}C_\ell P_\ell(\cos\theta), \tag{1.24}$$

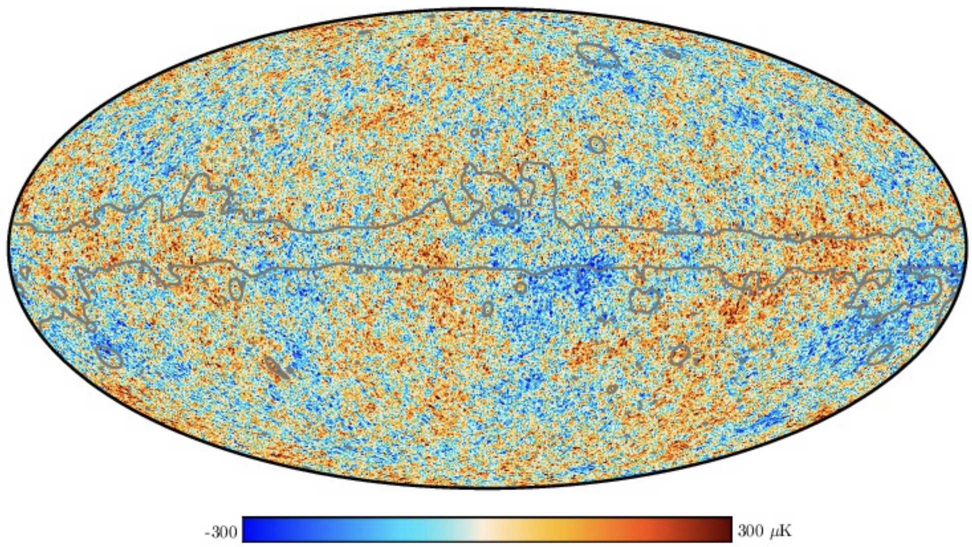

Figure 1.3: CMB temperature sky map from Planck 2018 release where contamination in the Galactic plane (outlined in grey) is removed with the SMICA technique. Red and blue represent cold and hot spots in the CMB. Adopted from [11].

where $P_\ell(\cos\theta)$ is the ℓ-th Legendre polynomial and the multipole ℓ is connected to the angular separation through $\ell \sim \pi/\theta$. Figure 1.4 gives an example of the CMB angular power spectrum.

But how can one use the CMB to constrain dark energy? Despite the fact that dark energy becomes dominant in the Universe long after the epoch of CMB, distance to the last scattering surface, which is encoded as peak locations in the angular power spectrum, is sensitive to dark energy. Again, with an independent knowledge of the sound horizon $r_s(z_*)$ which is measured at recombination, its projection into angular separations is dependent upon the comoving distance at recombination $r(z_*)$ through $\theta_* = r_s(z_*)/r(z_*)$. As in the previous two cosmological probes, the comoving distance is sensitive to dark energy parameters $\Omega_{\rm DE}$ and w and impacts on CMB from dark energy are reflected eventually in the angular features between hot and cold spots in the CMB map.

In the meantime, as the cold and hot spots represent photons falling into or climbing out of gravitational potential wells, the CMB contains important information on the clustering of matter at recombination. Features in CMB power spectrum can fix the combination $\Omega_M H_0^2$. Therefore, even though it seems that SNe Ia, BAO and CMB are all sensitive to cosmological parameters through the comoving distance, the CMB probes a different set of cosmological parameters and thus is an excellent complementary probe to dark energy.

Figure 1.5 shows constraints on dark energy and matter density parameter, using combined data from SNe Ia, BAO and CMB. Separately, each probe may not constrain both dark energy and matter density parameters well, but together, the three probes complement each other and are able

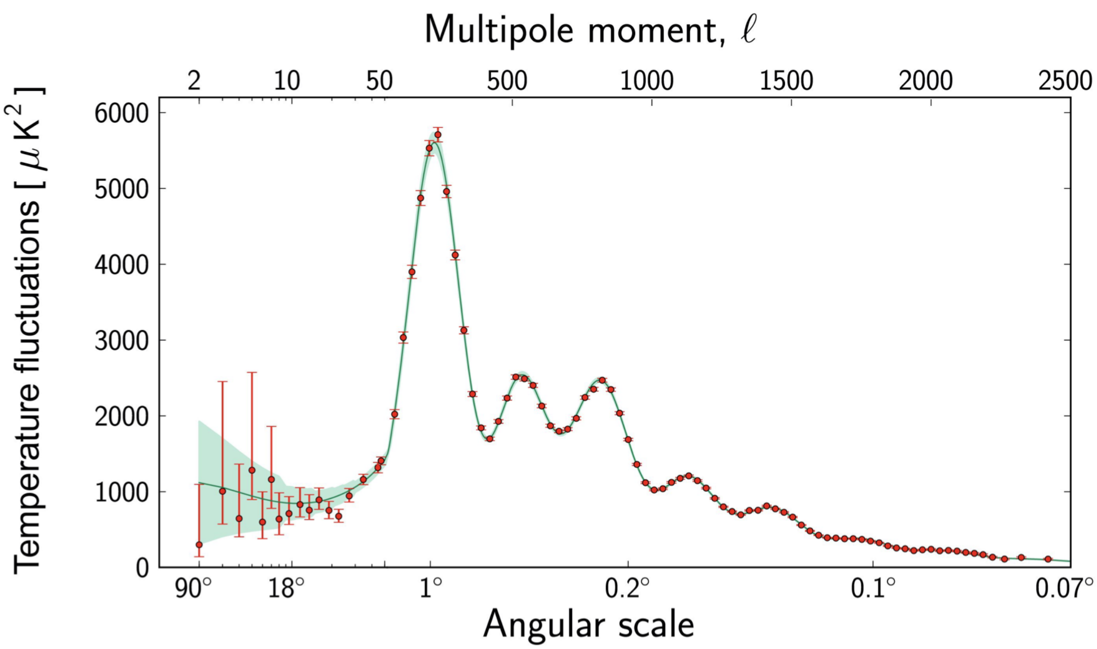

Figure 1.4: An example of CMB angular power spectrum of temperature fluctuations as a function of multipole ℓ or angular scale. The red data points are Planck 2013 measurements, while the green curve is the best-fit ΛCDM model, whose cosmic variance is shown as the shade around it. Adopted from [106, 7].

to yield a very tight constraint in the Ω_Λ-Ω_M plane, indicating strong evidence for dark energy and a preference for a flat geometry of the Universe.

Figure 1.6 further illustrates the power of CMB as a complementary probe of dark energy. With only SNe Ia (green contours), there is a degeneracy between the dark energy equation of state w and Ω_M and this degeneracy is only broken after the addition of CMB and BAO data (red contours). The contrast between constraints from earlier surveys (red contours) and more recent ones (blue contours) demonstrates the largely-improved constraining power over the past two decades.

1.2 Growth of Structure

Primordial fluctuations generated about 10^{-34} seconds after the Big Bang during inflation are seeds for the later formation of large scale structures under the influence of gravity. These initial perturbations in the density of matter are encoded in the hot and cold spots in the temperature map of the CMB as photons fall into or climb out of these potential wells. We can quantify these primordial overdensities by defining a $\delta(\vec{x}, t) \equiv (\rho(\vec{x}, t) - \bar{\rho})/\bar{\rho}$, where $\bar{\rho}$ is the average matter density. The value of initial matter density perturbations is $\delta = 10^{-5}$ [105].

The growth of primordial seeds of overdensities into the present day large scale structure is

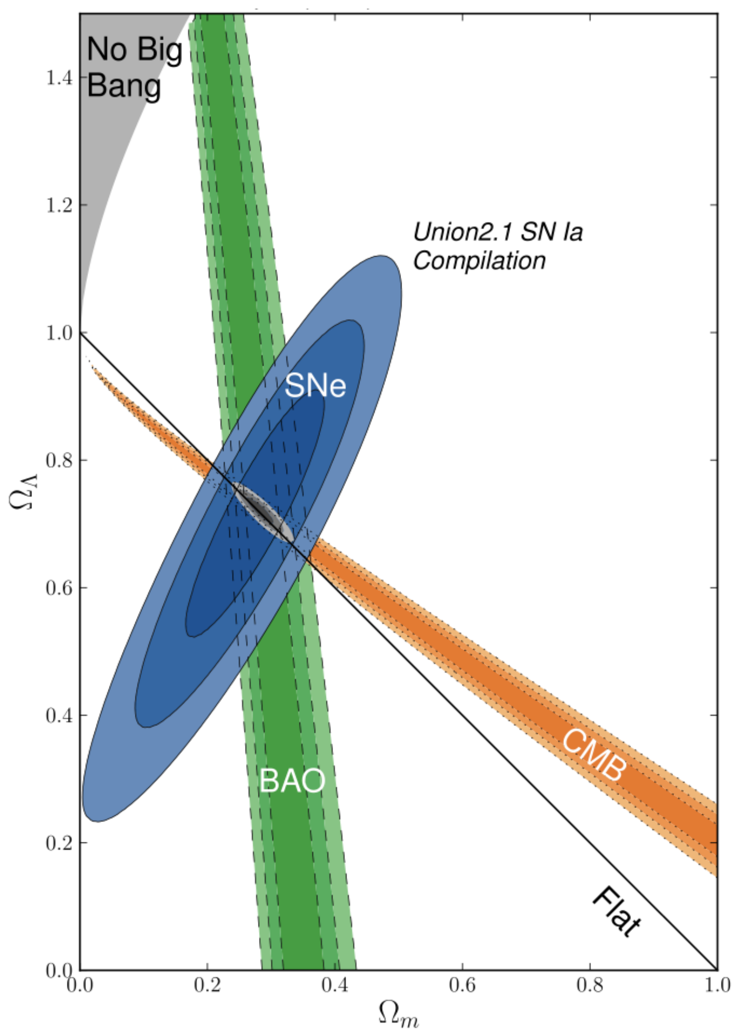

Figure 1.5: Constraints on the dark energy and matter density parameter by type Ia supernovae (blue), baryon acoustic oscillations (green) and cosmic microwave background (orange), separately and combined (grey), while the black line indicates the direction of a flat geometry of the Universe. Adopted from [77].

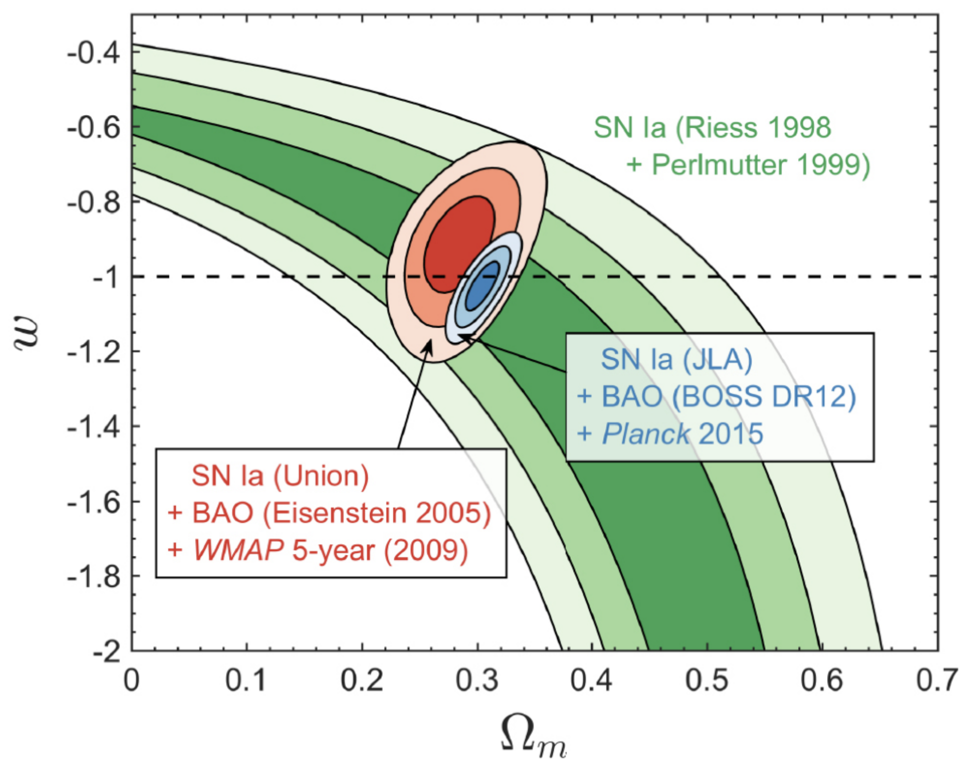

Figure 1.6: Constraints on the dark energy equation of state w and the matter density parameter Ω_M from SNe Ia alone (green) and after the addition of BAO and CMB data (red and blue). More recent surveys of the three probes (blue) greatly tightened the constraints than the earlier surveys (red). Adopted from [109].

dominated by two competing processes, the influence of gravity and the expansion of the Universe. As a result, the theory of gravity and the constitution of energy content of the Universe become key components that will determine the growth history. The following section will give an overview of the theoretical framework of structure formation, with an emphasis on the impact of dark energy. Growth of structure can also function as a sensitive test for any modifications to general relativity, a topic we will discuss further in a later section devoted to modified gravity theories.

1.2.1 Linear Growth of Structure

In this section, we will consider structure formation under the following conditions:

1. General relativity as our theory of gravity;
2. $|\delta| \ll 1$ such that we can employ perturbation theory in the linear regime;
3. Isentropic initial conditions where there is no initial fluctuation in entropy, as predicted by inflation and favored by data;
4. Focus on fluctuations that are sub-horizon but far beyond Jeans scale.

With these premises, one can start with the three fundamental equations in comoving coordinates describing the evolution of a fluid:

$$\begin{aligned}
\frac{\partial \delta}{\partial t} + \frac{1}{a}\nabla\left[(1+\delta)\vec{v}\right] &= 0 \quad \text{(Continuity)}\\
\frac{\partial \vec{v}}{\partial t} + \frac{\dot{a}}{a}\vec{v} &= -\frac{\nabla\phi}{a} - \frac{c_s^2}{a}\nabla\delta - \frac{2T}{3a}\nabla S \quad \text{(Euler)}\\
\nabla^2\phi &= 4\pi G\bar{\rho}a^2\delta \quad \text{(Poisson)},
\end{aligned} \tag{1.25}$$

where ϕ is the gravitational potential, c_s is the speed of sound, T is the temperature and S is the entropy.

Then we can combine these three equations and take the proper Fourier transforms of the overdensity $\delta_{\vec{k}} = \frac{1}{V_u}\int \delta(\vec{r},t)e^{-i\vec{k}\cdot\vec{r}}d^3\vec{r}$, where V_u is the volume over which perturbations can be assumed as periodic. In this way, we will arrive at the second-order differential equation that describes the growth of overdensities over time [105]

$$\frac{\partial^2\delta_{\vec{k}}}{\partial t^2} + 2\frac{\dot{a}}{a}\frac{\partial\delta_{\vec{k}}}{\partial t} = \left(4\pi G\bar{\rho} - \frac{k^2c_s^2}{a^2}\right)\delta_k - \frac{2}{3}\frac{T}{a^2}k^2S_{\vec{k}}, \tag{1.26}$$

where $S_{\vec{k}}$, the Fourier mode of entropy fluctuations, vanishes under the isentropic initial condition. We can also drop the terms that are of second order in k since the scales we consider are much smaller than the Jeans scale. Therefore, Eq. 1.26 can be simplified into

$$\ddot{\delta} + 2H\dot{\delta} - 4\pi G\bar{\rho}\delta = 0. \tag{1.27}$$

During the radiation-dominated era, $\bar{\rho}$ is negligible. Meanwhile, the scale factor $a(t)$ is proportional to $t^{1/2}$, then the Hubble parameter can be written as $H(t) \equiv \dot{a}/a = 1/(2t)$. As a result, solution to the growth equation (Eq. 1.27) is $\delta(t) = A_1 + A_2 \ln t$. Structure grows slowly following a logarithmic scale when radiation dominates in the early Universe.

Likewise, during the matter-dominated era, the Hubble parameter is dominated by matter and hence $H^2(t) = 8\pi G\bar{\rho}/3$. In this epoch, the scale factor goes as $a(t) \sim t^{2/3}$, so the solution is $\delta(t) = B_1 t^{2/3} + B_2 t^{-1}$. If we only look at the growth term (i.e. the first term) in the solution, we will see that when matter dominates, $\delta(t) \sim a(t)$. Structure grows substantially in this period, proportionally to the scale factor.

When dark energy takes over in late times, growth of structure is again suppressed by the accelerated expansion of the Universe. In this epoch, the Hubble parameter is constant where $H = H_\Lambda$ and the scale factor grows exponentially with time $a(t) = e^{Ht}$. Therefore, the solution is $\delta(t) = C_1 + C_2 e^{-2H_\Lambda t}$. The second term will quickly decay away exponentially, so when dark energy completely dominates, the growth of structure will stagnate.

It is obvious by this point that the growth of structure is certainly sensitive to the energy density and equation of state of dark energy. This late-time suppression of growth in the presence of dark energy will be illustrated even more clearly when we introduce several dimensionless functions describing different aspects of growth.

A linear growth function can be defined as

$$D(a) \equiv \frac{\delta(a)}{\delta(a=1)}, \tag{1.28}$$

And a growth suppression factor $g(a)$ is defined through $D(a)$ as $D(a) \equiv ag(a)/g(1)$. Figure 1.7 demonstrates $D(z)$ and $g(z)$ respectively as a function of redshift assuming a ΛCDM cosmology where dark energy takes up ~70% of the Universe versus a matter-only Einstein-de Sitter (EdS) Universe. At late times when z approaches 0, growth is suppressed in ΛCDM due to the presence of dark energy compared to a matter-only scenario.

Another dimensionless function describing the growth rate of large scale structure can also be defined through taking a derivative of the growth function $D(a)$. The linear growth rate function is

$$f(a) \equiv \frac{d \ln D}{d \ln a}. \tag{1.29}$$

Assuming general relativity, $f(a)$ is scale-independent and is only a function of the scale factor or

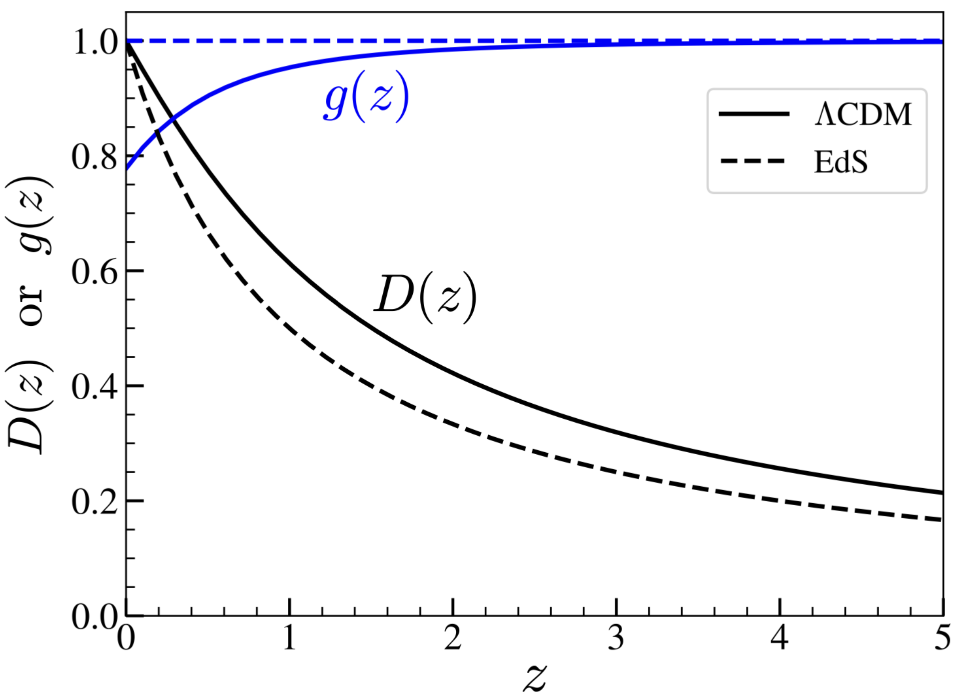

Figure 1.7: Dimensionless growth function $D(z)$ and growth suppression factor $g(z)$ as a function of redshift in a ΛCDM Universe (solid) and in Einstein-de Sitter Universe (dashed). Adopted from [105].

redshift. It has a well-known paramterization that fits a wide range of cosmological models [154]

$$f(z) = \Omega_M(z)^\gamma, \tag{1.30}$$

where $\Omega_M(z)$ is the energy density parameter for matter at a given redshift and the exponent γ is called the growth index. The best-fit value of the growth index, $\gamma = 0.55$, can fit ΛCDM models to sub-percent level [155].

1.2.2 Matter Power Spectrum

A powerful statistical tool and key observable in mapping out the distribution of overdensities across the Universe is the two-point correlation function and the matter power spectrum derived from it.

The two point correlation function can be understood as the mean probability of repeating the following process: throwing a stick of length r into a map populated by points and finding out that each end of the stick happens to land on a point. Mathematically, it is defined as

$$\xi(r) = \frac{\langle [\rho(\vec{x}+\vec{r}) - \langle\rho\rangle][\rho(\vec{x}) - \langle\rho\rangle]\rangle_{\vec{x}}}{\langle\rho\rangle^2} = \langle\delta(\vec{x}+\vec{r})\delta(\vec{x})\rangle_{\vec{x}}, \tag{1.31}$$

between a point at $\vec{x}$ and another point separated by $\vec{r}$.

If we consider the overdensities in Fourier space components $\delta_{\vec{k}}$, the two-point correlation function in Fourier space is

$$\langle\delta_{\vec{k}}\delta^*_{\vec{k}'}\rangle = (2\pi)^3\delta^{(3)}(\vec{k} - \vec{k}')P(k), \tag{1.32}$$

where $\delta^{(3)(\vec{k}-\vec{k}')}$ is the Kronecker delta function in 3 dimensions, and $P(k)$ is the matter power spectrum, measuring the amount of structure at each scale k. It is related to the one in real space, $\xi(r)$, through $P(k) = \int \xi(r)e^{-i\vec{k}\cdot\vec{r}}d^3\vec{r}$.

In the linear regime, we can arrange the matter power spectrum to define a dimensionless and more machine-friendly one

$$\begin{aligned}\Delta^2(k,z) &= \frac{k^3P(k,z)}{2\pi^2} \\ &= A_s\frac{4}{25}\frac{1}{\Omega_M^2}\left(\frac{k}{k_{\text{piv}}}\right)^{n_s-1}\left(\frac{k}{H_0}\right)^4\left(\frac{g(z)}{1+z}\right)^2 T^2(k),\end{aligned} \tag{1.33}$$

where A_s is the normalized amplitude of the matter power spectrum and n_s is the spectral index. The "pivot" k_{piv} is close to the scale where the primordial power is constrained best and where n_s

is computed. $T(k)$ is called the linear transfer function. It expresses the shape change of the matter power spectrum around matter-radiation equality.

Another point to note in the expression of power spectrum is that the term $g(z)/(1+z) = ag(a) \sim D(a)$. Therefore, the matter power spectrum is sensitive to growth through the following relation:

$$\Delta^2(k,z) \sim P(k,z) \sim [ag(a)]^2 \sim D^2(z). \tag{1.34}$$

Based on the matter power spectrum which is a function of scale at a certain redshift, one can define a root mean squared amplitude of matter fluctuations within a certain spherical region by integrating $\Delta^2(k,z)$ over this region and over all scales:

$$\sigma^2(z,R) = \int_0^\infty \Delta^2(k,z) \left(\frac{3j_1(kR)}{kR}\right)^2 d\ln k, \tag{1.35}$$

where R is the comoving radius of the spherical region and $j_1(kR)$ is the spherical Bessel function of the first kind. Conventionally, we set the radius to be $R = 8\ \mathrm{h}^{-1}$ Mpc and the quantity evaluted at $z = 0$ is named σ_8, a constraint often quoted in galaxy surveys.

1.2.3 Cosmological Probes of Growth

In this section, we will give an overview of the major cosmological probes used to measure the growth of structure. Through presenting the power spectrum of each probe, we will illustrate in what ways are each probe sensitive to growth and cosmological parameters.

1.2.3.1 Galaxy Clustering

Galaxy clustering is the oldest and most mature probe of cosmic growth that constrains the matter power spectrum. Figure 1.8 shows a map of the large scale structure from the Sloan Digital Sky Survey (SDSS) where each point is a galaxy in the sky colorred by the age of stars in it.

The summary statistics we extract from these photometric large scale structure surveys is the correlation between galaxy positions $P_(\mathrm{gg})(\mathrm{k, z})$, and this is connected to the matter power spectrum $P(k,z)$ through

$$P_{\mathrm{gg}} = b^2(k,z)P(k,z), \tag{1.36}$$

where $b^2(k,z)$ is called galaxy bias. A bias is introduced because amplitude of clustering of the density field is different from that of the peaks (of the density field). Amplitude of clustering of

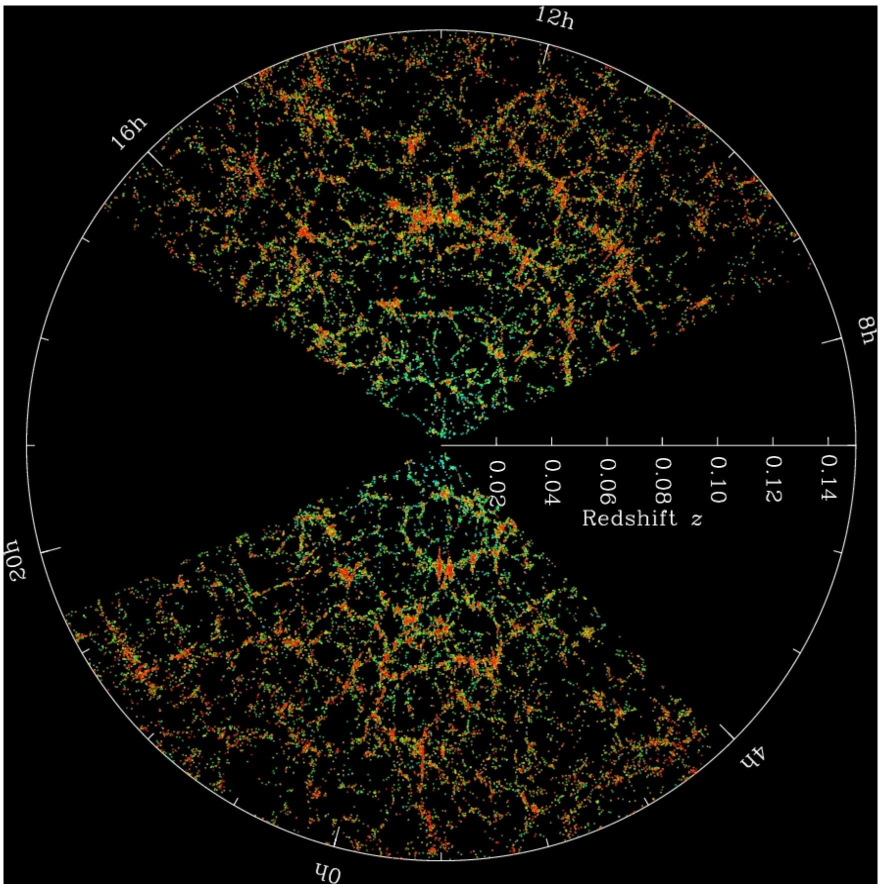

Figure 1.8: The large scale structure map from he Sloan Digital Sky Survey (SDSS). Each point on the figure represents a galaxy, and redder ones are galaxies with older stars while green ones have younger stars. Figure credit: M. Blanton and the Sloan Digital Sky Survey, adopted from [44].

peaks is not representative of the general distribution of dark matter across the entire field expressed in $P(k, z)$, so we need to quantify this discrepancy with $b(k, z)$.

The presence of galaxy bias adds complications to the measurement of matter power spectrum because it is difficult to model theoretically. Galaxy bias depends heavily on galaxy types and the formation history of galaxies and requires input from other probes such as weak lensing, galaxy-galaxy lensing or three-point statistics.

Additionally, measurements of galaxy clustering are mostly made on scales that are close to or in the non-linear regimes where the linear theory of growth in Eq. 1.27 does not hold. Expensive N-body simulations are required to model corrections to matter power spectrum in the non-linear regime.

Lastly, if one wants to measure the temporal evolution of cosmic structure, redshift of galaxies observed in the survey is necessary, either through complementary spectroscopic information or through photometric-redshift estimations.

1.2.3.2 Weak Gravitational Lensing

Weak gravitational lensing is a phenomenon where the shape of a source galaxy is distorted by the large scale structure between the Earth and where it is. As light emitted from the galaxy is bent by the gravitational potential wells created by the structure, this distortion of shape is thus sensitive to the distribution of matter in between. Weak lensing's main advantage as a probe for growth is the absence of any galaxy biases [105]. Figure 1.9 is a carton illustration of this effect.

We quantify the effects of weak lensing through the convergence κ, defined as

$$\kappa = \frac{d_{\mathrm{L}} d_{\mathrm{LS}}}{d_{\mathrm{S}}} \int_0^{S_{\mathrm{src}}} \nabla^2 \Phi ds. \tag{1.37}$$

The convergence is a function of position in the sky and is proportional to the amount of projected matter density between the observer and the source (i.e. a distant galaxy). This can be seen more clearly from its definition where the gravitational potential Φ is integrated along the line of sight. The coefficients in Eq. 1.37 are respectively the distance to the lens (d_{L}), to the source (d_{S}) and between the lens and the source (d_{LS}). The convergence power spectrum, written in harmonic space, is

$$\langle \kappa_{lm} \kappa_{l'm'} \rangle = \delta_{ll'} \delta_{mm'} P^{\kappa\kappa}(\ell). \tag{1.38}$$

Alternatively, if we do not integrate along the line of sight between the observer and the source galaxy but look at correlations of convergence between different redshift bins, we can write out

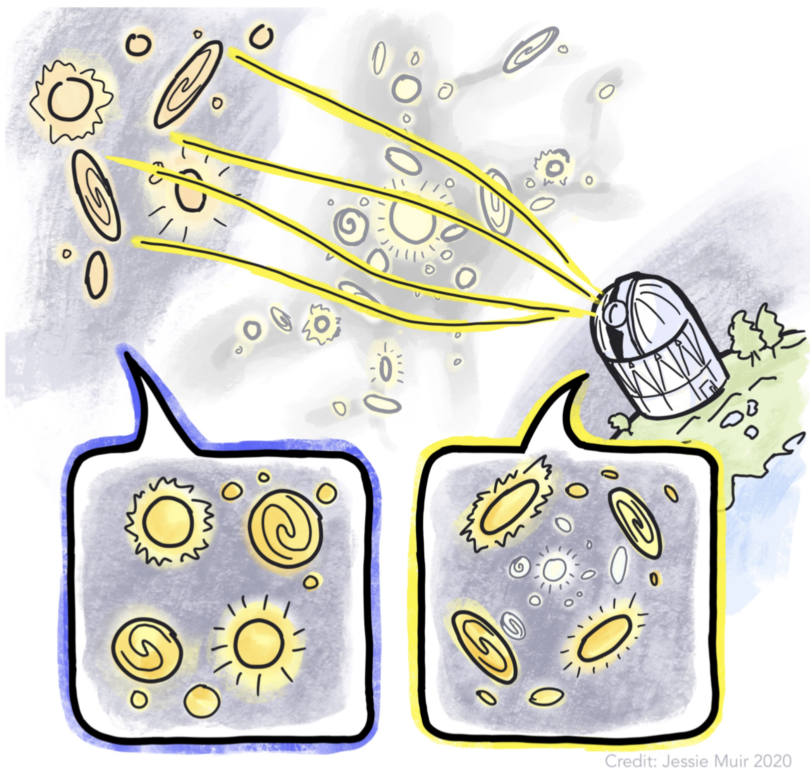

Figure 1.9: A cartoon illustration of weak gravitational lensing, where the light from source galaxies is bent by the large scale structure in between, leading to a distortion in the observed shape of the source galaxies. Created by Jessie Muir and adopted from [106].

what is called a tomographic power spectrum

$$P_{ij}^{\kappa\kappa}(\ell) = \int_0^\infty dz \frac{W_i(z)W_j(z)}{r^2(z)H(z)} P(\frac{\ell}{r(z)}, z). \tag{1.39}$$

The $W_i(z)$ are weights and are defined as

$$W_i(\chi) \equiv \frac{3}{2}\Omega_M H_0^2 q_i(\chi)(1+z), \tag{1.40}$$

where

$$q_i(\chi) \equiv r(\chi) \int_\chi^\infty d\chi_s n_i(\chi_s) \frac{r(\chi_s - \chi)}{r(\chi_s)} \tag{1.41}$$

and for χ_s within the ith redshift bin, n_i is the normalized comoving density of galaxies. In the tomographic power spectrum, the weights contain no information on growth and the connection to theory of growth is encoded in the matter power spectrum term $P(\ell/r(z), z)$.

The other key quantity of weak lensing is the shear γ, the extent of shape distortion. As long as the distortions are week, $P^{\gamma\gamma}(\ell) \simeq P^{\kappa\kappa}(\ell)$, and the same holds true for the shear and convergence tomographic power spectrum as well. Therefore, the shear tomographic spectrum is related to growth through

$$P_{ij}^{\gamma\gamma} \sim P(k, z) \sim D^2(z). \tag{1.42}$$

The combination of weak lensing with galaxy clustering has been shown to be extremely effective in constraining growth in photometric galaxy surveys as it can break degeneracies between nuisance and cosmological parameters [68]. This methodology is referred to as the 3×2-point analysis. For every redshift bin and for every scale k, the analysis involves a 2-by-2 matrix

$$\begin{pmatrix} \mathrm{gg} & \mathrm{g}\gamma \\ \mathrm{g}\gamma & \gamma\gamma \end{pmatrix}, \tag{1.43}$$

where the gγ entry denotes the correlation between shear and galaxy position.

The quantity constrained by this kind of analysis is a combination of matter density fluctuation and matter energy density:

$$S_8 = \sigma_8 \sqrt{\frac{\Omega_M}{0.3}}. \tag{1.44}$$

1.2.3.3 Peculiar Velocities

In linear theory, the continuity equation in [74] gives the relation between cosmic velocities and matter overdensities:

$$\vec{v} = \frac{i\vec{k}}{k^2}\frac{D'}{D}\delta = \frac{i\vec{k}}{k^2}afH\delta, \tag{1.45}$$

where f is the linear growth rate defined in Eq. 1.29. Then, the velocity power spectrum in linear theory is

$$P_{\rm vv}(k,a) = \left[\frac{af(a)H(a)}{k}\right]^2 P(k,a), \tag{1.46}$$

sensitive to growth history and cosmological parameters.

If we measure the velocity of individual galaxies at distance $\vec{x}$, it is

$$\dot{\vec{x}} = \frac{d}{dt}(a\vec{r}) = \dot{a}\vec{r} + a\dot{\vec{r}} = H\vec{x} + \vec{v}_{\rm pec}, \tag{1.47}$$

and at low redshift when $z \ll 1$, it becomes

$$cz_{\rm obs} = cz + v_{\rm pec}. \tag{1.48}$$

Therefore, if we want to determine the peculiar velocities, we would need accurate measurements of the other two terms in Eq. 1.48: the observed redshift and distance.

Looking at the velocity power spectrum, one will see that

$$P_{\rm vv}(k,z) \sim f^2(z)P(k,z) \sim f^2(z)\sigma_8^2(z) \sim [f(z)\sigma_8(z)]^2 \,. \tag{1.49}$$

This explains why the growth-related quantity usually constrained by peculiar velocities surveys is the combination $f\sigma_8$.

1.2.3.4 Redshift-Space Distortions

When the spatial distribution of galaxies are plotted in the redshift space, the distribution of their positions will be distorted because of the Doppler shifts caused by their peculiar velocities outside of the cosmological redshift induced by the accelerated expansion of the Universe. In other words, clustering measurements are distorted due to gravitational infalling into nearby overdensities or the galaxies' own peculiar velocities.

Figure 1.10 illustrates two common effects of redshift-space distortions (RSD). The first one,

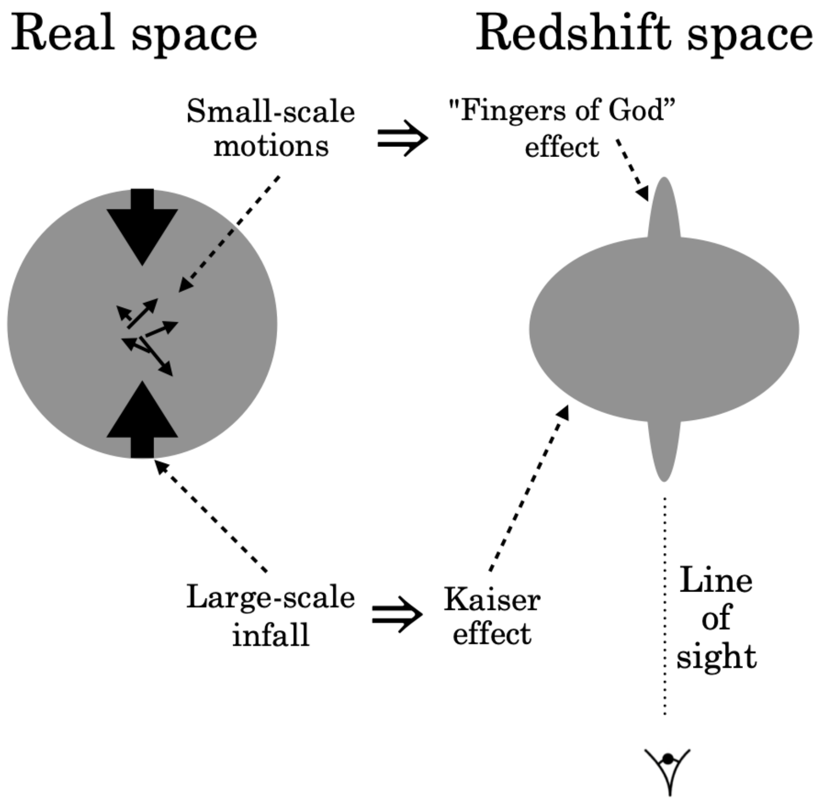

Figure 1.10: An illustration of two redshift-space distortions effects. The Kaiser effect (left) shows a flattening along the line of sight on large scales due to infalling into nearly large overdensities. The “fingers of God” (right) is an elongation on small scales in the redshift space along the line of sight. Adopted from [105].

known as the Kaiser effect, corresponds to a kind of flattening or “squishing” in real space along the line of sight on large scales as galaxies fall into nearby large overdensities. The other one, named “fingers of God” shows elongation in the radial direction on small scales in the redshift space.

The RSD power spectrum in redshift space (as denoted by the superscript s) to the lowest order is

$$P(\vec{k}, z)^{(s)} = \left[b + f\mu^2\right]^2 F(k^2\sigma_v^2\mu^2)P(k, z), \tag{1.50}$$

where μ is the cosine of the angle between $\vec{k}$ and line of sight, b is the galaxy bias, f is the linear growth rate, σ_v is the velocity dispersion and the function $F(k^2\sigma_v^2\mu^2) = 1/(1+k^2\sigma_v^2\mu^2)$, modeling suppression of the power spectrum at high k [105]. RSD measures the parameter combination $f\sigma_8$ to an excellent degree and functions as a good test for different theories of dark energy and modified gravity [195].

1.2.3.5 Cosmic Microwave Background

Despite the fact that CMB only provides information on matter overdensities during recombination, a period way before the emergence of dark energy as the dominant component, it still can provide tight constraints on the amplitude of the initial fluctuations in matter. Combined with constraints on σ_8, this information from the CMB can greatly help with understanding the temporal growth of structure.

Furthermore, as CMB photons travel through the large scale structure, they will be deflected. This effect of CMB lensing manifests itself as minor displacements of the cold and hot spots in the temperature map and is useful in probing the large scale structure.

In addition to the most famous tension in cosmology — the Hubble tension, there is another tension in measurements of the combined parameter S_8, where measurements from CMB is higher than those from lensing surveys. For instance, the Planck 2018 analysis including polarization and lensing constrains S_8 to be 0.832 ± 0.013 [13] while Dark Energy Survye Year 3 (DES Y3) year 3 results give $S_8 = 0.775 \pm 0.017$ [105, 5].

1.3 Modified-Gravity Theories

As the accelerated expansion of the Universe does not naturally arise from the theory of general relativity, there has been a vast range of attempts to propose a theory that can incorporate this effect. In essence, these modifications to general relativity involves adding extra degrees of freedom through the introduction of scalar fields, incorporating higher dimensions, or breaking diffeomorphism invariance etc.

1.3.1 Modified Gravity versus Dark Energy

Broadly speaking, there are two possibilities of what gives rise to the late-time cosmic acceleration. One possibility is that the acceleration is caused by a not-yet-identified component in the Universe. One example is the vacuum energy or the cosmological constant with $w = -1$ as discussed in Section 1.1.1. Another explanation for the late-time cosmic acceleration that falls under this category is the quintessence model where the dark energy candidate is a slowly-evolving scalar field. Under this theory, a scalar field ϕ is minimally coupled to gravity and slowly varies under a potential $V(\phi)$, a mechanism somewhat similar to the slow-roll model of inflation [203].

For a sub-category of quintessence models where the field is stalled by the Hubble friction in the early period and only starts to evolve in late times, one can find analytical solutions to the equation of state w, and w in turn can be constrained by cosmological probes such as type Ia supernova, CMB or BAO. Analytical solutions for the combination $f\sigma_8(z)$ in terms of the energy density parameter of the scalar field Ω_ϕ can also be found, and quitessence models can therefore be constrained by RSD or peculiar velocities surveys [203].

Other potential candidates under this category include k-essence where the scalar field only enters kinetic terms but not potential ones [56] and other exotic fluids such as the Chaplygin gas whose equation of state assumes $p \sim -1/\rho$ [119].

The second possible explanation involves modifications to the theory of gravity at large scales, where the late-time cosmic acceleration arise from the theory itself without introducing a new energy content. We will introduce in the follow sections several classes of such theories.

1.3.1.1 $f(R)$ Gravity

One general class of modified gravity theories involves a direct generalization of the GR Lagrangian. Named $f(R)$ gravity, this theory generalizes the Ricci scalar R into a general function of it, and the action of this theory takes the form of [202]

$$S = \frac{1}{16\pi G}\int d^4x\sqrt{-g}f(R) + S_m[g_{\mu\nu}], \tag{1.51}$$

where the g is a determinant of the metric $g_{\mu\nu}$ and the second term $S_m[g_{\mu\nu}]$ is the action for matter interactions. When $f(R) = R$, this action reduces back to the GR.

Assuming a flat FRW metric and taking a variational approach to the $f(R)$ action, one can obtain the equations of motion as [196]

$$\begin{aligned} H^2 &= \frac{\kappa}{3f'}\left[\rho + \frac{Rf' - f}{2} - 3H\dot{R}f''\right] \\ 2\dot{H} + 3H^2 &= -\frac{\kappa}{f'}\left[p + (\dot{R})^2 f''' + 2H\dot{R}f'' + \ddot{R}f'' + \frac{1}{2}(f - Rf')\right], \end{aligned} \tag{1.52}$$

where $\kappa \equiv 8\pi G$. Defining an effective density $\rho_{\rm eff}$ and an effective pressure $p_{\rm eff}$ as [196]

$$\begin{aligned} \rho_{\rm eff} &= \frac{Rf' - f}{2f'} - \frac{3H\dot{R}f''}{f'} \\ p_{\rm eff} &= \frac{\dot{R}^2 f''' + 2H\dot{R}f'' + \ddot{R}f'' + \frac{1}{2}(f - Rf')}{f'}, \end{aligned} \tag{1.53}$$

the field equations in Eq. 1.52 can be rewritten into the form of Friedmann equations

$$\begin{aligned} H^2 &= \frac{8\pi G}{3}\rho_{\rm eff} \\ \frac{\ddot{a}}{a} &= -\frac{4\pi G}{3}(\rho_{\rm eff} + 3p_{\rm eff}). \end{aligned} \tag{1.54}$$

If we enforce the relation $\frac{f'''}{f''} = \frac{\dot{R}H - \ddot{R}}{\dot{R}^2}$, the equation of state of this effective component is $w_{\rm eff} = -1$. Under these conditions, $f(R)$ gravity can mimic the behavior of a cosmological constant that will give rise to the observed cosmic acceleration without introducing a new component as the physical source of dark energy.

1.3.1.2 Scalar-Tensor Gravity

As the name suggests, in scalar-tensor gravity, a scalar field ϕ is coupled to the Ricci scalar R in the action. The most general form of scalar-tensor theory action is

$$S = \int d^4\sqrt{-g}\left[\frac{1}{2}f(\phi, R) - \frac{1}{2}\zeta(\phi)\,(\nabla\phi)^2\right] + S_m[g_{\mu\nu}]. \tag{1.55}$$

When $f(\phi, R) = f(R)$ and $\zeta(\phi) = 0$, scalar-tensor gravity will reduce to $f(R)$ gravity, which is a special case of scalar-tensor model.

Of particular interest to works in this dissertation is the Horndeski theory. It is the most general scalar-tensor theory and has second-order equations of motion in four dimensions that will avoid the appearance of a ghost [117]. The action of Horndeski theory is [120]

$$\begin{aligned} S = \int & d^4\sqrt{-g}G_2(\phi, X) + G_3(\phi, X)\Box\phi + G_4(\phi, X)R \\ &+ \frac{\partial G_4(\phi, X)}{\partial X}\left[(\Box\phi)^2 - (\nabla_\mu\nabla_\nu\phi)(\nabla^\mu\nabla^\nu\phi)\right] + G_5(\phi, X)G_{\mu\nu}\nabla^\mu\nabla^\nu\phi \\ &- \frac{1}{6}\frac{\partial G_5(\phi, X)}{\partial X}\left[(\Box\phi)^3 - 3(\Box\phi)(\nabla_\mu\nabla_\nu\phi)(\nabla^\mu\nabla^\nu\phi) + 2(\nabla^\mu\nabla_\alpha\phi)(\nabla^\alpha\nabla_\beta\phi)(\nabla^\beta\nabla_\mu\phi)\right], \end{aligned} \tag{1.56}$$

where $X \equiv -\frac{1}{2}\nabla^\mu\phi\nabla_\mu\phi$, $\Box \equiv \nabla^\mu\nabla_\mu$ and $G_{\mu\nu}$ is the Einstein tensor.

With proper choice of $G_i(\phi, X)$ where $i = 2, 3, 4, 5$, the Horndeski action can be turned into a wide range of classes of modified gravity theories. We summarize some of these relations in Table 1.1.

Model	$G_2(\phi, X)$	$G_3(\phi, X)$	$G_4(\phi, X)$	$G_5(\phi, X)$
Quintessence	$X - V(\phi)$			
K-essence	$G_2(\phi, X)$	0	$M_{\rm pl}^2/2$	0
Brans-Dicke	$M_{\rm pl}\omega_{\rm BD}X/\phi - V(\phi)$	0	$M_{\rm pl}\phi/2$	0
$f(R)$ **Gravity**	$-M_{\rm pl}^2(RF - f)/2$	0	$M_{\rm pl}^2/2$	0
Covariant Galileons	$\beta_1 X - m^3\phi$	$\beta_3 X$	$M_{\rm pl}^2/2 + \beta_4 X^2$	$\beta_5 X^2$

Table 1.1: Representation of various modified gravity theories by selecting proper functional forms of $G_i(\phi, X)$ in the action of Horndeski theory [120]. In the entry for $f(R)$ gravity, $F \equiv \partial f/\partial R$.

Without going into the techinical details of background variations and tensor perturbations of the Horndeski action, we here present the derived equation of state of an effective dark energy component arising from Horndeski theory in the form of [120]

$$w_{\rm DE} = -1 + \frac{2(2G_4 - M_{\rm pl}^2)\dot{H} + (\dot{\phi}^2 G_{3,X} + 2G_{4,\phi})\ddot{\phi} + \left[\dot{\phi}(G_{2,X} + 2G_{3,\phi} + 2G_{4,\phi\phi}) - H(2G_{4,\phi} + 3\dot{\phi}^2 G_{3,X})\right]\dot{\phi}}{3H^2(M_{\rm pl}^2 - 2G_4) - G_2 + \dot{\phi}^2 G_{2,X} - \dot{\phi}^2(3H\dot{\phi}G_{3,X} - G_{3,\phi}) - 6H\dot{\phi}G_{4,\phi}}, \tag{1.57}$$

where abbreviations taking the form of $G_{i,a} \equiv \partial G_i/\partial a$. It is clearly illustrated that if the true theory of the Universe is described by a Horndeski model, this modification to general relativity will manifest itself in the measured equation of state of dark energy.

1.3.2 Effective Field Theory of Dark Energy (EFTDE)

The theory space of potential modified gravity theories is enormous. The few classes of theories introduced in the previous sections are a mere fraction. The effective field theory (EFT) approach unifies a vast number of modified gravity theories under the same theoretical framework so that the properties of and observational constraints on these theories can be studied en masse.

Following the successful application of EFT formalism in particle physics and condensed matter, in cosmology, EFT approach to dark energy models aims to describe each theory under the framework of perturbations to a cosmological background.

The general form of the EFT action written in unitary gauge is [45]

$$\begin{aligned} S = \int d^4x\sqrt{-g}\bigg[&\frac{1}{2}m_0^2\Omega(t)R - \Lambda(t) - c(t)g^{00} + \frac{M_2^4(t)}{2}(\delta g^{00})^2 \\ &- \frac{\bar{M}_1^3(t)}{2}\delta K\delta g^{00} - \frac{\bar{M}_2^2(t)}{2}\delta K^2 - \frac{\bar{M}_3^2(t)}{2}\delta K_\nu{}^\mu \delta K_\mu{}^\nu \\ &+ \frac{\hat{M}^2(t)}{2}\delta R^{(3)}\delta g^{00} + m_2(t)\partial_i g^{00}\partial^i g^{00}\bigg] + S_m[g_{\mu\nu}, \psi_m], \end{aligned} \tag{1.58}$$

where g^{00} is the time-time component of the metric $g^{\mu\nu}$, $K_{\mu\nu}$ is the extrinsic curvature tensor, ψ_m is the matter field, and any quantity with a δ symbol in front of it refers to perturbations in it. This action is written in the Jordan frame rather than the Einstein frame such that matter only couples to $g_{\mu\nu}$. The gauge in which this action is written preserves a time-dependent spatial diffeomorphism invariance and the metric is invariant under this as well [45].

The time-dependent terms in Eq. 1.58 are called EFT functions. Specifying the functional form and coefficients in these EFT functions allows one to express different modified gravity theories.

In Chapter 2 and Chapter 4, we will explain in more details about how to define a modified gravity model, especially a Horndeski model under EFT formalism.

1.4 Outline of Thesis

Research presented in this dissertation studies various approaches to probe the vast theory space of modified gravity theories and test the concordance cosmological model using data from present and future surveys of dark energy and the growth of cosmic structure.

The work in Chapter 2 studies the question: What happens if the true theory dominating our Universe is a modified-gravity theory, but when we analyze observational data, we still assume a phenomenological dark energy model without modifications to general relativity (which is a common practice in today's cosmological data analysis)? Even if an incorrect theory of gravity is assumed during data analysis, we likely will not see a red flag because experimental data could still be fit sufficiently well. Therefore, in this work, we present for the first time to our knowledge a quantitative approach that will study if there are generic features that indicates the presence of modified gravity in standard cosmological analysis.

Chapter 3 presents a test of the concordance flat ΛCDM cosmology from the perspective of the growth of structure. In this work, we focus on constraining the growth rate of matter density perturbations through the parameter, "growth index". Employing current data from CMB, weak lensing, galaxy clustering and cosmic velocities, we find that the best-fit value of growth index is in a 3.7σ tension with the concordance cosmology, showing evidence of growth being suppressed in late times.

In Chapter 4, we present a new parameterization to the growth rate of matter density perturbations in Horndeski theories of modified gravity. Generalizing the popular parameterization $f(z) = \Omega_M(z)^\gamma$ into a two-parameter redshift-dependent one, we propose a new fitting formula that improves the fit to the growth of structure among Horndeski models by reducing the median goodness-of-fit by 40 times, assuming future Stage IV and V surveys.

Finally, in Chapter 5, we summarize the work presented in this dissertation, place them in the broader context of endeavors to understand the nature of dark energy, and implications for future research.

CHAPTER 2

Misinterpreting Modified Gravity as Dark Energy: a Quantitative Study

Over the past two decades, huge efforts have been made to understand the physical nature of the accelerated expansion of the Universe, both on the observational and on the theoretical front.

On the theory side, many modifications to general relativity have been made so that a late-time cosmic acceleration can naturally arise from within the theory. The volume of possible modified-gravity theories is enormous, and our understanding of this theory space up till today is still limited as studying the observational implications of each theory case-by-case is a very laborious task.

Meanwhile, many photometric, CMB and spectroscopic surveys have provided a huge amount of data that can be used to constrain properties of dark energy. Next generation of surveys will tighten constraints on dark energy and cosmological parameters even further. When analyzing these observational data, however, we typically assume a simple phenomenological dark-energy model — general relativity plus an unknown negative-pressure component with an equation of state $w(z)$.

Experimental data could be fit sufficiently well under this assumption of no modifications to general relativity. But the question that will naturally arise is: what if the true theory of the Universe is some kind of modified-gravity theory? Are we able to see some indications of modified gravity in standard cosmological analysis even though no modification is assumed?

In this chapter, for the first time to our knowledge, we set out to answer this question by constructing a quantitative mapping showing how modified gravity models look when (mis)interpreted within the standard unmodified-gravity analysis. We particularly trained and implemented a machine learning algorithm to facilitate this mapping process.

2.1 Introduction

Overwhelming observational evidence for the current acceleration of the universe presents one of the most outstanding theoretical challenges in all of cosmology and physics [80, 109]. The physical mechanism for the apparent acceleration remains fundamentally mysterious. It could be given by the presence of the cosmological-constant term in Einstein's equations, but the tiny size of the constant presents an apparently insurmountable challenge [210, 52]. A number of dark energy models beyond the cosmological constant have been proposed as well [60]. Similarly, the accelerated expansion could be that gravity is modified on large scales [57, 116, 194], but thus far there is no direct evidence for such a modification.

The difficulty with studying modified-gravity models with data is that the space of possibilities is enormous. There are many completely distinct classes of models to modify gravity and, in each, a large number of possible parameterizations. Constraining any *one* of those modified-gravity model parameterizations with large-scale structure also presents a challenge, for the following reasons: i) modified-gravity-model predictions for nonlinear clustering are, with a few exceptions, not available at all; and ii) the linear-theory predictions generally need to be validated by (modified-gravity) N-body simulations, as e.g. galaxy bias in these models may differ from that in standard gravity (for example [24, 143]). Tests of modified gravity with the cosmic microwave background (CMB) are a little easier as one only needs linear-theory predictions and there is no galaxy bias, but the large scale of possible modified-gravity theories still presents a major obstacle.

As a consequence of these challenges, the majority of confrontations of theory with data has not encompassed models of modified gravity. Instead, most analyses consider simple phenomenological descriptions of the dark-energy sector, such as the model with a cosmological constant (ΛCDM), and that with constant dark-energy equation of state parameter w (wCDM) [206]. Also popular is the time-varying parameterization of the dark-energy equation of state [135] that allows for the dynamics, $w(a) = w_0 + w_a(1 - a)$, where a is the scale factor and w_0 and w_a parameters to be constrained by the data. Modified gravity has typically been constrained only for very specific models (e.g. Σ, μ parameterizations of the gravitational potentials, [216, 63, 166]). There have been attempts to constrain individual modified-gravity models [215, 51, 91, 31, 219, 172, 64, 62, 217, 171, 32, 95, 183, 115, 147, 218, 21, 13, 4, 150, 197, 16, 201, 128] or even reconstruct the temporal behavior of certain models [170, 165], but canvassing the space of modified-gravity theories is challenging because that space is extremely large and difficult to constrain with currently available cosmological surveys.

In this paper we aim to answer a fundamental question:

What happens when the data is analyzed assuming smooth dark energy and the universe is dominated by modified gravity?

Such a scenario will clearly lead to an overall biased estimate of the inference of the cosmological model; see for example Figure 1 in Ref. [107]. Yet it would be very useful to know if modified-gravity theories lead to *generic* shifts in the cosmological parameters relative to their true values.

For example, it could be that a departure of the equation of state w relative to its ΛCDM value of -1 indicates modified gravity. Or, that the currently observed Hubble tension — the discrepancy between measurements of H_0 from the distance ladder and the CMB — is a signature of modified gravity (something that a number of papers in the literature have explored, e.g. [134, 47]). It would be extremely useful to have knowledge of whether there are any *generic* parameter shifts that modified gravity typically induces if analyzed assuming the standard unmodified model.

To address the highlighted question above, we opt for a forward-modeling approach. We wish to generate a large number of modified-gravity models, coming perhaps from different *classes* of such models, and compute the cosmologically observable quantities. We then analyze those observables using some assumed future data, consisting of the cosmic microwave background, baryon acoustic oscillations, and type Ia supernova (these data are further discussed in Sec. 2.3). Crucially, when analyzing these data we assume unmodified-gravity, i.e. the ΛCDM or the w_0w_aCDM model. We can thus assess the bias in all cosmological parameters, relative to their true values, due to the fact that data were analyzed using a wrong model. We then iterate the procedure many times. This informs us about what range of values for the standard (unmodified-gravity) cosmological parameters are inferred when the universe is subject to modified gravity.

One important decision in this procedure is to choose a general framework of modified-gravity theories from which to sample individual models. Here we opt to utilize a familiar approach from particle physics (and, as of recently, cosmology) — the Effective Field Theory (EFT). Here our approach is to utilize the EFT of Dark Energy (EFTDE) [152, 90, 45, 83], where (universality) classes of models are established through a grouping of terms in the fundamental Lagrangian. This has the advantage that instead of considering one particular model at a time, one can consider an entire class of models with similar properties. One example of such a universality class in the EFTDE are the Horndeski models of modified gravity. In fact, here we will focus our investigation on the Horndeski sub-class of EFTDE models as described in Sec. 2.2.1 below.

Our procedure in this paper also includes a solution to a pesky technical problem: how to fit the eight-dimensional w_0w_aCDM models to each of the thousands of EFTDE models. This is computationally expensive because traditional Boltzmann-Einstein equation solvers used for this purpose such as `CAMB` are slow for what we are trying to do here. We thus employ and adapt an existing emulator package to speed up this fitting process. This development enables us to obtain our numerical results with relatively modest computer resources. Most readily available cosmological emulators for the CMB power spectrum (such as [189] and [198]) function for a fixed set of parameters – usually the standard six cosmological parameters – while our methodology of setting up the emulator allows a much greater freedom in including parameters.

The paper is organized as follows. Sec. 2.2 is divided into two parts and gives an overview of our overall methodology. The first half explains how we select a subset of Horndeski gravity

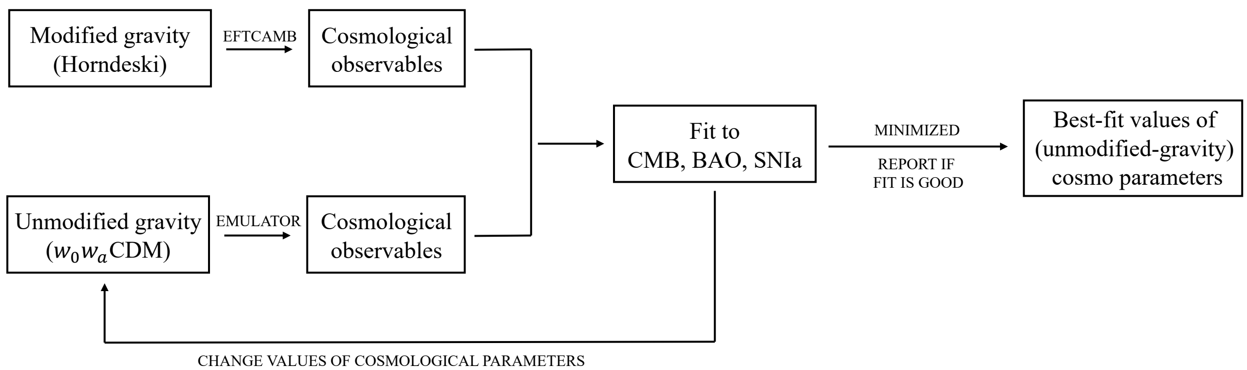

Figure 2.1: A schematic describing our pipeline to interpret and fit a modified gravity data vector with an (unmodified-gravity) dark energy model. We show the complete procedure for a single Horndeski data vector, corresponding to one point in our final best-fit parameter values in the plots that follow. We repeat this procedure procedure for thousands of Horndeski models.

models and compute cosmological observable quantities from them. The second half goes over methods (including a brief introduction on the emulation technique) used to reinterpret the data vectors generated by Horndeski models by fitting them with an unmodified-gravity w_0waCDM model. Sec. 2.3 introduces the cosmological probes and assumed future experiment data used in the fitting process. Sec. 2.4 discusses and summarizes the results. We conclude in Sec. 2.5.

2.2 Methodology Overview

As discussed in Sec. 2.1, we generate the data vector assuming a modified-gravity model, but analyze it assuming unmodified gravity in the w_0w_aCDM model. Specifically, for each Horndeski data vector, we generate a CMB angular power spectrum predicted by this theory through a package `EFTCAMB`[1], and also generate predictions for BAO and SNIa. Then, we fit to this synthetic data with w_0w_aCDM cosmological models. We record the best-fit parameters of such w_0w_aCDM model, and move on to the next iteration, selecting a new EFTDE model. Figure 2.1 shows our approach schematically.

We now describe the key pieces of our approach: the modified-gravity theory to generate fake data, and the unmodified-gravity theory to analyze it with. For both modified and unmodified-gravity aspects of our analysis, we also discuss the numerical tools that enable the feasibility of our analysis.

[1] https://eftcamb.github.io

2.2.1 Generating data: modified gravity

Inspired by the EFT formalism for Inflation by Cheung et. al. [55], the EFTDE provides a universal description for all viable dark energy and modified gravity models [152, 90, 45] Working in unitary gauge, the EFTDE action takes the form [45],

$$\begin{aligned} S &= \int d^4x\sqrt{-g}\left[\frac{1}{2}m_0^2\Omega(t)R - \Lambda(t) - c(t)g^{00} + \frac{M_2^4(t)}{2}(\delta g^{00})^2\right. \\ &- \frac{\bar{M}_1^3(t)}{2}\delta K\delta g^{00} - \frac{\bar{M}_2^2(t)}{2}\delta K^2 - \frac{\bar{M}_3^2(t)}{2}\delta K_\nu{}^\mu\delta K_\mu{}^\nu \\ &+ \left.\frac{\hat{M}^2(t)}{2}\delta R^{(3)}\delta g^{00} + m_2(t)\partial_i g^{00}\partial^i g^{00} + \mathcal{L}_m\right], \end{aligned} \tag{2.1}$$

where $\delta g^{00} = g^{00}+1$ is the perturbation to the time component of the metric, $R^{(3)}$ is the perturbation to the spatial component, and $\delta K_{\mu\nu}$ is the perturbation of the extrinsic curvature. The background evolution depends on three functions, $c(t)$, $\Lambda(t)$, and $\Omega(t)$. Two of the three can be constrained using the Einstein equations and are equivalent to the energy density and pressure. The third function, $\Omega(t)$, parameterizes the effect of modified gravity [45]. In what follows we will take $\Omega = 1$, thus explicitly fixing the background to ΛCDM[2]. The rest of the EFT functions describe perturbations about this background and correspond to observables that we are interested in when comparing to observations. For a summary of all models included in this very general formalism, refer to Table 1 in [141]. Again, we note that the EFTDE includes such well-known simpler models as DGP and $f(R)$ (see [90, 45] for a discussion).

Here we specialize in a very broad subset of models captured by the EFTDE approach — Horndeski models (for a general review of this class of models see [124] and references therein). These models have been of particular interest because even if one does not take the EFTDE approach they have stable, second order equations of motion, leading to a well defined Cauchy problem and viable models of modified gravity. However, within the EFTDE approach, this is guaranteed from the outset. This universality class of models is obtained when the following relations are imposed on EFTDE functions

$$2\hat{M}^2 = \bar{M}_2^2 = -\bar{M}_3^2; \qquad m_2 = 0. \tag{2.2}$$

We will be interested in the linear-theory predictions of Horndeski models as given by the EFTCAMB code [101]. There, the EFTDE is described in terms of dimensionless parameters γ_i

[2] m_0 is the mass scale of the theory and is equivalent to $m_{\rm pl}$ when $\Omega(t) = 1$.

defined as

$$\begin{aligned} \gamma_1 &= \frac{M_2^4}{m_0^2 H_0^2}, \quad & \gamma_2 &= \frac{\bar{M}_1^3}{m_0^2 H_0}, \quad & \gamma_3 &= \frac{\bar{M}_2^2}{m_0^2}, \\ \gamma_4 &= \frac{\bar{M}_3^2}{m_0^2}, \quad & \gamma_5 &= \frac{\hat{M}^2}{m_0^2}, \quad & \gamma_6 &= \frac{m_2^2}{m_0^2}. \end{aligned} \tag{2.3}$$

In terms of these new variables, the Horndeski models are obtained from the full EFTDE with these conditions

$$2\gamma_5 = \gamma_3 = -\gamma_4; \;\; \gamma_6 = 0. \tag{2.4}$$

Our approach is therefore to canvass through the possible Horndeski models by varying $\gamma_i(t)$ for $i = 1, 2, 3$.

There is an important caveat to our assumptions about the Horndeski parameter space. It has been argued that there exists a strong additional constraint on the parameter γ_3, based on the comparison of the speed of light and gravitational-wave speed of propagation from the event GW170817 discovered by LIGO (see e.g. [125]). Because γ_3 is related to the speed of the gravitational wave c_T (see e.g. [141] and references therein), such a constraint would impose a strong prior that γ_3 is very close to zero. However, there are various theoretically motivated possible exceptions to this constraint [66, 20, 30]. With that in mind, and to make our analysis broadly applicable and not tied to specific theoretical models, we opt to keep γ_3 as a free parameter without any gravitational-wave-inspired prior. [To reinsert this prior, one could simply inspect and analyze our results evaluated for the small range of γ_3 around zero, although of course such an analysis will necessarily have a lower statistics than one where the γ_3 prior has been assumed from the beginning.]

In our approach, we require Horndeski models to successfully reproduce an approximate ΛCDM background and then focus on the connection between the perturbations and observations. That is, we take the equation of state to be near that of a pure cosmological constant (always with $w > -1$), which in terms of the EFTDE parameters corresponds to a nearly vanishing value of the parameter c, Λ nearly constant and Ω close to unity in the EFTDE. This is a subset of Horndeski models, but corresponds to those consistent with a viable alternative to ΛCDM as required by data. Our approach is similar to that of the EFT of inflation where one assumes an inflationary background and then focuses on the perturbations (observables) [55].

With the background constrained to a ΛCDM universe, we now consider allowed variations in the perturbations of our Horndeski models. Recall that there are three free time-dependent EFTDE functions in Horndeski gravity, $\gamma_i(t)$ for $i = 1, 2, 3$. The first task is to parametrize the time-dependence of these functions, which we take as

$$\gamma_i(a) = \gamma_{i,0}\, a, \tag{2.5}$$

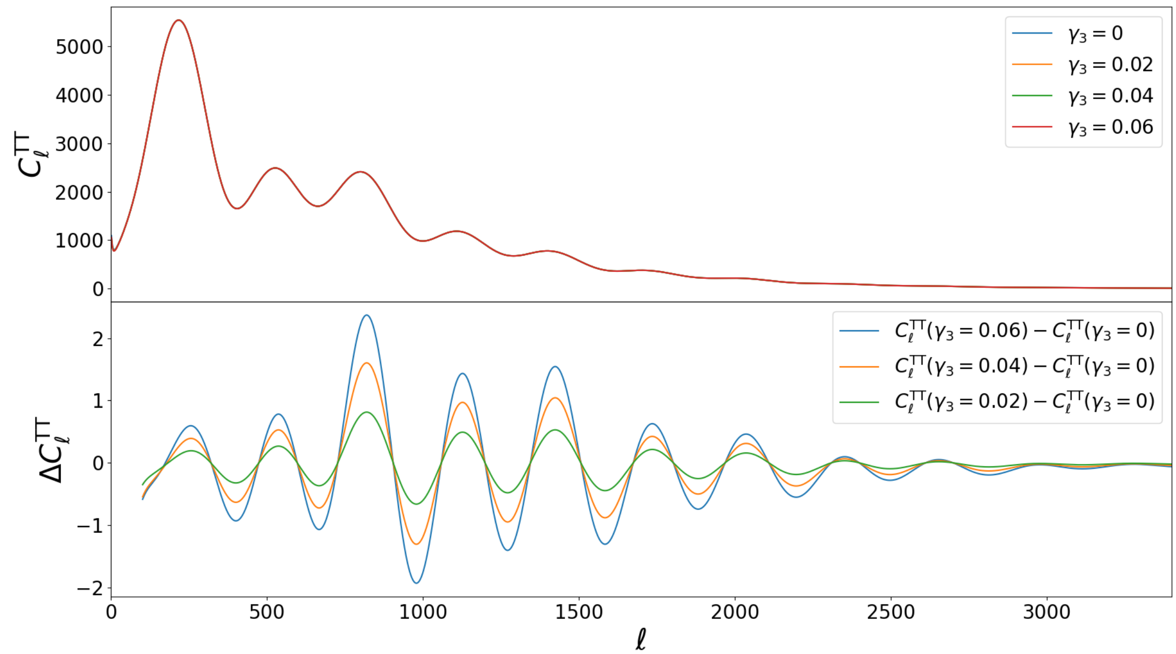

Figure 2.2: CMB temperature power spectrum generated from EFTCAMB with varied values of the Horndeski parameter $\gamma_{3,0}$ in Eq. 2.6 while fixing $\gamma_{1,0} = \gamma_{2,0} = 0$. Increasing the value of $\gamma_{3,0}$ makes the peaks higher and troughs lower.

reproducing the CMB power spectra that are closest to current observations.

Next, we determine the range of the coefficients $\gamma_{i,0}$. In Sec. 2.2.2, we describe how we set a 5σ requirement for each unmodified-gravity model as to be a good fit for the Horndeski model. By phenomenologically studying sample fits to various Horndeski models, we determine that the Horndeski parameter space restricted to the range

$$\gamma_{1,0} \leq 1; \quad \gamma_{2,0} \leq 0.1; \quad \gamma_{3,0} \leq 0.06, \tag{2.6}$$

encompasses models that are sufficiently in correspondence to unmodified-gravity models, using criteria that we now describe. In Fig. 2.2, we display how different values of the Horndeski parameter $\gamma_{3,0}$, which is of particular interest to our analysis in the later sections, impact the peak height of CMB temperature power spectrum.

2.2.2 Analyzing data: unmodified gravity

Our main goal is to fit simulated modified-gravity data using standard dark energy (unmodified-gravity) models. To be as general as possible, we fit w_0w_aCDM cosmological models to the data, with parameters

$$\{p_i\} = \left\{\omega_b, \omega_c, H_0, \ln(10^{10}A_s), n_s, \tau_{\rm reio}, w_0, w_a\right\} , \tag{2.7}$$

where $\omega_b \equiv \Omega_b h^2$ is the physical baryon density, $\omega_c \equiv \Omega_c h^2$ is the physical cold dark matter density, H_0 is the Hubble constant, A_s is the amplitude of the primordial power spectrum at pivot wave number $k_{\rm piv} = 0.05\ {\rm Mpc}^{-1}$, n_s is the scalar spectral index, $\tau_{\rm reio}$ is the optical depth to reionization, and (w_0, w_a) are the parameters describing the dark energy equation of state.

For each Horndeski data vector generated using `EFTCAMB` with assumptions as described in Sec. 2.2.1, we need to find the best-fit w_0w_aCDM model. We thus need to be able to produce the supernova and BAO observables (distances and the Hubble parameters) and the CMB angular power spectrum in w_0w_aCDM models many times for a single Horndeski model. Calculating distances is straightforward, while the CMB temperature and polarization angular power spectra are typically obtained using the standard Boltzmann-Einstein solver `CAMB`. Here we employ an emulator due to computational cost reasons explained above.

Given a single Horndeski data vector and predictions from unmodified-gravity models, we minimize the total χ^2, defined as a sum of chi-squareds for each cosmological probe in Sec. 2.3 and thus find the best-fitting parameters. To carry out chi-squared minimization in our eight-dimensional parameter space given in Eq. (2.7), we adopt iminuit[3]. This optimizer allows us to restart the minimization process from the ending point of the last minimization, re-doing the minimization five times for each EFTDE model to improve the result. The allowed ranges for each parameter to explore is set to be 5% smaller than the parameter range specified in Table 2.1.

As alluded to in Sec. 2.2.1, we wish to only use reasonably good fits to our Horndeski data vectors, as an analysis resulting in a bad fit to the data would simply not be allowed to proceed in a realistic situation. To that end, we only accept best-fit w_0w_aCDM models that have a minimized χ^2 within 5σ of the expectation for a chi-square distribution of $N_{\rm dof}$ degrees of freedom. Our simulated cosmological data, described below in Sec. 2.3, have $N_{\rm dof} = 7492$[4]. Recall that our simulated Horndeski data vectors are noiseless, so that a perfect fit would have $\chi^2 = 0$. With this information, the "5-σ" limit to a cosmological fit corresponds to chi-square limit of

$$\chi^2 < 650 \quad \text{(acceptable fit).} \tag{2.8}$$

If the best fit to a given Horndeski model is worse than this, we judge that such a model would not be interpreted as a viable cosmological model. We also exclude results for models where one or more parameters reach the upper or lower bounds of their respective parameter range given in

[3]https://iminuit.readthedocs.io/en/stable/

[4]We used 3×2500 multipoles from temperature and polarization spectra respectively as our data, and it was constrained by 8 parameters as listed in Table 2.1.

Table 2.1 as it indicates that this model cannot be fitted by a w_0w_aCDM model within the range of current measurements well; this affects about 21 percent of Horndeski models that we considered.

In our model-fitting procedure, the main challenge is the significant computational cost. Consider that `CAMB`[5] takes about 1.5 second to produce a w_0w_aCDM CMB angular power spectrum. For a single Horndeski model, the minimizer requires of order 1,000 w_0w_aCDM model evaluations, and our overall goal is to produce results for 10,000 or more Horndeski models. To addrress this challenge we constructed an emulator to generate model predictions for w_0w_aCDM cosmologies. An emulator is essentially an interpolator. Given a set of grid points in an N-dimensional parameter space and corresponding outcomes evaluated at these points, the emulator interpolates to produce an expected outcome on arbitrary points off the grid (but still within its boundaries). In our case, the grid is the eight-dimensional parameter space listed in Eq. (2.7). Since the spectrum is obtained through interpolation, and not from solving the Boltzmann-Einstein equation, this method generates spectra much faster. The emulator we developed builds on the `EGG`[6] package.

Table 2.1: Fiducial values of cosmological parameters and their ranges used in training the emulator

Parameter	**Fiducial value**	**Parameter range**
$\Omega_b h^2$	0.02222	(0.02147, 0.02297)
$\Omega_c h^2$	0.1197	(0.1137, 0.1257)
A_s	2.196 $\times 10^{-9}$	(1.132 $\times 10^{-9}$, 2.703 $\times 10^{-9}$)
H_0	67.5	(64.8, 70.2)
n_s	0.9655	(0.9445, 0.9865)
τ	0.06	(0.0235, 0.0965)
w_0	-1	(-1.5, -0.5)
w_a	0	(-0.5, 0.5)

- *Parameter ranges:* The prior range for each of the first six parameters in Eq. (2.7) is set to $\pm 5\sigma$ around their fiducial values, where σ is the 68% marginalized error on each corresponding parameter from the Planck 2018 analysis using the `Plik` likelihood [13]. For the two dark energy parameters w_0 and w_a, we adopt ranges $-1.5 \leq w_0 \leq -0.5$ and $-0.5 \leq w_a \leq 0.5$. A summary of all parameter ranges are in Table 2.1.

- *Parameter grid values:* A uniform grid is not ideal as, for a reasonable number of values in each parameter, it leads to a large number of grid points and slow emulator training.

[5]https://camb.info
[6]https://github.com/lanl/EGG

Therefore, we employ the Latin Hypercube sampling (LHS) which is known to be very efficient for emulators [93]. The points in LHS are stratified along the direction of each axis in a multi-dimensional space. This design is mathematically equivalent to forming a $n \times m$ matrix such that every column of this matrix is a unique permutation of $\{1, ..., n\}$. There are a number of strategies to design an LHS[7], and the one we use is provided by a python package `pyDOE`[8]. This package allows us to specify the number of parameters and the number of grid points with much greater flexibility.

- *Training:* To "train" an emulator is to assign the corresponding outcomes to the grid points. Here, we use `CAMB` to calculate the CMB temperature and polarization angular power spectra (TT, EE, and TE) and assign them to the corresponding grid points. During training, the emulator uses a Markov chain Monte Carlo type process to find and optimize an interpolative function that describes the nonlinear relationship between the grid points and their corresponding CMB power spectra.

- *Testing emulator's performance:* The performance of an interpolation under a given LHS setup can be determined quantitatively by comparing the interpolated power spectrum at an arbitrary point in parameter space with the one generated directly by `CAMB`. Adopting a test similar to the one used in [189], we randomly selected 100 points from the allowed parameter space in Table 2.1 and calculated the fractional difference between the angular power spectrum interpolated by the emulator and the power spectrum generated by `CAMB`. For the temperature power spectrum, the emulator's fractional errors within the first and third quartile are 0.3% for multipoles $\ell > 8$. For the polarization power spectra EE and TE, the fractional errors are 0.5% for $\ell > 25$ and 3.5% for $\ell > 55$ respectively.

  The performance of the interpolation is mostly determined by the number of grid points in the LHS design and the number of MCMC iterations when training the emulator. A larger number of grid points and a higher number of steps in the MCMC-type process during training would both improve the performance of interpolation, but at the cost of a slower evaluation per model. In this work, we use 570 grid points and 1000 iterations. With the current setup, each interpolation takes about 0.3 seconds to finish, which is five times faster

[7] We did not opt for the commonly used orthogonal-array Latin hypercube (OALH) design. This is because using OALH, one relies on the existing library of orthogonal arrays, and the latter does not offer much flexibility to change the number of parameters and the number of samples (i.e. grid points). Specifically, there exist only a few available orthogonal arrays for an eight-dimensional parameter space, and the allowed sample numbers for these arrays are too low for our purposes. The strategy we adopt, as discussed in the text, is not as optimal as the OALH design in its coverage of the parameter space, but its performance can be easily improved through increasing the number of grid points.

[8] `Designs of Experiments for Python`, https://pythonhosted.org/pyDOE/randomized.html#latin-hypercube

Table 2.2: A summary table of the probes and data sets used to determine the best-fit parameters for a certain EFTDE model.

Probes	**Experiment**	**Measurements**	**Details**
CMB	Stage-4	angular power spectrum C_ℓ (data error: Eq. 2.12)	from $l = 2$ to $l = 2500$ temperature (TT) and polarization (EE and TE)
SNIa	WFIRST	apparent magnitude $m(z)$ (data error: Eq. 2.17)	16 effective SNe Ia in bins of $\Delta z = 0.1$ from $z = 0.1$ to $z = 1.6$ with 0.4% error
	Pan-STARRS1	apparent magnitude $m(z)$ (data error: Ref. [190])	870 supernovae from $z = 0.00508$ to $z = 1.06039$
BAO	DESI	angular diameter distance $D_A(z)$ Hubble parameter $H(z)$ (data error: Ref. [10])	13 redshift bins of size $\Delta z = 0.1$ from $z = 0.65$ to $z = 1.85$

than using CAMB.

Under this setup, we further validate the emulator's accuracy by testing its ability to recover the input values used to generate the data. Further details are explained in Appendix A.1.

2.3 Simulated Data

In this section, we will discuss the probes and experiment specifics we used to determine the best-fit values of dark energy parameters w_0 and w_a.

We use cosmic microwave background, baryon acoustic oscillations (BAO), and type Ia supernovae (SN Ia) as our data. In this first paper on the topic, we opt not to use weak gravitational lensing or galaxy clustering. As mentioned in the introduction, this is due to the significant additional complexity in modeling clustering, which for starters one typically needs to restrict to linear scales only in modified-gravity models as obtaining reliable nonlinear predictions is very challenging. It is our goal to set up a robust proof-of-principle analysis pipeline with the CMB, BAO and SN Ia alone. In a future publication, we will add the galaxy clustering and weak lensing (and, ideally, the full "3x2" pipeline that also includes galaxy-galaxy lensing).

A summary of the probes used can be seen in Table 2.2. We now describe them in more detail.

2.3.1 CMB

We assume a CMB survey modeled on expectations from CMB-S4 [132]. The survey covering 40% of the sky, with other specifications given below. We utilize scales out to maximum multipole $\ell_{\rm max} = 2500$, consistent with the cutoff in Planck 2018 results[13]. Assuming a Gaussian likelihood $\mathcal{L}$, the chi squared, $\chi^2 \equiv -2\ln\mathcal{L}$, is given by

$$\chi^2_{\rm CMB} = \sum_{\ell=2}^{\ell=2500} \left(\mathbf{C}_\ell^{\rm data} - \mathbf{C}_\ell^{\rm th}\right)^T \, {\rm Cov}_\ell^{-1} \left(\mathbf{C}_\ell^{\rm data} - \mathbf{C}_\ell^{\rm th}\right), \tag{2.9}$$

where $\mathbf{C}_\ell^{\rm th}$ is the data-vector corresponding to theory ($w_0 w_a$CDM) prediction, and $\mathbf{C}_\ell^{\rm data}$ are the data which, recall, are produced assuming the EFT model. Both the theory and the data $\mathbf{C}_\ell$ are composed of parts corresponding to temperature-temperature (TT), temperature-polarization (TE), and polarization-polarization (EE) correlations:

$$\mathbf{C}_\ell \equiv \begin{pmatrix} C_\ell^{TT} \\ C_\ell^{EE} \\ C_\ell^{TE} \end{pmatrix}. \tag{2.10}$$

The overall covariance matrix ${\rm Cov}_\ell$ is diagonal between the different multipoles. At each multipole, the covariance for the data vector $\mathbf{C}_\ell^{\rm data}$ is given by (e.g. [132])

$$\begin{aligned} {\rm Cov}_\ell &= \frac{2}{(2\ell+1) f_{\rm sky}} \\ &\times \begin{pmatrix} (\tilde{C}_\ell^{TT})^2 & (\tilde{C}_\ell^{TE})^2 & \tilde{C}_\ell^{TT}\tilde{C}_\ell^{TE} \\ (\tilde{C}_\ell^{TE})^2 & (\tilde{C}_\ell^{EE})^2 & \tilde{C}_\ell^{EE}\tilde{C}_\ell^{TE} \\ \tilde{C}_\ell^{TT}\tilde{C}_\ell^{TE} & \tilde{C}_\ell^{EE}\tilde{C}_\ell^{TE} & \frac{1}{2}[(\tilde{C}_\ell^{TE})^2 + \tilde{C}_\ell^{TT}\tilde{C}_\ell^{EE}] \end{pmatrix}. \end{aligned} \tag{2.11}$$

The elements of this covariance matrix are explicitly

$$\begin{aligned} \tilde{C}_\ell^{TT} &= C_\ell^{TT} + N_\ell^{TT} \\ \tilde{C}_\ell^{EE} &= C_\ell^{EE} + N_\ell^{EE} \\ \tilde{C}_\ell^{TE} &= C_\ell^{TE}, \end{aligned} \tag{2.12}$$

and the noise terms are

$$
\begin{aligned}
N_\ell^{TT} &= \Delta_T^2 \exp\left[\frac{\ell(\ell+1)\theta_{\rm FWHM}^2}{8\ln 2}\right] \\
N_\ell^{EE} &= 2 \times N_\ell^{TT},
\end{aligned}
\tag{2.13}
$$

where $\Delta_T = 1\,\mu K$, $\theta_{\rm FWHM} = 8.7 \times 10^{-4}$ radians, and assume $f_{\rm sky} = 0.4$, using the specifics of the Stage-4 experiment [132].

We generate the data vector $\mathbf{C}_\ell^{\rm data}$ (for each ℓ) using `EFTCAMB`, for a given cosmological model as discussed in Sec. 2.2.1. This is an important step, as CMB is the only part of our simulated data that is directly affected by modified gravity.

We generate *noiseless* data vectors — that is, the final $\mathbf{C}_\ell^{\rm data}$ used in the likelihood are precisely centered on theory, with no stochastic noise. This assumption is justified because we are not interested in statistical errors on the infered parameters, but rather only at the best-fit parameters (for a given simulated Horndeski model). Had we included stochastic noise, we could have still obtained the results that we are after, but it would have required running a number of statistical realizations of data vectors for a given Horndeski model in order to account for stochasticity in the data.

2.3.2 SNIa

Type Ia supernovae (SNIa) are sensitive to distances alone. Because in our generated data we fix the background cosmology to ΛCDM and only vary the perturbations according to modified gravity, SNIa data vector is not directly sensitive to modified gravity. Nevertheless, SNIa are very useful in pinning down the cosmological parameters and breaking degeneracies between them, and thus helping isolate the effects of modified gravity on data analyzed assuming $w_0 w_a$CDM.

Assuming again a gaussian likelihood, the chi squared for SNIa measurements is determined by

$$
\chi^2_{\rm SN}(\{p_i\}, \mathcal{M}) = (\mathbf{m}^{\rm data} - \mathbf{m}^{\rm th})^T {\rm Cov}^{-1} (\mathbf{m}^{\rm data} - \mathbf{m}^{\rm th}),
$$

where $\mathbf{m}^{\rm data}$ is the apparent magnitude of simulated data which is calculated based on the cosmology in each fit to the Horndeski model. The theoretical magnitude $\mathbf{m}^{\rm th}$ is, conversely, calculated based on the fiducial $w_0 w_a$CDM cosmological model:

$$
m^{\rm th}(z) = 5\log_{10}[H_0 d_L(z, \{p_i\})] + \mathcal{M} \tag{2.14}
$$

where d_L is the luminosity distance, and $\mathcal{M} = M - 5\log_{10}(H_0 \times 1{\rm Mpc}) + 25$ is a nuisance parameter that always needs to be marginalized over in a SNIa analysis. We can analytically marginalize over

$\mathcal{M}$ and obtain a marginalized effective χ^2

$$\chi^2_{\text{SN, marg}} = a - \frac{b^2}{c}, \tag{2.15}$$

where

$$\begin{aligned} a &= (\mathbf{m} - \mathbf{m}^{th})^T \text{Cov}^{-1} (\mathbf{m} - \mathbf{m}^{th}) \\ b &= \mathbf{1}^T \text{Cov}^{-1} (\mathbf{m} - \mathbf{m}^{th}) \\ c &= \mathbf{1}^T \text{Cov}^{-1} \mathbf{1}, \end{aligned} \tag{2.16}$$

where **1** is a unit vector.

We employed the SNIa redshift bins and the covariance matrix as forecasted for the WFIRST satellite [97]. The covariance matrix is diagonal between different bins, and is calculated as a combination of systematic and statistical errors. In a given redshift bin,

$$\sigma_{\text{tot}} = (\sigma^2_{\text{sys}} + \sigma^2_{\text{stat}})^{1/2}, \tag{2.17}$$

where

$$\begin{aligned} \sigma_{\text{sys}} &= \frac{0.01(1+z)}{1.8} \\ \sigma_{\text{stat}} &= \frac{(\sigma^2_{\text{meas}} + \sigma^2_{\text{int}} + \sigma^2_{\text{lens}})^{1/2}}{N^{1/2}_{\text{SN}}}. \end{aligned} \tag{2.18}$$

Here, $\sigma_{\text{meas}} = 0.08$, $\sigma_{\text{int}} = 0.09$, $\sigma_{\text{lens}} = 0.07z$, and N_{SN} is the number of supernovae in that redshift bin.

We have also incorporated redshift bins and the corresponding covariance matrix from measurements at low redshift by Pantheon dataset [190], which includes 870 supernovae. The covariance matrix for this data set is diagonal, and the error at each redshift is given by Pantheon as well.

2.3.3 BAO

Baryon acoustic oscillations (BAO) — wiggles in the matter power spectrum due to photon-baryon oscillations prior to recombination — are a powerful cosmological probe. Much like SNIa, they probe geometry, and are sensitive to the angular-diameter distance $D(z)$ and Hubble parameter $H(z)$ evaluated at the redshift of tracer galaxies in question. Often, the general analysis of the BAO provides precisely these ”compressed quantities” for one or more effective redshifts, which in turn can be used to constrain a cosmological model.

Here we assume the $D(z)$ and $H(z)$ measurements that are forecasted to be measured DESI experiment [10]. The measurements of both the distances and the Hubble parameters are each reported separately in 13 redshift bins; we thus organize these measurements in data vectors **D** and **H** that each have 13 elements. As before, we generate synthetic noiseless data ($\mathbf{D}^{\mathrm{data}}$ and $\mathbf{H}^{\mathrm{data}}$) assuming Horndeski models, and analyze it using theoretically computed quantities ($\mathbf{D}^{\mathrm{th}}$ and $\mathbf{H}^{\mathrm{th}}$) that assume the w_0w_aCDM model.

The goodness-of-fit for BAO is written down in a similar way as for the CMB and SNIa

$$\begin{aligned}\chi^2_{\mathrm{BAO}}(\{p_i\}) = (\mathbf{D}^{\mathrm{data}} - \mathbf{D}^{\mathrm{th}})^T \mathrm{Cov}_D^{-1} (\mathbf{D}^{\mathrm{data}} - \mathbf{D}^{\mathrm{th}}) \\ + (\mathbf{H}^{\mathrm{data}} - \mathbf{H}^{\mathrm{th}})^T \mathrm{Cov}_H^{-1} (\mathbf{H}^{\mathrm{data}} - \mathbf{H}^{\mathrm{th}}),\end{aligned} \tag{2.19}$$

where Cov_D and Cov_D are respectively the 13×13 covariance matrices for the distance and Hubble parameter measurements, which are diagonal. We adopt these matrices also from DESI forecasts [10].

2.4 Results and Discussions

Our results are summarized in Fig. 2.3. Here we show the eight-dimensional space of w_0w_aCDM models that were fit to Horndeski data vectors. Each point corresponds to values of the best-fit w_0w_aCDM model for a given Horndeski model. We show results for a total of 15186 Horndeski data vectors which passed our criteria laid out in Sec. 2.2.2. We show all possible 2D planes of cosmological parameters, as well as histograms of the distributions in each parameter on the diagonal. The axis limits are chosen so that they indicate the range within which each parameter is allowed to vary during the minimization. The grey crosshair in each panel indicates our fiducial cosmology (see Table 2.1), which corresponds to the background cosmology we set in all our Horndeski models.

Note specifically that Fig. 2.3 does *not* show any kind of parameter constraint — that is, no ”error bars” are represented here. Rather, in each parameter panel of the Figure, the distribution of points relative to the crosshair demonstrates how values of the respective parameters shift relative to their true values when modified gravity (Horndeski) theories are incorrectly interpreted as dark energy (w_0w_aCDM). Recall also that these fits are only performed for w_0w_aCDM models that are decent fits to Horndeski data vectors, judged by the criterion in Eq. (2.8), mimicking the decision point that would be applied in an analysis of real data. Finally, the density of points in Fig. 2.3 is not particularly important, as it merely reflects the metric on our prior in the space of models (e.g. the fact that we used a flat prior in the parameters γ_i rather than, say, a log prior). What we are interested instead is the overall extents and shapes of the clouds of points.

The most apparent observation from Fig. 2.3 is that the biases in w_0w_aCDM parameters, relative to their true values, carve out very specific directions in the parameter space. Table 2.3 summarizes

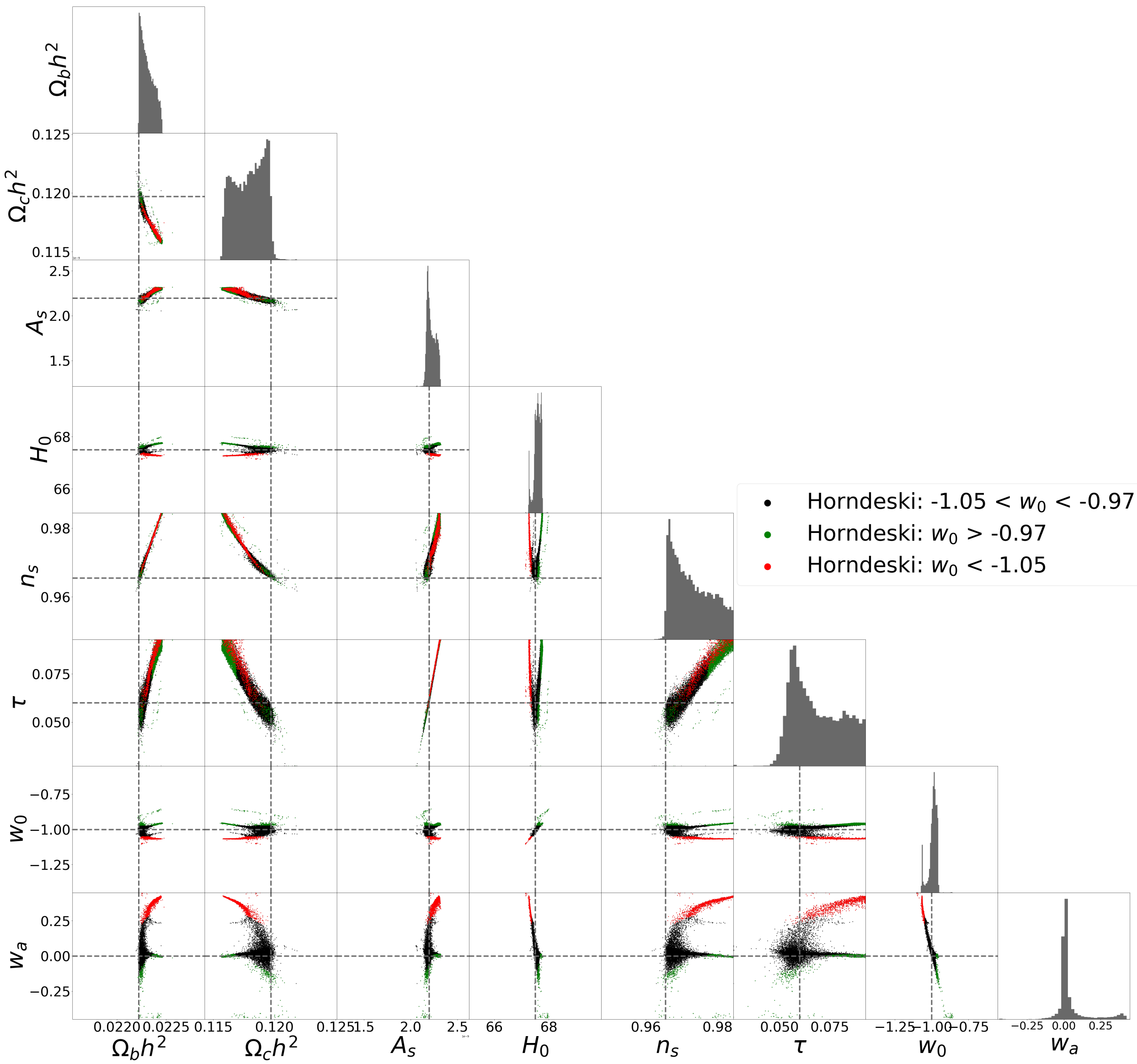

Figure 2.3: Best-fit values and histograms of cosmological parameters and dark energy sector parameters obtained from fitting to 15186 Horndeski models with a w_0w_aCDM cosmology. Branches shown in the panels along the rows of H_0, w_0 and w_a can be separated by values of w_0, as indicated by red and green points.

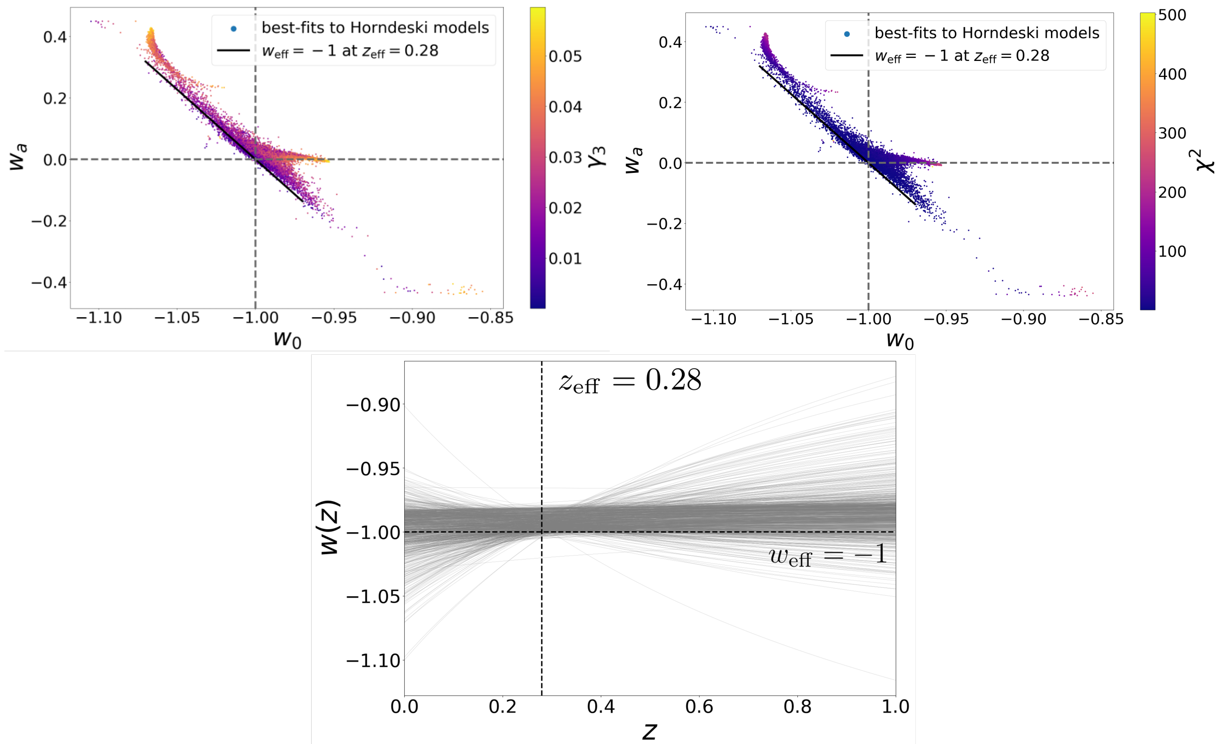

Figure 2.4: *Top left panel:* The w_0-w_a plane from Figure 2.3, where each point is colored by the γ_3 function of the corresponding Horndeski data vector that was fitted with a w_0w_aCDM cosmology. *Top right panel:* The same as the left panel but each point is colored by the χ^2 value that quantifies the difference between the best-fit power spectrum and the Horndeski data vector. *Bottom panel:* Equation of state $w(z)$ for 1000 randomly selected models (corresponding to a subset of points in the purple-pink region in the left panel). Notice that the equation-of-state curves intersect around an effective redshift $z_{\rm eff} = 0.28$, at the value of the effective equation of state typically slightly larger than $w_{\rm eff} = -1$.

the directions in which the parameters are shifted. The specific shifts are generally unsurprising, as we would guess that there exist specific degeneracies between Horndeski models and w_0w_aCDM parameters where the former can be interpreted as the latter. Nevertheless, the precision to which the w_0w_aCDM biases are carved out in their respective parameter spaces is remarkable.

The next most noticeable feature of our results are the branchings in the w_0w_aCDM parameter biases. In other words, biases in the parameters trace out multiple (two or three) directions in several 2D parameter planes. This indicates multiple degeneracy directions between shifts in the w_0w_aCDM space and Horndeski models. A very general quantitative expectation for this multi-modality is difficult to establish, but we have nevertheless explored this in some detail. We found that the value of the parameter w_0 — dark energy equation of state value today — is a good predictor for the branchings. Specifically, we found that modified-gravity models that are best fit with, respectively, $w_0 < -1.05$ and $w_0 > 0.97$, lead to two prominent branches that are evident in a number of 2D planes, and that are labeled with green and red points respectively in Fig. 2.3. Conversely, models fit with $-1.05 < w_0 < -0.975$, labeled with black points, form the "core" of the distribution, at the nexus of the two branches.

Closing the analysis of Fig. 2.3, note that the overall biases in the standard-model parameters are, very roughly, comparable to the current statistical uncertainties in these parameters. For example, the range of the scalar spectral index, roughly $[0.96, 0.98]$, is somewhat larger than its present statistical uncertainty, while that in the Hubble constant, $[66.86, 68.43]$, is also somewhat larger than the constraints from Planck 2018 analysis [13]. This is not particularly surprising as we have only shown models whose fit to Horndeski data vectors is "good" as quantified in terms of near-future experimental errors. Nevertheless, this tells us that future constraints on these parameters will likely favor a subset of models shown in Figure 2.3. Future data may thus indicate whether a specific sub-class of modified-gravity models lurks in the data.

Of particular interest to cosmologists is the measured value of the equation-of-state parameters (w_0, w_a). Can these measured values indicate the presence of modified gravity? To help answer this question, we enlarge and display Fig. 2.3's $w_0 - w_a$ plane in the top panels of Fig. 2.4. First, note that the w_0 and w_a values of best-fit unmodified-gravity models are mutually highly correlated. This is entirely expected, as the physically relevant quantity is $w(z)$ at the redshift where best constrained by the data — the effective, or "pivot" redshift [110, 137]. In fact, it turns out that our range of Horndeski models given by Eq. (2.6), the largely one-dimensional direction of best-fit models in $w_0 - w_a$ plane is

$$w_{\text{eff}} = w_0 + w_a(1 - a_{\text{eff}}) \simeq -1 \tag{2.20}$$

with the effective scale factor $a_{\text{eff}} = 0.78$ or redshift $z_{\text{eff}} = 0.28$.

Therefore, the best-fit models do allow variation in w_0 and w_a, but constrained so that the two parameters combine to produce a constant $w(z)$ at some effective redshift. To illustrate this, the black line in both of the top panels of Fig. 2.4 follows combinations of w_0 and w_a that give $w_{\text{eff}} \equiv w(z_{\text{eff}}) = -1$ at effective redshift $z_{\text{eff}} = 0.28$ based on Eq. (2.20). [Note that most best-fit models are actually slightly above the black dashed line, indicating that w_{eff} is slightly larger than -1.] The linear relation in Eq. (2.20) is not unexpected, as it is really the "physical" value of the equation of state w_{eff} at some redshift z_{eff} to which the theory is most sensitive. In our scenario, dark-energy parameters preferentially follow the relation in Eq. (2.20) so as to fit our SNIa and BAO data which are generated using $w = -1$, even while individually departing from the cosmological-constant values of $(w_0, w_a) = (-1, 0)$ in order to fit the CMB data which are generated using Horndeski. Specifically, w_0 and w_a obey a definite one-parameter family of curves for a fixed value of the distance to the last-scattering surface, which the CMB data constrain particularly well [138]. The value of the pivot value that the analysis reports to us, $z_{\text{eff}} = 0.28$, merely reflects the typical redshift to which cosmological SNIa, BAO and CMB data are most sensitive [110].

We shed more light on what best-fit (w_0, w_a) values are favored as fits to Horndeski models in the bottom panel of Fig. 2.4. Here, each curve represents the function $w(z)$ (in the w_0, w_a model) for each corresponding (purple or pink-colored) point in Fig. 2.4. Notably, most best-fit $w(z)$ curves intersect around the effective redshift $z_{\text{eff}} = 0.28$, the value that is indicated with a vertical black dashed line.

It is instructive to look at the overall extent of the distribution of models in the top panels of Fig. 2.4. The coverage of the $w_0 - w_a$ ”island” is highly non-uniform, with more models with a positive w_a than negative. In the top left panel, we obtain additional information by plotting the γ_3 parameter from Eq. 2.3 for each model, which dominates how far that Horndeski data vector's departure from our background ΛCDM cosmology is. As expected, lower values of γ_3 (i.e. models that resemble the ΛCDM background most) forms the core of the distribution, while models with higher values of γ_3 have larger deviations in (w_0, w_a) and tend to either aggregate in the branch favoring a higher value of w_0 and w_a around zero, or at the upper left tip which favors the lowest values of w_0 but the highest ones of w_a.

In the top right panel, we also color the points in the $w_0 - w_a$ plane with their associated values of χ^2 that quantify the difference between the input Horndeski data vector and the data vector corresponding to the best-fit $w_0 w_a$CDM model. The core of the distribution in $w_0 - w_a$ is made up of models with a low value of χ^2; these are the models that can be fit well with a $w_0 w_a$CDM cosmology. As in the left panel, models aggregating in the branch on the right, or at the tip on the upper left, are fit less well with a $w_0 w_a$CDM cosmology.

The top panels of Fig. 2.4 also show a branching in the distribution of models in the $w_0 - w_a$ plane, though weaker than the more prominent ones in the full 8D parameter space seen in Fig. 2.3. We did not pursue understanding this feature, given hat it is not extended, and probably encodes subtle correlations between dark energy parameters (w_0, w_a) and Horndeski model parameters when the former are enforced to fit the latter.

Finally, we ask what implications are on two of the most readily measured parameters by lensing surveys — Ω_M and $S_8 \equiv \sigma_8(\Omega_M/0.3)^{0.5}$. Note that the values of these two parameters measured in lensing surveys and the CMB are typically interpreted within the context of the flat ΛCDM cosmological model. Therefore, to infer σ_8 from our set of simulated Horndeski data vectors, we now enforce a fit of modified gravity with a ΛCDM cosmology rather than $w_0 w_a$CDM. We thus fix $w_0 = -1$ and $w_a = 0$, and vary the six other parameters listed in Eq. (2.7) to find the best-fit ΛCDM model. Then, we use `CAMB` to calculate the value of σ_8 and the corresponding S_8 for each best-fit ΛCDM model.

We plot ΛCDM's best-fit (Ω_M, S_8) pair for each Horndeski model in Fig. 2.5. Each point is colored by the γ_3 parameter (as defined in Eq. 2.3) for each Horndeski model we fitted to. As before, the cross-hairs denote the fiducial, input values of these parameters. In this case, we do not observe

Table 2.3: Summary of the trends in the inferred cosmological parameters when modified-gravity (Horndeski) models are interpreted within the context of unmodified gravity — either in w_0w_aCDM or ΛCDM cosmology. For each parameter, we show the percentage of best-fit values larger/smaller than the true (input) value. Parameters whose best-fit values are overwhelmingly shifted in the same direction are highlighted in red.

	w_0w_aCDM		ΛCDM	
Compared to fiducial value	% Larger	% Smaller	% Larger	% Smaller
$\Omega_b h^2$	99.7	0.3	99.9	0.1
$\Omega_c h^2$	2.8	97.2	1.1	98.9
A_s	62.3	37.7	35.2	64.8
H_0	78.6	21.4	99.2	0.8
n_s	99.2	0.8	99.97	0.03
τ	67.5	32.5	41.2	58.8
w_0	73.0	27.0	N/A	N/A
w_a	78.7	21.3		
Ω_m	N/A	N/A	0.9	99.1
S_8			0.7	99.3
$A_s e^{-2\tau}$	6.1	93.9	12.2	87.8

a particularly narrow region, or multiple branches, in the best-fit $\Omega_M - S_8$ plane. Rather, we see a near-universal shift to lower values of the best-fit Ω_M, and also a preferential shift toward lower S_8. As the Horndeski model deviates more from general relativity when γ_3 is larger, we observe a shift in Ω_m towards lower values. It is known that Horndeski models can generally accommodate *both* a larger and a smaller amplitude of structure formation relative to the standard model with the same background parameters. However, we need to remember that the CMB measurements at large scales, which fit the Integrated Sachs-Wolfe plateau, lie below the ΛCDM prediction. With the newfound parametric freedom in Horndeski models, it appears that the spectral index n_s increases to lower the large-scale power, and in turn lowers Ω_m and σ_8 (with which n_s is negatively correlated) to preserve the good fit at intermediate and smaller scales. This explains why we find the preferentially low Ω_m and σ_8 values in Horndeski models.

We also investigated the biases that one would observe on all six base cosmological parameters when interpreting modified gravity with a ΛCDM cosmology. The results are displayed in Fig. 2.6, which contains all possible 2D planes and histograms of cosmological parameters. The grey crosshair again indicates the unbiased, fiducial value of a parameter. In every panel, each point represents a parameter's relative shift or bias resulting from misinterpreting one of the 16769 modified gravity models with dark energy. Here, we observe a shift towards a uniform direction

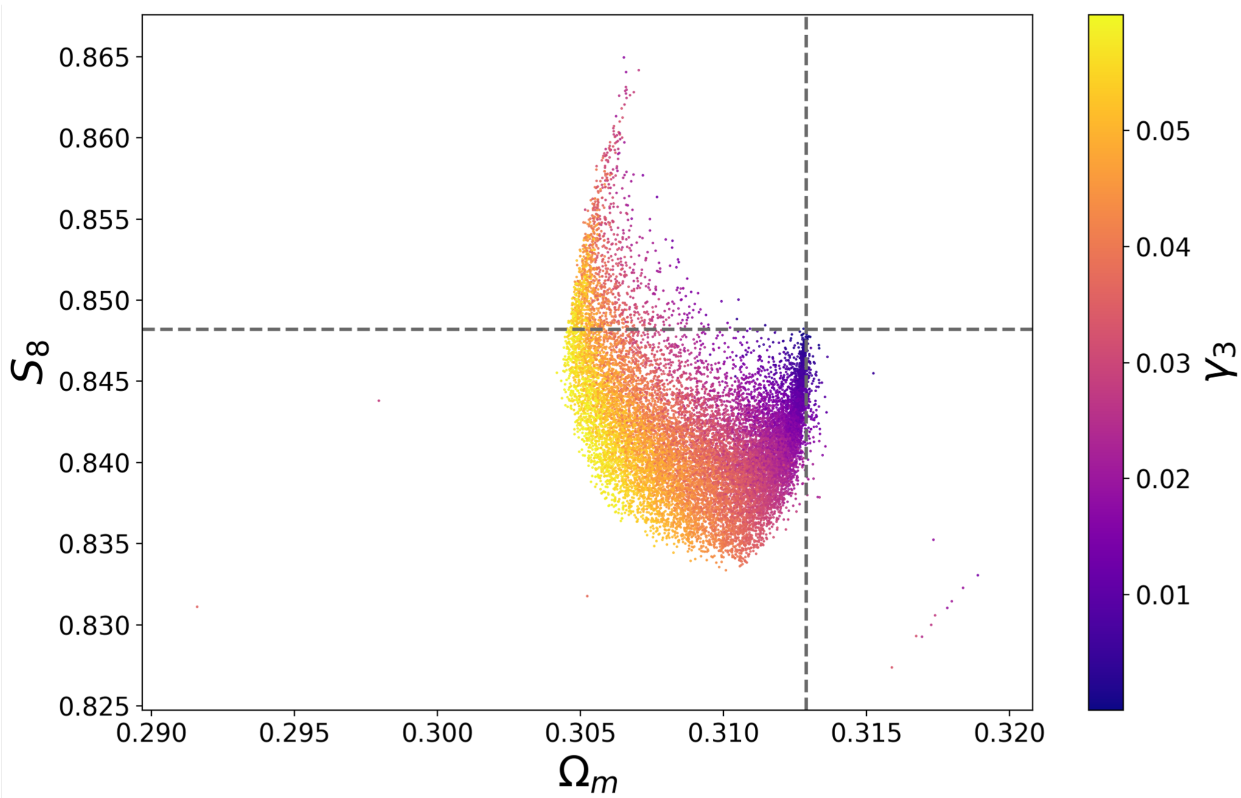

Figure 2.5: Best-fit values and projected 1D histograms of Ω_m and S_8 derived from fitting 16769 Horndeski data vectors with a ΛCDM cosmological model. Each point is colored by the γ_3 parameter for each Horndeski model as defined in Eq. 2.3.

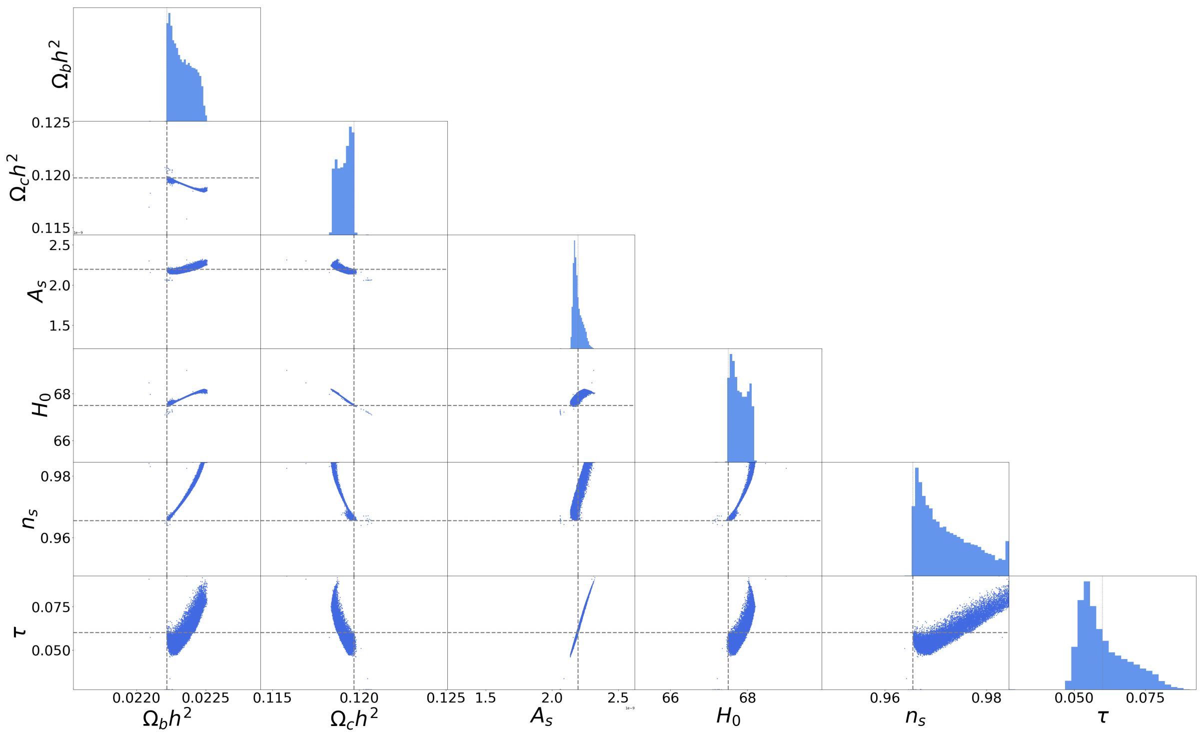

Figure 2.6: Best-fit values and histograms of cosmological parameters obtained from fitting to 16769 Horndeski models with a ΛCDM cosmology.

among four of the six parameters, $\Omega_b h^2$, $\Omega_c h^2$, H_0 and n_s, which are listed in Table 2.3. The degenerate combination of $A_s e^{-2\tau}$ also mostly shifts towards a value smaller than the fiducial one.

2.5 Conclusion

In this work we address the question of how analyses that fit standard cosmological models (say ΛCDM or $w_0 w_a$CDM) to data may show hints of modified gravity. Assume for the moment that modified gravity is at work. In a realistic situation, it is entirely plausible that a standard, unmodified-gravity model is a good fit to the data, so that we cannot immediately rule it out and claim evidence for modified gravity. This scenario, however, will generally lead to shifts in the (standard-model, unmodified-gravity) parameter values relative to their true values. And such shifts, interpreted together and in relation to other measurements in cosmology that depend on different kinds of data, may reveal the presence of modified gravity.

In this paper, we quantitatively investigate these parameter biases in scenarios when modified gravity is misinterpreted as a standard model. Specifically, we establish the link between modified-gravity models and shifts in the standard cosmological parameters. To scan through a broad range of modified-gravity model, we focus on the Horndeski universality class of models, whose phenomenological predictions (on linear scales) are produced by the code `EFTCAMB` [101]. Horndeski models allow a separate specification of the cosmological theory background and perturbations. For simplicity, we assume a cosmological-constant background for the Horndeski models (in agreement with the most recent cosmological data to date), and vary the perturbations, allowing the full freedom of Horndeski models. We fit these models with simulated future data consisting of CMB temperature and the polarization power spectra, BAO data, and type Ia supernova data. We restrict the analysis to only those Horndeski models whose simulated data vectors are well fit by the $w_0 w_a$CDM model. In doing this we mimic a realistic situation where one would only proceed with the interpretation of model fits in scenarios where the goodness of fit passes some threshold.

We report the best-fit values of the standard cosmological parameters for each Horndeski model that passes the aforementioned cuts. We find that the distribution of the best-fit values cover remarkably tight regions in the standard eight-dimensional parameter space (Fig. 2.3). These regions are largely linear, though on occasion carve out multi-pronged directions in the 2D parameter spaces. These tight correlations in standard parameter best-fits imply that even general classes of modified-gravity models register as specific deviations (from true values) in the unmodified-gravity parameters. This is good news; for example, a deviation in standard parameters that does *not* lie in one of these directions would indicate that systematic errors, rather than modified gravity, may be the cause of such unexpected shifts. Hence it should be possible to spot such signatures of systematic errors in future data.

Focusing now on the equation-of-state parameter values that are best fits to Horndeski models, we find that, even though significant deviations in both w_0 and w_a are allowed, they obey a tight mutual relation (Fig. 2.4). Specifically, most Horndeski models are fit with an effective equation of state of $w(z_{\rm eff}) \simeq -1$, evaluated at the effective redshift of $z_{\rm eff} = 0.28$. This can be taken as a very generic prediction of the perturbations provided by the large class of modified-gravity models that we study, given a ΛCDM background as stipulated above. This prediction, along with those on all other parameters specified in Fig. 2.3, will be sharply tested using upcoming cosmological data.

We finally study the implications of our result to the currently much debated tension between constraints on the S_8 parameter obtained from lensing probes and CMB measurements. Assuming now the ΛCDM model (in which the S_8 tension is usually framed), we find that Horndeski models typically predict a lower S_8, and near-universally a lower Ω_M, than the truth when the latter two are inferred assuming the ΛCDM model. Because the only direct probe of S_8 that we assumed was the CMB, this implies that CMB's S_8 value is preferentially low when Horndeski data are analyzed assuming the ΛCDM model. This should be compared to the prediction from applying the same pipeline to lensing data, something we plan to do in a future work.

CHAPTER 3

Evidence for suppression of structure growth in the concordance cosmological model

The temporal growth of cosmic structure is intimately connected with the property of dark energy and the theory of gravity. Works in the next two chapters involve using information on the growth of structure to test the concordance ΛCDM cosmological model and to probe the presence of modified-gravity theories.

We choose to focus on a parameter named the "growth index" which enters the parameterization of the linear growth rate through

$$f(z) = \Omega_M(z)^\gamma, \tag{3.1}$$

where $\Omega_M(z)$ is the energy density parameter of matter at a gived redshift, and the exponent γ is the growth index. Studying this parameter has two major advantages: 1) it only impacts the growth of cosmic structure but has no influence on geometric quantities such as distances, thus cleanly separating growth from geometry; 2) $\gamma = 0.55$ fits a wide range of cosmological models to sub-percent level, so any deviations in data analysis from this best-fit value will be of great interest.

In this chapter, we constrain the growth index by combining current cosmological data, including CMB data from Planck and the large-scale structure data from weak lensing, galaxy clustering, and cosmic velocities.

3.1 Introduction

The flat ΛCDM concordance cosmology, which combines general relativity (GR) and a spatially flat universe with ~70% constant dark energy and ~30% cold dark matter, provides an excellent fit to observational data. However, several tensions in measurements of parameters in this model have been noted in recent years [6]. Most significantly, the expansion rate H_0 inferred from the distance ladder [175] is higher than that measured by the cosmic microwave background (CMB)

[13]. At a lesser level of significance, the parameter $S_8 \equiv \sigma_8\sqrt{\Omega_m/0.3}$ (where σ_8 is the amplitude of mass fluctuations in spheres of $8\,h^{-1}$Mpc and Ω_m is matter density relative to the critical density) determined by CMB observations is larger than that found by galaxy clustering and weak gravitational lensing measurements [70]. Finally, the Planck CMB data by itself shows a preference for a nonzero spatial curvature Ω_K [13].

In this Letter, we consider the possibility that the growth of structure deviates from what predicted by the concordance model. While it is true that all the aforementioned parameters (Ω_m, S_8, and Ω_K) affect the growth of density perturbations, they also control geometrical quantities like distances and volumes, complicating the physical interpretation. It is thus important to isolate and constrain the growth of structure [105] separately from geometrical quantities. Here, we adopt a precise parameterization of the growth rate and find evidence for growth suppression — relative to the expectation from flat ΛCDM and GR — which also reconciles tensions in S_8 and Ω_K constraints. Our results clarify and consolidate the current situation in the field, where different analyses adopting different prescriptions of growth, or different implementations of how growth is separated from geometry, either found some evidence for a suppressed growth [178, 35, 113, 145, 29, 182, 86, 179, 213, 54, 5] or did not [209, 75, 104, 169, 168, 17, 180, 148, 23].

3.2 Growth of structure.

Over cosmic time, matter density fluctuations $\delta \equiv (\rho - \bar{\rho})/\bar{\rho}$ (where ρ and $\bar{\rho}$ are the local and the cosmic mean densities respectively) are amplified by gravity. Assuming GR and restricting to linear regime where $\delta \ll 1$ (roughly $k \lesssim 0.1\,h\,\mathrm{Mpc}^{-1}$ today with $h = H_0/100\,\mathrm{kms}^{-1}\mathrm{Mpc}^{-1}$) and subhorizon scales (roughly $k \gtrsim H_0 \simeq 0.0003\,h\,\mathrm{Mpc}^{-1}$ today), we can describe the growth of large-scale structure as [154, 36]

$$\ddot{\delta}(\boldsymbol{k}, t) + 2H\dot{\delta}(\boldsymbol{k}, t) - 4\pi G\bar{\rho}\delta(\boldsymbol{k}, t) = 0, \tag{3.2}$$

where dot denotes derivative with respect to time. Here the matter overdensity δ, the expansion rate H, and the mean matter density $\bar{\rho}$ all depend on time, while every Fourier $\boldsymbol{k}$-mode evolves independently. In this regime, it is useful to consider the (linear) growth function $D(t) \equiv \delta(t)/\delta(t_0)$, where t_0 is the present time, and the growth rate $f(a) \equiv d\ln D(a)/d\ln a$, where $a(t)$ is the scale factor. The growth rate is a central link between data and theory: it is directly proportional to large-scale structure observables like peculiar velocities and redshift-space distortions [153, 133], while being exquisitely sensitive to the properties of dark-energy models [58].

To further isolate the temporal evolution of structure, [84, 208, 136] introduced a robust and accurate approximation of the growth rate as

$$f(a) = \Omega_m^\gamma(a), \tag{3.3}$$

where γ is the *growth index*. In particular, [208, 136] showed that standard GR in the flat ΛCDM background predicts $\gamma \simeq 0.55$ even in the presence of dark energy; this fit is accurate to $\simeq 0.1\%$ [136, 139, 88]. A measured deviation from $\gamma = 0.55$ would suggest an inconsistency between the concordance cosmological model and observations. Assuming Eq. 3.3, the linear growth function takes the form

$$D(\gamma, a) = \exp\left[-\int_a^1 da\, \frac{\Omega_m^\gamma(a)}{a}\right], \tag{3.4}$$

where we have normalized $D(\gamma, a = 1) \equiv 1$ for all γ. A $\gamma > 0.55$ corresponds to a growth rate $f(\gamma, a) < f(0.55, a)$ and, because of the normalization, to a growth function $D(\gamma, a) > D(0.55, a)$ in the past.

3.3 Methodology and data.

To implement Eqs. 3.3–3.4, we express the linear matter power spectrum as

$$P(\gamma, k, a) = P_{\mathrm{today}}(k, a = 1)\, D^2(\gamma, a), \tag{3.5}$$

where P_{today} is the fiducial linear matter power spectrum evaluated today which depends on the usual set of cosmological parameters. To compute transfer functions and power spectra, we modify the cosmological Boltzmann solver `CAMB` [131, 98]. With $\gamma = 0.55$ we obtain (at redshift $z = 1.5$ and up to $k \lesssim 0.1\, h\,\mathrm{Mpc}^{-1}$) linear matter power spectra within 0.1% of the outputs from the unmodified version of `CAMB`. Likewise, we repeat the baseline Planck 2018 [13] and DES year-1 [3] analyses, using our modified `CAMB` [1] at fixed $\gamma = 0.55$, and reproduce their constraints on relevant cosmological parameters well within their precision.

Because the growth-index parameterization has only been validated for sub-horizon perturbations, care needs to be taken when modeling the CMB whose information partially comes from large scales and high redshifts. We choose to exempt the primary CMB anisotropies from the growth-index description. That is, we ensure Eq. 3.5 does not directly alter the *unlensed* CMB power spectra, but rather only affects the lensing effect, i.e. smoothing of the primary CMB acoustic peaks. Consequently, CMB data is sensitive to γ only through the CMB lensing gravitational potential [2], which is generated by density fluctuations within the regime where Eqs. 3.3–3.5 are

[1] Code available at this fork of `CAMB`: github.com/MinhMPA/CAMB_GammaPrime_Growth.

[2] Strictly speaking, the integrated Sachs-Wolfe effect, a secondary CMB anisotropy sourced by gravitational redshift,

valid.

Our baseline data includes measurements of the parameter combination $f\sigma_8$ from peculiar velocity and redshift-space distortion (RSD) data, at local ($z < 0.1$) [39, 108, 182, 46, 207] and cosmological distances ($z \geq 0.1$) [42, 43, 99, 151, 162, 16]. Figure 3.2 shows these $f\sigma_8$ measurements at the corresponding redshifts. We assume that the $f\sigma_8$ measurement uncertainties are Gaussian-distributed and uncorrelated among each other [3]. We further complement the $f\sigma_8$ measurements with either the Planck 2018 CMB data — including temperature, polarization and lensing reconstruction [13, 12] (hereafter PL18) — or large-scale structure data from galaxy surveys, or both. Data from galaxy surveys include a) the DESY1 3x2pt correlation functions [3] (hereafter DESY1), and b) baryon acoustic oscillations in the 6dF Galaxy Survey (6dFGS) galaxy [37] and the Sloan Digital Sky Survey (SDSS) [177, 15, 16] galaxy plus Lyman-alpha (hereafter BAO collectively). When including both SDSS $f\sigma_8$ and BAO data, we employ joint covariance and likelihood that properly account for their correlations [4]. Throughout, we adopt the same likelihoods and priors used in the baseline of those analyses. We fix the total mass of neutrinos to $\sum m_\nu = 0.06$ eV and include neutrino contribution Ω_ν in the matter density parameter Ω_m. We verify that excluding Ω_ν in computing theoretical $f\sigma_8$ leads to negligible changes in the latter and all downstream results. We allow γ to vary assuming a uniform prior $\mathcal{U}(0, 2.0)$.

We wish to constrain the growth index γ, along with other standard cosmological parameters: the matter and baryon densities relative to critical Ω_m and Ω_b, the Hubble constant H_0, spectral index n_s, mass fluctuation amplitude σ_8, and reionization optical depth τ. We therefore perform Bayesian inference via the Monte Carlo Markov Chain (MCMC) method using the `cobaya` framework [200] and analyze the MCMC samples using the `GetDist` package [130].

To quantify the statistical significance of our results, we compute the Bayesian factor of $\gamma = 0.55$ and $\gamma \neq 0.55$ by assuming the Savage-Dickey density ratio

$$\log_{10} \mathrm{BF}_{01} = \log_{10} \left. \frac{\mathcal{P}(\gamma|\mathrm{d}, \mathrm{M}_1)}{\mathcal{P}(\gamma|\mathrm{M}_1)} \right|_{\gamma=0.55}, \tag{3.6}$$

where d and M_1 respectively denote the data and the model with γ, while $\mathcal{P}(\gamma|\mathrm{M}_1) = \mathcal{U}(0., 2.)$. This is reported in the fifth column of Table 3.1. We further quote the significance of $\gamma \neq 0.55$ following the two-tailed test and measuring the posterior tail in units of Gaussian sigmas. To compare the goodness of fit between models, we first identify best-fit models that maximize their corresponding joint posteriors, then report the chi-square difference $\Delta\chi^2$ between two such models in the last column of Table 3.1 and in Table 3.2.

is also sensitive to γ.

[3]Likelihood and data available at this fork of `cobaya`: github.com/MinhMPA/cobaya

[4]cobaya.readthedocs.io/en/latest/likelihood_bao.html

3.4 Constraints on γ in a flat universe.

We first consider the data combination $f\sigma_8$+PL18. Marginalizing over all other cosmological parameters, we obtain the posterior density of γ shown in orange in Figure 3.1. This corresponds to the constraint $\gamma = 0.639^{+0.024}_{-0.025}$ and a Bayes factor of $|\log_{10}\mathrm{BF}_{01}| = 1.7$. The former excludes $\gamma = 0.55$ at a statistical significance of 4.2σ, while the latter provides a "very strong" evidence for deviation from the GR+flat ΛCDM prediction of $\gamma = 0.55$ according to the Jeffreys' scale [112]. Note that neither PL18 nor $f\sigma_8$ alone substantially constrains the growth index due to degeneracies with other cosmological parameters, yet together they show a clear preference for $\gamma > 0.55$, that is, a lower rate of growth than predicted by GR in flat ΛCDM. Figure 3.2 illustrates the effect of growth suppression as a function of redshift by showing the $f\sigma_8(z)$ posterior assuming flat ΛCDM, and that assuming flat ΛCDM+γ, both inferred from the $f\sigma_8$+PL18 data combination.

We next wish to investigate how the large-scale structure clustering and lensing data constrain γ. To do so, we replace the PL18 data by the DESY1 3x2pt measurements of galaxy clustering and weak lensing, together with the expansion-history data from BAO. The $f\sigma_8$+DESY1+BAO data combination yields the marginalized constraint $\gamma = 0.598^{+0.031}_{-0.031}$. Much like the $f\sigma_8$ + PL18 constraint, this combination prefers a higher growth index than the GR value, except now at a lower statistical significance, excluding $\gamma = 0.55$ at 2.0σ.

We finally report the constraint from all data combined, $f\sigma_8$+PL18+DESY1+BAO:

$$\gamma = 0.633^{+0.025}_{-0.024}. \tag{3.7}$$

Analysis of the posterior tails indicates that $\gamma = 0.55$ is excluded at 3.7σ, while the Bayes factor $|\log_{10}\mathrm{BF}| = 1.2$ shows a "strong" evidence for a departure from the expected value of γ. We show the posterior density of γ for combined data in violet in Figure 3.1; it is very close to the posterior for $f\sigma_8$+PL18.

We summarize all marginalized constraints on γ, together with their statistical significance, in Table 3.1.

3.5 Implications for S_8 tension.

A moderate yet persistent tension in constraints of S_8 has emerged between CMB measurements, e.g. Planck [13] or Atacama Cosmology Telescope plus Wilkinson Microwave Anisotropy Probe [14], and low-redshift 3x2pt measurements of weak lensing and galaxy clustering, e.g. the Dark Energy Survey (DES) [3], the Kilo-Degree Survey (KiDS) [94], and combinations thereof [22]. This discrepancy is statistically significant and unlikely to be explained by lensing systematics alone

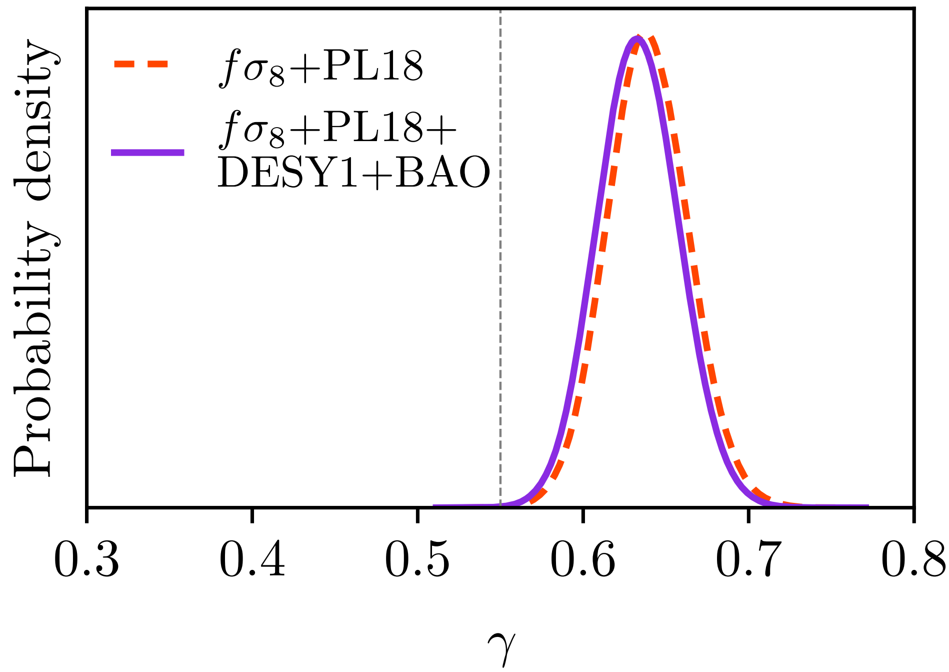

Figure 3.1: Marginalized constraints on the growth index γ, from $f\sigma_8$ data combined with PL18 (orange) and PL18+DESY1+BAO (violet). The vertical dashed line marks the concordance model prediction of $\gamma = 0.55$.

[127], thus motivates investigations of physics beyond the standard model.

Figure 3.3 shows the marginalized constraints in the 2D planes of the growth index γ and, from left to right, S_8 or Ω_m or H_0, by different data combinations. Notably, the $S_8 - \gamma$ panel indicates a potential solution to the S_8 tension: a higher growth index ($\gamma \simeq 0.65$) implies a *higher* S_8 value in the probes of large-scale structure. Specifically, the $f\sigma_8$+DESY1+BAO combination yields $S_8 = 0.784^{+0.017}_{-0.016}$, while in the standard ΛCDM (with $\gamma \equiv 0.55$) $S_8 = 0.771^{+0.014}_{-0.014}$. Conversely, Planck now prefers a *lower* amplitude of fluctuations ($S_8 = 0.807^{+0.019}_{-0.019}$) than it does in ΛCDM ($S_8 = 0.831^{+0.013}_{-0.012}$). Consequently, the "$S_8$ tension" between the measurements of S_8 in the galaxy clustering and gravitational lensing versus that in Planck decreases from 3.2σ to 0.9σ, as measured by the S_8 difference divided by errors added in quadrature.

3.6 Allowing curvature to vary.

Relaxing the assumption of spatial flatness changes the expansion history and the concordance prediction for the growth history [146, 89]. An immediate question is whether the apparent preference for a higher growth index and a slower growth rate is the same effect as the apparent

Table 3.1: Constraints on the growth index γ and cosmological parameters S_8 and H_0 from different data combinations, the corresponding Bayes factors, and chi-square differences relative to the concordance model ($\gamma = 0.55$).

Data	γ	S_8	H_0 [$\mathrm{kms^{-1}Mpc^{-1}}$]	$\lvert \log_{10} \mathrm{BF}_{10} \rvert$	$\Delta\chi^2 \equiv \chi^2_\gamma - \chi^2_{\gamma=0.55}$
PL18	$\mathbf{0.668^{+0.068}_{-0.067}}$	$0.807^{+0.019}_{-0.019}$	$68.1^{+0.7}_{-0.7}$	0.4	−2.8
PL18+$f\sigma_8$	$\mathbf{0.639^{+0.024}_{-0.025}}$	$0.814^{+0.011}_{-0.011}$	$67.9^{+0.5}_{-0.5}$	1.7	−13.6
PL18+$f\sigma_8$ +DESY1+BAO	$\mathbf{0.633^{+0.025}_{-0.024}}$	$0.802^{+0.008}_{-0.008}$	$68.4^{+0.4}_{-0.4}$	1.2	−13.2
PL18+$f\sigma_8$ +DESY1+BAO (flat ΛCDM+GR)	**0.55**	$0.803^{+0.008}_{-0.008}$	$68.5^{+0.4}_{-0.4}$	-	0

Table 3.2: Chi-square differences between best-fit models with free γ and best-fit concordance models, for different data combinations and individual likelihoods.

Data	$\Delta\chi^2 \equiv \chi^2_\gamma - \chi^2_{\gamma=0.55}$							
	low-ℓ TT	**low-ℓ EE**	**high-ℓ TTTEEE**	**lensing**	$f\sigma_8$	**DESY1**	**BAO**	**total**
PL18 temp.+pol.	−1.1	−0.4	−7.0	-	-	-	-	−8.5
PL18	−1.0	−0.1	−3.1	+1.4	-	-	-	−2.8
PL18+$f\sigma_8$	+0.1	−0.3	−5.6	+0.5	−8.3	-	-	−13.6
PL18+ DESY1+BAO	−0.6	−0.8	−3.7	+0.3	-	−0.7	+0.8	−4.7
$f\sigma_8$+DESY1 +BAO	-	-	-	-	−1.2	−2.9	−2.2	−6.3
PL18+$f\sigma_8$ +DESY1+BAO	−0.2	−1.1	−5.3	−0.7	−6.8	+0.8	+0.1	−13.2

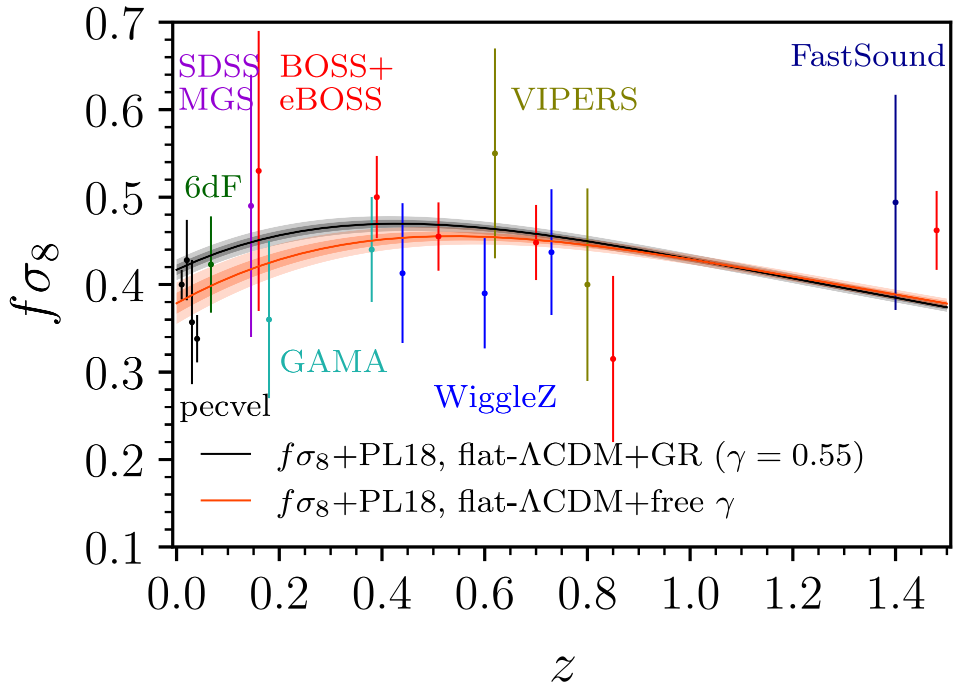

Figure 3.2: Marginalized posterior on the theoretical $f\sigma_8(z)$ assuming the growth-index parameterization in Eq. 3.3. Shaded bands show the 68% and 95% posteriors from our baseline analysis that includes $f\sigma_8$ and PL18 data (orange), and the corresponding constraints in the concordance model with $\gamma = 0.55$ (black). The data points indicate actual $f\sigma_8$ measurements.

preference for a nonzero curvature found by the Planck 2018 analysis that, by using temperature and polarization data, found $\Omega_K = -0.044^{+0.018}_{-0.015}$ ([13]; see also [72, 92, 71]).

Allowing both curvature and growth index to vary, we observe a trade-off between Ω_K and γ, as shown in Figure 3.4 using *only* Planck CMB temperature and polarization data (henceforth PL18 temp.+pol.). The data clearly prefer either a positively curved space, i.e. $\Omega_K < 0$, or growth suppressed relative to the GR prediction, i.e. $\gamma > 0.55$; the flat model with $\gamma = 0.55$ has a worse fit than the best-fit model by $\Delta\chi^2 = -6.9$.

We next focus on two limits of the results shown in Figure 3.4: a) varying Ω_K while fixing $\gamma = 0.55$ (which reproduces the standard analysis from the Planck paper, also finding $\Omega_K = -0.044$), and b) fixing $\Omega_K = 0$ while varying γ. We are particularly interested in comparing the fit of these two models. We find that the model with free curvature fits the PL18 temp.+pol. data marginally better than the model with free γ ($\Delta\chi^2 = -1.3$). Including PL18 CMB lensing reconstruction likelihood leads to $\Delta\chi^2 = 0.7$ in favor of the free-γ model. Overall, we conclude that both models fit the PL18 data equally well.

Recall that the feature in the PL18 temp.+pol. data driving the preference for $\Omega_K < 0$ is

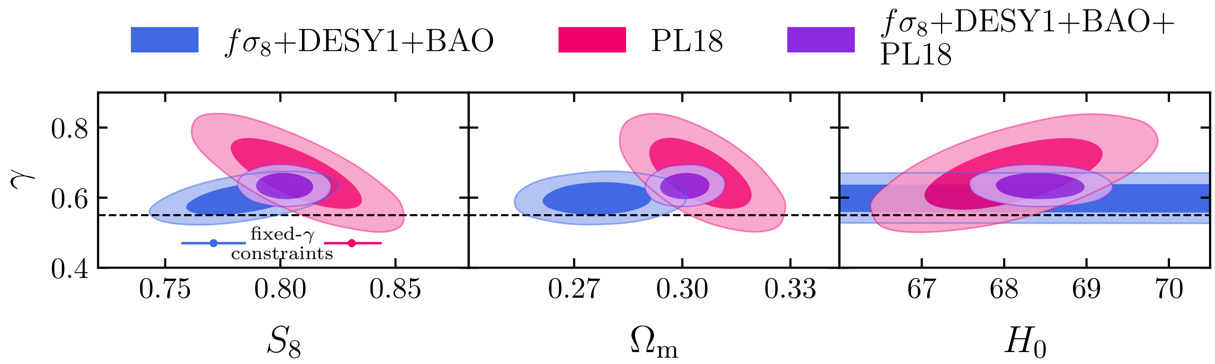

Figure 3.3: 68% and 95% marginalized constraints on parameters in the concordance model allowing for a free growth index γ, from $f\sigma_8$+DESY1+BAO (blue), PL18 alone (red) and $f\sigma_8$+DESY1+BAO+PL18 (violet). Contours contain 68% and 95% of the corresponding projected 2D constraints. The horizontal black dashed lines mark the concordance model prediction of $\gamma = 0.55$. The horizontal bars in the $\gamma - S_8$ panel indicate the 68% limits on S_8 for a fixed $\gamma = 0.55$ (see text); they are vertically offset from $\gamma = 0.55$ for visibility.

essentially the same one that favors a high CMB lensing amplitude, i.e. $A_{\rm lens} > 1$ [8, 13, 12]. Does the cosmological model with a high γ produce similar features in the CMB power spectra as those with $\Omega_K < 0$ or $A_{\rm lens} > 1$? The answer is affirmative, as shown in Figure 3.5 where we compare the residuals in the CMB temperature angular power spectrum (TT) of a) the PL18 data, b) the best-fit flat model with γ, c) the best-fit model with curvature but fixed $\gamma = 0.55$, and d) the best-fit flat model with $A_{\rm lens}$ but fixed $\gamma = 0.55$, all relative to that of the best-fit concordance model. All three best-fit model residuals display the same oscillatory pattern that closely follows the oscillations in the data residuals. The similarity of the effects of $\gamma > 0.55$ and $A_{\rm lens} > 1$ in the CMB temperature and polarization power spectrum is not entirely surprising: a higher γ encodes a lower growth rate $f(a)$ and, for a fixed amount of structure observed today, a larger amount in the recent past (see Eq. 3.4 and the discussion that follows). This in turn implies a higher lensing signal in the CMB, and thus has a qualitatively similar effect as $A_{\rm lens} > 1$ [5].

3.7 Summary and Discussion.

In this Letter, we have presented new constraints on the growth rate using a combination of Planck, DES, BAO, redshift-space distortion and peculiar velocity measurements. The constraints from different data combinations are consistent with one another within 1σ. Our constraints exclude

[5]The preference for anomalous growth index in PL18 temp.+pol. data ($\Delta\chi^2 = -8.5$ in favor of the free-γ model over the concordance one) decreases once the CMB lensing reconstruction likelihood is included ($\Delta\chi^2 = -2.8$). A similar effect is observed for the case of varying $A_{\rm lens}$.

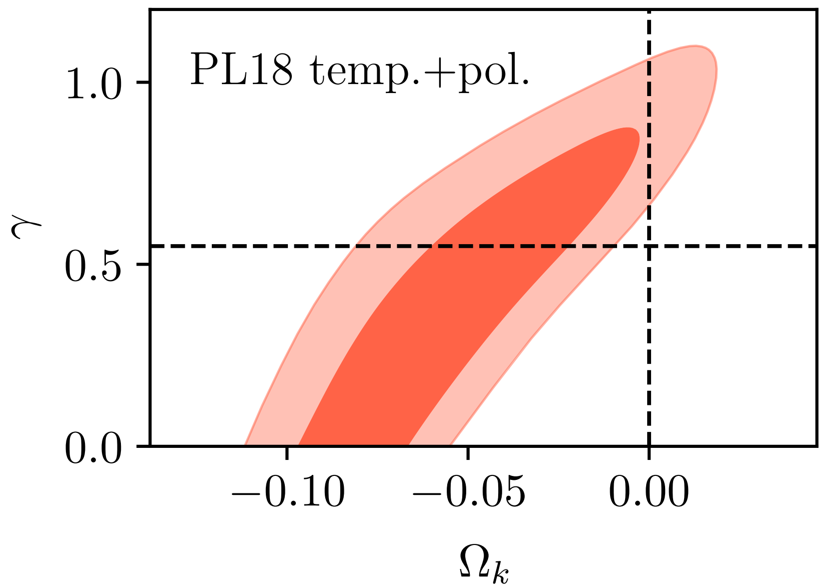

Figure 3.4: Degeneracy between γ and Ω_K in the PL18 temp.+pol. analysis when both parameters are allowed to vary. Contours show the 68% and 95% credible intervals. The dashed lines mark the point [$\Omega_K = 0, \gamma = 0.55$] corresponding to the concordance flat ΛCDM model.

the predictions of flat ΛCDM model in GR at the statistical significance of 3.7σ, indicating a suppression of growth rate during the dark-energy dominated epoch.

Further, we have explicitly demonstrated that cosmological models with a high γ resolve two known tensions in cosmology. First, allowing for a suppressed growth removes the need for negative curvature indicated by the PL18 temp.+pol. data; in fact, the best-fit flat model with free γ fits the data equally well as the best-fit model with standard growth and negative curvature, producing highly similar features in the temperature angular power spectrum. Second, the discrepancy in the measured amplitude of mass fluctuations parameter S_8 from the PL18 data and that from the large-scale structure data can be reconciled with a high-γ model. Our findings indicate that these cosmological tensions can be interpreted as evidence of growth suppression.

A late-time growth suppression is not straightforward to achieve in modified theories of gravity, particularly if the expansion history is similar to that in the concordance model [27, 117, 118] as our constraints indicate. Nevertheless, there is sufficient freedom in the space of modified-gravity theory (within a sub-class of Horndeski models, e.g. [164, 158, 157]) to do so. Probing such modified-gravity theories should be within the reach of future surveys and experiments [82, 156, 212]. Specifically, upcoming large-scale structure data [61, 87, 186, 199, 126, 188] will improve $f\sigma_8$ data both in terms of measurement precision and redshift coverage. In parallel, forthcoming CMB measurements [14, 9, 1, 18] with higher resolution and sensitivity will also play a significant role

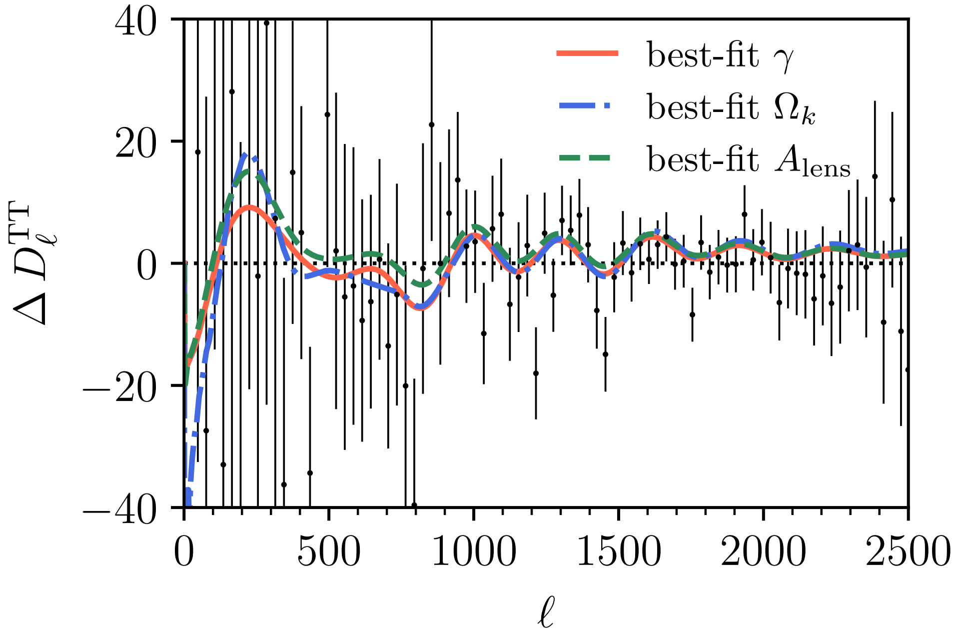

Figure 3.5: Residuals in the CMB TT angular power spectrum $D_\ell \equiv \ell(\ell+1)C_\ell/(2\pi)$ between the best-fit model with free γ (orange), best-fit model with curvature (blue), and best-fit model with free CMB lensing amplitude $A_{\rm lens}$ (green). The data points and error bars represent the Planck 2018 (binned) TT power spectrum residuals and the 68% uncertainties. All residuals are computed with respect to the best-fit concordance model.

in pinning down the expansion history and growth rate. As we enter the era of high-precision large-scale structure and CMB measurements, joint analyses of these data sets will hold the key to confirming any evidence for physics beyond the standard model.

CHAPTER 4

Sweeping Horndeski Canvas: New Growth-Rate Parameterization for Modified-Gravity Theories

This chapter continues to study the growth index γ, modeling its behavior in modified-gravity theories. While the popular constant growth index can parameterize linear growth rate $f(z)$ sufficiently well in models that assume GR, the growth index can be generalized to incorporate time variations into $\gamma(z)$. We investigate in this work whether a redshift-dependent parameterization of the growth index can model linear growth better in modified-gravity theories. If so, what is the functional form of this better fitting formula and by how much has it improved the goodness-of-fit?

4.1 Introduction

Over ∼13.7 billions years of cosmic evolution, the tiny primordial fluctuations seeded during inflation — under gravitational interaction — evolve into the large-scale structure observed and measured by galaxy surveys today. The temporal growth of cosmic structure has a rich and well-understood behavior in different epochs: it is robust in the matter-dominated era, but suppressed at late times, especially following the onset of dark energy. The clustering of galaxies, the weak gravitational lensing of distant background galaxies, and arguably the abundance of galaxy clusters as a function of their redshifts and mass proxies have all established themselves as powerful probes of structure growth. These measurements then translate into constraints on models of dark matter and dark energy or modified gravity (see, e.g. [96] for a recent, general review).

In the linear regime (corresponding to scales $k \lesssim 0.1h\,\mathrm{Mpc}^{-1}$ today), the growth of density fluctuations is described by the linear growth function $D(a) \equiv \delta(a)/\delta(a=1)$. From it, we can define the *growth rate* as

$$f(a) \equiv \frac{d\ln D}{d\ln a}, \tag{4.1}$$

where a is the cosmic scale factor. For the standard, smooth dark-energy with an equation of state

w, on sub-horizon-scales and in the absence of massive neutrinos, D and f are scale-independent[1]. The growth rate can be formally obtained by solving the second-order differential equation which, in standard gravity and on sub-horizon scales, reads $\ddot{D} + 2H\dot{D} = 4\pi G\rho_M D$. Here ρ_M is the background matter density, G is the Newton constant, and dots are derivatives with respect to time.

In a wide class of cosmological models, the growth rate is well-approximated by a fitting function[2]

$$f(z) = \Omega_M(z)^{\gamma(z)}. \tag{4.2}$$

Here, $\Omega_M(z)$ is the time-dependent matter density relative to critical, and the free function $\gamma(z)$ is the so-called *growth index*. The latter has a long history in cosmology, dating back to [154, 84, 133, 208], as it describes the growth rate in standard matter-dominated cosmologies. [136] proposed and verified that the growth-index parameterization $\gamma = 0.55 + 0.02(1 + w(z = 1))$ fits the true growth for all wCDM models to better than 0.2%, all the way from the matter-dominated era to the present time, for a wide range of Ω_M value. Moreover, this parameterization also provides a good fit to the growth in isolated modified-gravity models with, e.g. $\gamma \simeq 0.67$ for the DGP models [139, 88].

A fitting formula for the growth rate such as Eq. 4.2 is useful for at least two reasons. First, it is easy to implement in cosmological analyses. Second, it is straightforward to test whether the growth *alone* agrees with the prediction of a cosmological model (say $\gamma \simeq 0.55$ for ΛCDM [149] (see also, e.g. [17, 113]). Therefore, there has been considerable interest in developing phenomenological formulae for the growth rate and, in particular, investigating their robustness with respect to the choice of the cosmological model. Analytic works, e.g. [139, 129, 140, 50], have examined the best-fit $\gamma(z) = \gamma_0$ — the redshift-independent values of γ that minimized deviations of Eq. 4.2 from the exact growths defined in Eq. 4.1 — in various modified gravity and dark energy models. Further, [167, 85, 214, 34, 28, 29, 122, 142, 123, 192] focused on the redshift evolution of the growth index in $f(R)$ gravity, $f(Q)$ gravity, and interacting dark energy models; the most common among which are the linear parameterization $\gamma(z) = \gamma_0 + \gamma_1 z$ and the Taylor expansion $\gamma(z) = \gamma_0 + \gamma_1\, z/(1+z)$ which are both motivated by the parametrization $w(a) = w_0 + w_a(1-a)$ for the time-dependent equation of state of dark energy $w(a)$ [59, 135].

Our principal goal in this paper is to explore the accuracy of different $\gamma(z)$ parameterizations within the viable space of Horndeski theory, in the context of future constraints on $f(z)\sigma_8(z) \equiv f\sigma_8(z)$ by Stage-IV and Stage-V large-scale structure surveys. These upcoming surveys will yield $f\sigma_8(z)$ measurements with stringent error bars and extend to high redshifts. To that effect, we adopt exact numerical calculations of Eq. 4.1 as the baseline, and then fit the growth rate $f\sigma_8(z)$ in

[1]See the discussion in the Appendix B.2 for more details on the scale-independence in the context of Horndeski models considered in this work.

[2]Throughout, we characterize the time evolution interchangebly by the scale factor a or the redshift $z = 1/a - 1$.

$\sim$18,000 Horndeski models using a broad set of functional forms. We then compare their goodness of fit to the ground truth in Horndeski models in the context of errors predicted for future surveys, and propose the best new parameterization of $\gamma(z)$. We further demonstrate the utility of the proposed parameterization by constraining its parameters using current observational data of type Ia supernovae, large-scale structure, and the cosmic microwave background (CMB), and briefly comment on the implications for stress-testing the standard cosmological model.

The rest of this paper is structured as follows. Section 4.2 reviews the effective field theory framework we exploit to evaluate the growth rate $f\sigma_8(z)$ in a given Horndeski model. Section 4.3 details our procedure to sample Horndeski models and to obtain each model's theoretical prediction on $f\sigma_8(z)$. Section 4.4 discusses various parameterizations of $\gamma(z)$ focusing on their performance in fitting the theory models, and presents current constraints on parameters of the best fitting formula. Finally, Section 4.5 summarizes our analysis.

4.2 Horndeski models: theory background and growth of structure

We wish to consider the most general class of ΛCDM extensions for the accelerating universe that are *not* strongly disfavored by current data. We therefore must find an effective way to sample the model space. To this end, we adopt the Effective Field Theory (EFT) formalism for dark energy and modified gravity (henceforth EFTDE) [90, 45]. Within EFTDE, models with similar properties are established through a grouping of terms in the fundamental Lagrangian such that one can consider a class of models together (for more details, see [83] and references therein).

4.2.1 Effective Field Theory approach to Dark Energy

In general, the EFTDE action in unitary gauge can be written as, e.g. [100, 171]

$$
\begin{aligned}
S = \int d^4x\sqrt{-g}\Bigg[&\frac{1}{2}m_0^2[1+\Omega(t)]R - \Lambda(t) - c(t)g^{00} + \frac{M_2^4(t)}{2}(\delta g^{00})^2 \\
&- \frac{\bar{M}_1^3(t)}{2}\delta K\delta g^{00} - \frac{\bar{M}_2^2(t)}{2}\delta K^2 - \frac{\bar{M}_3^2(t)}{2}\delta K_\nu{}^\mu\delta K_\mu{}^\nu \\
&+ \frac{\hat{M}^2(t)}{2}\delta R^{(3)}\delta g^{00} + m_2(t)\partial_i g^{00}\partial^i g^{00} + \mathcal{L}_m\Bigg],
\end{aligned}
\tag{4.3}
$$

where $\delta g^{00} = g^{00}+1$ is the perturbation to the time component of the metric, $R^{(3)}$ is the perturbation to the spatial component, and $\delta K_{\mu\nu}$ is the perturbation of the extrinsic curvature. The background evolution depends on three EFTDE functions, $c(t)$, $\Lambda(t)$, and $\Omega(t)$. For any given expansion history, the first two functions, $c(t)$ and $\Lambda(t)$ can be constrained by the Friedmann equations and correspond to energy density and pressure. The effect of modified gravity is parameterized by the third function $\Omega(t)$. The other EFTDE functions in Eq. 4.3 represent perturbations around the background and correspond to observables that can be compared with observations. Table 1 in [141] gives a summary of all models that can be represented by the EFT formalism.

Within EFTDE, we focus on the Horndeski class of models (see, e.g. [124] for an in-depth review). The class of Horndeski theories is the most general scalar-tensor extension of general relativity, including but not limited to quintessence (see [203] for a review) and generalized Brans-Dicke (Jordan Brans-Dicke [48], f(R) [102], chameleons [121]) models. Moreover, within these scalar-tensor theories, a coupling between the derivative of a scalar field and the Einstein tensor (or the Ricci tensor alone) leads to an accelerated expansion of the cosmic background without demanding for a scalar potential [19, 67].

The Horndeski class is specified by imposing additional constraints on the EFTDE functions that describe perturbations around the background, as follows:

$$2\hat{M}^2 = \bar{M}_2^2 = -\bar{M}_3^2,\ m_2 = 0. \tag{4.4}$$

To evaluate the growth rate in a given Horndeski model and cosmology, we employ the `EFTCAMB` framework[3] [100, 101, 171]. `EFTCAMB` characterizes a given Horndeski model by seven functions which we parameterize as follows. One aforementioned function, $\Omega(t)$, controls the background evolution. We henceforth relabel it Ω^{MG}, for it not to be confused with an energy density parameter.

Inspired by $f(R)$ gravity and (again) following the convention in [100, 101, 171], we further assume $\Omega^{\mathrm{MG}}(t)$ evolves in time as

$$\Omega^{\mathrm{MG}}(a) = \Omega^{\mathrm{MG},0} a^{s_0}. \tag{4.5}$$

For ΛCDM, $\Omega^{\mathrm{MG}}(a) = 0$. Further, there are six dimensionless, second-order EFTDE functions $\{\gamma_1^{\mathrm{MG}}, \ldots, \gamma_6^{\mathrm{MG}}\}$ that jointly define the perturbative properties of the model. These functions are related to the perturbation functions in the EFTDE action in Eq. 4.3 through

$$\begin{aligned}
\gamma_1^{\mathrm{MG}}(t) &= \frac{M_2^4(t)}{m_0^2 H_0^2}, & \gamma_2^{\mathrm{MG}}(t) &= \frac{\bar{M}_1^3(t)}{m_0^2 H_0}, & \gamma_3^{\mathrm{MG}}(t) &= \frac{\bar{M}_2^2(t)}{m_0^2}, \\
\gamma_4^{\mathrm{MG}}(t) &= \frac{\bar{M}_3^2(t)}{m_0^2}, & \gamma_5^{\mathrm{MG}}(t) &= \frac{\hat{M}^2(t)}{m_0^2}, & \gamma_6^{\mathrm{MG}}(t) &= \frac{m_2^2(t)}{m_0^2}.
\end{aligned} \tag{4.6}$$

We assume that the time evolution of these quantities follows a similar functional form to that of

[3] github.com/EFTCAMB/EFTCAMB

$\Omega^{\rm MG}(t)$ in Eq. 4.5 above, that is

$$\gamma_i^{\rm MG}(a) = \gamma_i^{\rm MG,0} a^{s_i}. \tag{4.7}$$

Note that Eq. 4.5 and Eq. 4.7 implicitly limit the Horndeski theory space accessible in our analysis.

The constraint in Eq. 4.4 corresponds to $2\gamma_5^{\rm MG} = \gamma_3^{\rm MG} = -\gamma_4^{\rm MG}$ and $\gamma_6^{\rm MG} = 0$. Therefore, the Horndeski models are fully specified with six EFTDE parameters that control perturbations, $\gamma_{1,2,3}^{\rm MG,0}$ and $s_{1,2,3}$, plus two EFTDE parameters that control the background, $\Omega^{\rm MG,0}$ and s_0.

The full theoretical model requires the specification of other standard cosmological parameters that control the expansion rate $H(z)$ and the density perturbations. For the background expansion, we consider a flat ΛCDM cosmological model, specified by the physical baryon and cold-dark-matter densities ($\Omega_b h^2$ and $\Omega_c h^2$ respectively), and the constant dark-energy equation of state $w = -1$. Our full model parameter space is therefore

$$p_i \in \{\Omega_b h^2, \Omega_c h^2, H_0, \Omega^{\rm MG,0}, \gamma_1^{\rm MG,0}, \gamma_2^{\rm MG,0}, \gamma_3^{\rm MG,0}, s^0, s^1, s^2, s^3\}. \tag{4.8}$$

Certain analyses, e.g. [125, 150, 82], fix $\gamma_3^{\rm MG}(a) = 0$ to enforce that the speed of the propagation of gravitational waves (GW) to be equal to the speed of light. This requirement is motivated by the constraints derived from the binary neutron-star merger events "observed" by both GW and optical instruments (see [79] for a review), e.g. GW170817 and GRB170817A [2]. To better understand this, consider a simple model-independent parameterization of the speed of propagation of GW [96]

$$c_T^2/c^2 = 1 + \alpha_T(a), \tag{4.9}$$

where c_T^2 and c^2 are the squared speeds of GW and of light, respectively. Here $\alpha_T(a)$ quantifies the GW speed excess, and can be mapped into the $\gamma_3^{\rm MG,0}$ function as

$$\alpha_T(a) = -\frac{\gamma_3^{\rm MG}(a)}{1 + \Omega^{\rm MG}(a) + \gamma_3^{\rm MG}(a)}. \tag{4.10}$$

From Eq. 4.10, it is clear that the GW constraint of $-3 \times 10^{-15} < c_T/c - 1 < 7 \times 10^{-16}$ [2, 79] translates into

$$-1.4 \times 10^{-15}[1 + \Omega^{\rm MG}(a)] < \gamma_3^{\rm MG}(a) < 6 \times 10^{-15}[1 + \Omega^{\rm MG}(a)], \tag{4.11}$$

which is often simply taken to be $\gamma_3^{\rm MG}(a) = 0$ within EFTDE (or $\alpha_T = 0$ in general).

In this paper, we do *not* follow the above approach but rather, for full generality, allow for $\gamma_3^{\rm MG,0} \neq 0$. This choice certainly merits a justification: [66] pointed out that current LIGO multi-messenger GW events have only been detected at the energy scale close to either the strong coupling scale or the EFT cut-off. They further explicitly showed that, within the EFTDE approach to Horndeski theories, the GW speed is generally a function of energy scale $c_T(k)$ (see their Eq. (13)), and therefore — while strongly bounded to the speed of light at LIGO scale — can still potentially deviate from that when measured at lower frequencies (see their Fig. 1). Those Horndeski models hence do not necessarily obey the derived constraint in Eq. 4.11. Future observations of either GW events at lower frequency, e.g. with LISA [25], or CMB B-mode polarization [18, 1] will be able to place stringent constraints on the speed of GWs in these Horndeski models. Finally, we note that [170] did not find a qualitative difference between reconstructed Horndeski models with zero and non-zero $\gamma_3^{\mathrm{MG}}(a)$ when confronting models with current cosmological data[4].

4.2.2 Stability conditions in EFTDE and `EFTCAMB`

`EFTCAMB` further allows user to impose a set of consistency checks on the EFT functions in order to ensure that the EFTDE models being considered and evaluated meet the theoretical stability conditions [100]. These so-called *viability conditions* [101], or rather *viability priors* in the context of cosmological inference [171], include

1. Physical stability: the EFTDE theory must have a background stable to perturbations. In other words, the background must be free from ghost and gradient instabilities. The former corresponds to the situation where the model has a negative kinetic energy; the latter refers to the scenario where the squared sound speed is negative in some background regions. [33] (see Eqs. (42)-(51) of [101] for details).

2. Mathematical stability: the EFTDE theory must have a well-defined π-field equation with no fast exponential growing modes of perturbations, as well as well-defined equations for tensor perturbations (see Eq. (52) of [101] for details).

3. Additional, model-specific stability: For Horndeski models, this enforces $w(a) \leq -1/3$ at all time. Specifically to this work, this condition is automatically guaranteed as we consider only the case of a constant $w = -1$.

Generally speaking, the set of physical stability conditions is more restrictive than the mathematical ones. Further, the mathematical stability conditions implicitly assume that a) the π-field equation decouple from other field equations and b) its time-dependent coefficients evolve slowly (with time); these conditions are approximate and model-dependent. Therefore, in this work we only impose the physical conditions. We have explicitly verified through on a number of pilot runs that running `EFTCAMB` with only physical conditions versus both physical and mathematical conditions does not

[4]Their data sets include CMB (Planck), weak lensing (CFHTLenS), BAO (6dFGS and SDSS) and type Ia supernovae (Pantheon).

qualitatively affect the range of Horndeski models successfully evaluated by `EFTCAMB`, hence the principal results of our work.

4.2.3 Growth prediction in Horndeski models

In order to draw connections between Horndeski models and observational data, we will focus on the prediction of each Horndeski model for the parameter combination $f(z)\sigma_8(z) \equiv f\sigma_8(z)$. This quantity plays a central role in describing galaxy peculiar velocities and redshift-space distortions; it is thus an excellent meeting place between observations and theories of modified gravity. For each theoretical model under consideration, we compute the exact $f\sigma_8(z)$ using `EFTCAMB` in bins of redshift. In this paper, we follow the convention in [8, 13] and define $f\sigma_8(z)$ through

$$f\sigma_8(z) \equiv \frac{\left[\sigma_8^{(vd)}(z)\right]^2}{\sigma_8^{(dd)}(z)}, \tag{4.12}$$

where $\sigma_8^{(vd)}$ is the amplitude of (total) matter fluctuations obtained from the matter velocity-density (cross-)correlation function, while $\sigma_8^{(dd)} \equiv \sigma_8$ is that same quantity obtained from the matter density-density (auto-)correlation function. Specifically,

$$\left[\sigma_8^{(xx)}(z)\right]^2 = \int \frac{dk}{k} W_{\mathrm{TH}}^2(k, R = 8h^{-1}\,\mathrm{Mpc}) T_x(k,z) T_x(k,z) P_{\mathcal{R}}(k), \tag{4.13}$$

where x denotes either the v or d component, $W_{\mathrm{TH}}^2(k, R = 8h^{-1}\,\mathrm{Mpc})$ is the Fourier transform of the spherical top-hat window function of radius $R = 8h^{-1}$ Mpc, $T_x(k)$ is the transfer function of the x component, and $P_{\mathcal{R}}(k)$ is the power spectrum of primordial adiabatic perturbations.

Dividing this $f\sigma_8(z)$ by the value of $\sigma_8(z)$ (also calculated by `EFTCAMB`), gives the theoretically predicted growth rate $f(z)$ of each Horndeski model, which will then be fit with the formula in Eq. 4.2 with a specified functional form of $\gamma(z)$. For all Horndeski models considered in this work, Eqs. 4.12–4.13 or Eq. 4.1 yields the same numerical result and quantitative conclusion within the scales of interest, $k \simeq 0.01 - 0.1\,h\,\mathrm{Mpc}^{-1}$. This conclusion naturally follows under the assumption that growth rate is scale-independent. Even though this assumption may not hold in more generic Horndeski and modified gravity models (see e.g. [193, 26]), it holds up rather well for Horndeski models we consider here, in particular within the scales probed by Stage IV and V surveys, i.e. $k \simeq 0.01 - 0.1\,h\,\mathrm{Mpc}^{-1}$. Within that range of k and each of the Horndeski models considered in this work, $f\sigma_8(z)$ only vary within sub-percent level at any given z. We further illustrate and discuss this point in Appendix B.2.

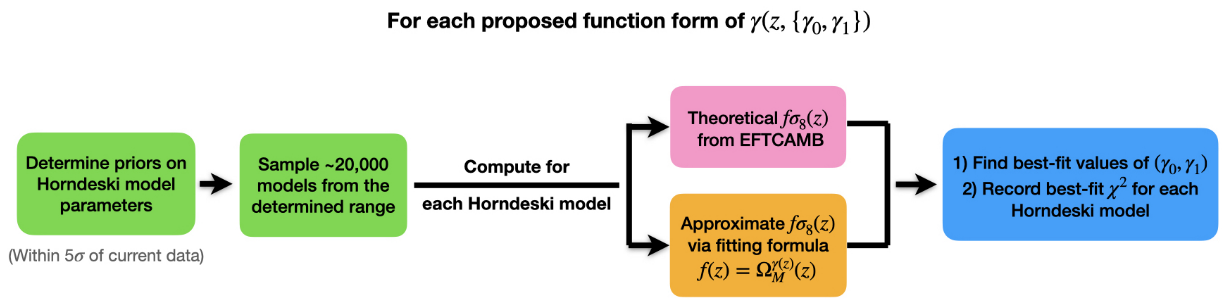

Figure 4.1: Flowchart describing how we sample Horndeski models from EFTDE theory space, evaluate the models and test the fitting functions for $\gamma(z)$ against their predictions for $f\sigma_8(z)$.

4.3 Testing growth parameterizations in Horndeski models

Our aim is to statistically chart a broad range of functional forms of $\gamma(z)$, but only for Horndeski models that are compatible with current observational constraints. To do so, we first identify the sub-space of Horndeski theories in which models are *both* stable and compatible with current constraints on $f\sigma_8(z)$. Detailed description about how we carry this out can be found in Appendix B.1.

After we have determined a sub-space of Horndeski theories compaitable with current data, we then follow the procedure outlined here:

1. We sample this theory sub-space, i.e. randomly draw Horndeski models from the sub-space and calculate the theoretical prediction for $f\sigma_8(z)$ by each model; this is described in Section 4.3.1.

2. For each model, we quantify the goodness-of-fit between the $f\sigma_8(z)$ computed using various proposed fitting formulae for $\gamma(z)$ and the actual theory prediction. To compute the fit, we use the forecast constraints on $f\sigma_8(z)$ from Stage IV and V surveys; this is discussed in Section 4.3.2.

Finally, we compare the goodness-of-fits and identify the best functional form for $\gamma(z)$. Figure 4.1 depicts the entire procedure.

4.3.1 Sampling and evaluating Horndeski models

Following the preliminary runs and cuts described in Appendix B.1, we identify a particular sub-space of Horndeski theories where models that are both stable and consistent with current data constraints on $f\sigma_8$:

Table 4.1: Fiducial values of cosmological parameters and priors on them used in our sampling of Horndeski models. They closely follow the ΛCDMbest-fit values and 68% in the Planck 2018 analysis [13].

Parameter	Fiducial value	Prior distribution
$\Omega_b h^2$	0.022383	$\mathcal{N}(0.022383, 0.00015)$
$\Omega_c h^2$	0.12011	$\mathcal{N}(0.12011, 0.0012)$
H_0	67.32	$\mathcal{N}(67.32, 0.54)$
w	-1.0	Fixed
A_s	2.086×10^{-9}	
n_s	0.9666	
τ	0.0543	

$$
\begin{aligned}
\Omega^{\mathrm{MG},0} &\in \mathcal{U}[0.0, 0.1], & s_0 &\in \mathcal{U}[0, 3] \\
\gamma_1^{\mathrm{MG},0} &\in \mathcal{U}[0.0, 0.7], & s_1 &\in \mathcal{U}[-3, 3], \\
\gamma_2^{\mathrm{MG},0} &\in \mathcal{U}[-1.0, 0.0], & s_2 &\in \mathcal{U}[0, 3], \\
\gamma_3^{\mathrm{MG},0} &\in \mathcal{U}[0.0, 1.0], & s_3 &\in \mathcal{U}[1, 3].
\end{aligned}
\tag{4.14}
$$

Eq. 4.14 specify our priors on EFTDE parameters from which we sample Horndeski models in our main analysis. They are in broad agreement with the corresponding posteriors reported in [83].

From the Horndeski priors in Eq. 4.14 and cosmological priors in Table 4.1, we first draw and evaluate a sample of ~20,000 Horndeski models using `EFTCAMB`. Of these, 19,908 models pass the stability conditions imposed within `EFTCAMB` (see Section 4.2). For each model successfully evaluated by `EFTCAMB`, we use its prediction of $f\sigma_8(z)$ to recompute the quantity $\chi^2_{\text{current data}}$ given in Eq. B.2 and reject those with $\chi^2_{\text{current data}} > 5\sigma$ (same cut as in Appendix B.1). We thereby end up with a final set of 18,543 viable Horndeski models and we only use *these* models to test our fitting formulae and identify the most accurate one.

4.3.2 Testing the functional forms for $\gamma(z)$

In this section, we describe the procedure to fit the growth index $\gamma(z)$ in Eq. 4.2 parameterized by different functional forms to Horndeski models, assuming future $f\sigma_8$ data.

The final fitting formula must be sufficiently accurate even for future measurements of structure growth in the coming years and decades. We therefore assume optimistic constraints given by

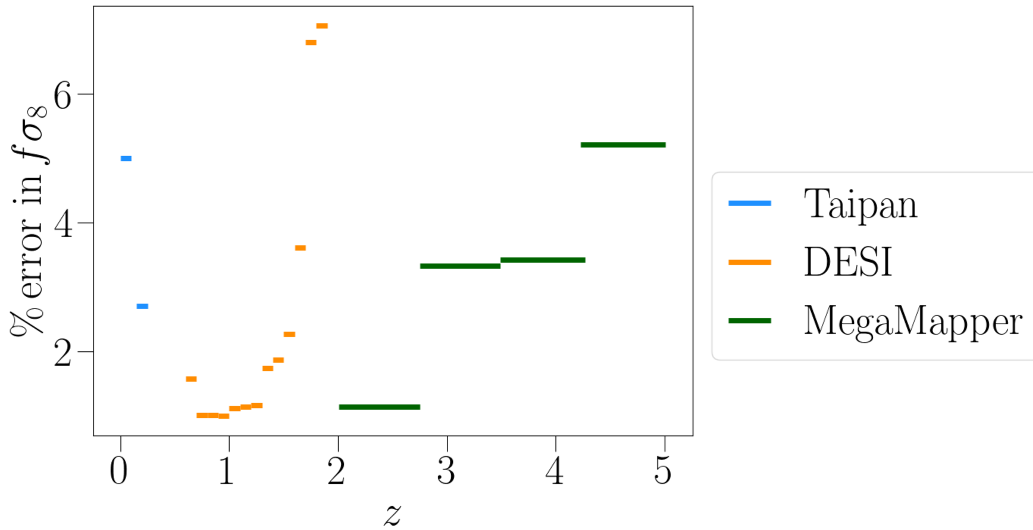

Figure 4.2: Future $f\sigma_8(z)$ error forecasts that we use to assess the accuracy of the fitting formulae for the growth rate. The width of each line segment indicates the size of the redshift bin while the height shows the magnitude of the forecast error.

future data considered in this work. In this way, we impose a higher burden of proof for any proposed fitting formula. Specifically, we choose the measurements of and constraints on $f\sigma_8(z)$ from several future surveys that together cover a redshift span up to $z_{\text{max}} = 5$, as demonstrated in Figure 4.2 and listed in Table 4.3. In the low-redshift region, we adopt forecast error bars based on the Taipan Galaxy Survey [61], assuming a 5% error at $z = 0.05$ and a 2.7% error at $z = 0.2$. In the intermediate redshift range of $0.65 < z < 1.85$, we adopt the DESI forecasts [69] where errors are in bins of size $\Delta z = 0.1$ as given in Table 4.3. In the high redshift region, we use forecasts from MegaMapper[5] where errors are in four bins of size $\Delta z = 0.75$.

For every Horndeski model (generated following the protocols described in Appendix B.1), we assume future data centered on the predictions of that model, with errors representative of Stage IV and V surveys shown in Table 4.3. We then fit this simulated data with a number of distinct two-parameter fitting formulae for $\gamma(z)$. To perform each fit, we employ the `iminuit` optimization package to find the best-fit values of the two fitting-formula parameters, γ_0 and γ_1 that minimizes χ^2_{fit}, which is defined as

$$\chi^2_{\text{fit}} \equiv \sum_i \frac{[(f\sigma_8)^{\text{fit}}(z_i) - (f\sigma_8)^{\text{model}}(z_i)]^2}{(\sigma_i^{\text{future data}})^2}. \tag{4.15}$$

Here $(f\sigma_8)^{\text{model}}(z)$ is the value obtained directly from `EFTCAMB` following the definition in Eq. 4.12;

[5]The $f\sigma_8$ constraint forecast for MegaMapper was obtained through a joint fit to $\{\Omega_c, \Omega_b, h, \log A_s\}$, marginalizing over galaxy bias and nuisance parameters.

in $(f\sigma_8)^{\rm fit}(z)$, $f(z)$ was calculated by each of the two-parameter parameterizations listed in Table 4.4 and $\sigma_8(z)$ obtained from `EFTCAMB` following the definition in Eq. 4.13; $\sigma_i^{\rm future\ data}$ is the error on the i-th future measurement at redshift z_i, both of which are given in Table 4.3. Finally, we select the fitting formula of $\gamma(z)$ that gives the best goodness-of-fit across all sampled Horndeski models.

4.4 Results

We now present the two principal results of this paper. In Section 4.4.1, we show the performance of different parameterizations of $\gamma(z)$ in their fit to theoretical predictions of $f\sigma_8$ in Horndeski models, and identify the best fitting formula. In Section 4.4.2 we constrain the parameters of the best fitting function using current cosmological data.

4.4.1 And the winner is...

To first get a sense of what kind of $\gamma(z)$ typically predicted by Horndeski models, we numerically compute the redshift-dependent growth index for a limited number of models. Specifically, we evaluate

$$\gamma(z) \equiv \frac{\ln f(z)}{\ln \Omega_M(z)} \tag{4.16}$$

given $f(z)$ and $\Omega_M(z)$ in that model. Figure 4.3 shows the exact $\gamma(z)$ computed from Eq. 4.16 in 50 randomly selected Horndeski models from our prior. To guide the eye we also plot the ΛCDM growth index which, as expected, is very well approximated by $\gamma(z) \simeq 0.55$. The general behavior of $\gamma(z)$ in Horndeski models at $z \gtrsim 1$ can be easily understood from Eq. 4.16: as z increases, $\Omega_M(z) \to 1$ in cosmological models without early dark energy (which is true for all models considered in this paper). Therefore, for any given (Horndeski) model, departures of the growth rate $f(z \gtrsim 1)$ from the ΛCDM prediction are generally associated with relatively large fluctuations in the the growth index simply because the latter is the exponent of $\Omega_M(z)$. Overall, the results in Figure 4.3 not only show a clear redshift evolution of the growth index expected in these models, but also demonstrate that this redshift dependence is fairly featureless.

The results in Figure 4.3 motivate our selection of specific functional forms of the growth index and Table 4.4 enumerates these functions. In addition to the constant growth index and (for pure simplicity) the one going linearly with z, we also try several other forms that contain simple polynomials in redshift, as well as simple logarithmic or exponential terms. Since we would like to parameterize $f\sigma_8(z)$ up to $z \simeq 5$ where Stage IV and V data will constrain growth, trends in Figure 4.3 emphasize that we need a nonlinear redshift-dependent parameterization, such as those suggested in Table 4.4.

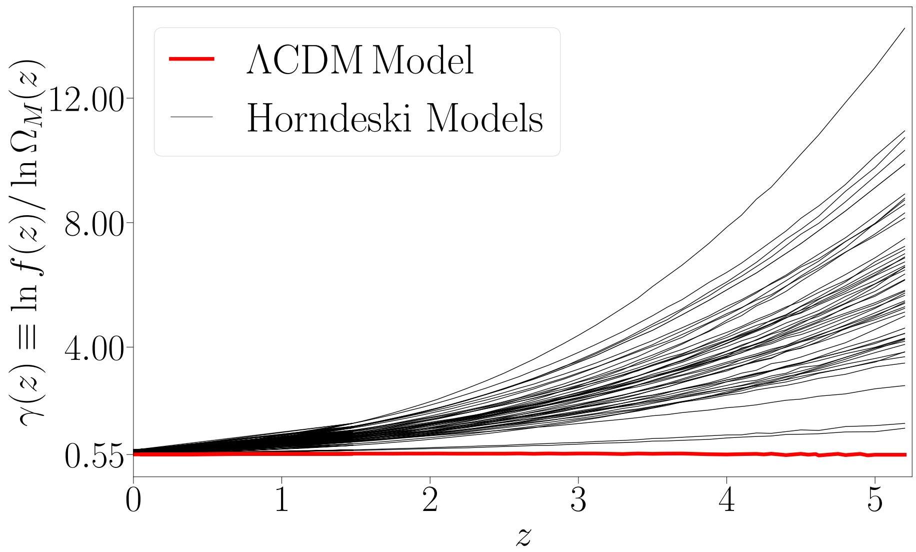

Figure 4.3: The exact redshift-dependent growth index, $\gamma(z) \equiv \ln f(z)/\ln \Omega_m(z)$, numerically evaluated for 50 randomly selected Horndeski models from our prior out to $z_{\rm max} \simeq 5$. The red nearly horizontal line shows the exact $\gamma(z)$ for the ΛCDM model. These results demonstrate that one needs a nonlinear multi-parameter parameterization to capture the features of growth index at high redshift in modified gravity. They also motivate functional forms for our trial fitting functions in Table 4.4.

The success (or failure) of each parameterization in fitting theoretical predictions of Horndeski models is further reported in Table 4.4. For each fitting function, we summarize the statistics of the quantity $\chi^2_{\rm fit}$, defined in Eq. 4.15, measured for our set of ~18,000 Horndeski models. The summary is provided by two statistical measures: the median of the $\chi^2_{\rm fit}$ values, and the 95-th percentile (i.e. the upper bound of 95% of values of $\chi^2_{\rm fit}$). Since the theoretical data vector is calculated by `EFTCAMB` is noiseless, a perfect fit of a fitting formula to true $f\sigma_8(z)$ of a theory model will have $\chi^2_{\rm fit} = 0$; this explains the generally small chi-squared values in Table 4.4. In general, we find that the distribution of the $\chi^2_{\rm fit}$ values has a heavy tail in each instance; this explains why the 95% upper bounds are typically much larger than the corresponding medians in Table 4.4. The presence of the heavy tails reflects the improvement of $f\sigma_8$ constraints going from Stage III to Stage IV and V surveys: our model selection cut, Eq. B.2, is only concerned with current constraints on $f\sigma_8$, while our comparison by Eq. 4.15 is only concerned with forecast constraints for Stage IV and V surveys.

As shown by the highlighted cell in Table 4.4, the best fitting formula for the growth index in the redshift range of $0 < z < 5$ is

$$\gamma(z) = \gamma_0 + \gamma_1 \frac{z^2}{1+z}. \tag{4.17}$$

This two-parameter fitting formula fits the future data with a median $\chi^2_{\rm fit}$ of 0.028, which is about 40 times smaller than the median $\chi^2_{\rm fit}$ with the constant growth index $\gamma(z) = \gamma_0$. Furthermore, we find that with the new fitting formula from Eq. 4.17, the maximum deviation in $f\sigma_8(z)$ at any redshift between the fitting formula's approximation and Horndeski theory's true value for $f\sigma_8(z)$ has a median of 0.4% when averaged over all models. When using the traditional one-parameter growth index, $\gamma(z) = \gamma_0$, the median of maximum differences per model is 2.5%. Our two-parameter, redshift-dependent fitting formula therefore approximates the theoretical predictions of $f\sigma_8(z)$ in Horndeski theories about six times better than the one-parameter, constant-γ case, leading to an improvement of ~ 40 times in χ^2.

Several other fitting functions in Table 4.4, also do a good job, in particular $\gamma(z) = \gamma_0 + \gamma_1 z$ comes close in the median, but falls short in fitting models near the tail; however, none are as good as the form in Eq. 4.17.

The result that the median $\chi^2_{\rm fit} \ll 1$ with the best fitting function is very encouraging, as it implies that the contribution of the inaccurate fitting function to the bias in cosmological parameters will be subdominant. Specifically, our finding that $\chi^2_{\rm fit} \ll 1$ implies that even the best-determined direction in parameter space will be biased by $\ll 1\sigma$ in our optimistic-data case.

In Figure 4.4, we further showcase the performance of a few proposed fitting formulae on one randomly selected Horndeski model. It is evident that the prize-winning fitting form in Eq. 4.17 is the best of the fitting functions shown. We also observe that the best fitting function does a good job both at $z \ll 1$ and at $z > 1$; both of these ranges are required to be accurately fit for the (γ_0, γ_1) description to be a useful tool for the Stage IV and V surveys.

4.4.2 Constraint on $\gamma(z) = \gamma_0 + \gamma_1 z^2/(1+z)$ from current data

In the previous section, we have proposed and validated Eq. 4.17 as a new fitting function of the growth index $\gamma(z)$ for future surveys. Using current cosmological data, we now demonstrate the applicability of this formula in consistency tests of general relativity and flat ΛCDM.

Building upon the work in [149], here we constrain the growth index $\gamma(z)$, specifically (γ_0, γ_1) in Eq. 4.17, from a combination of large-scale structure and CMB data sets: measurements of $f\sigma_8$ through peculiar velocity and redshift-space distortions[6] [39, 108, 182, 46, 207, 42, 43, 99, 151, 162, 16], measurements of baryon acoustic oscillation (BAO) from the Six-degree Field Galaxy Survey (6dFGS; [37]) and the Sloan Digital Sky Survey (SDSS; [177, 15, 16]), 3x2pt correlation functions from the Year-1 analysis of Dark Energy Survey (DES-Y1; [3]), and CMB measurements from Planck 2018 [13]. In this work, we additionally include the type Ia supernovae data sets and likelihoods from Pantheon [190] which however make very little difference in our final constraints on (γ_0, γ_1). To obtain constraints on the growth-index and cosmological parameters (after numerically

[6]Fig. 2 of [149] show these $f\sigma_8$ measurements and their error bars.

marginalizing over nuisance parameters), we use `cobaya`[7], which provides out-of-the-box access to most likelihoods for the aforementioned data sets, validated against their official analyses. The only exception is the $f\sigma_8$ likelihood for [39, 108, 182, 46, 207, 42, 43, 99, 151, 162], which we implement in [149], assuming a Gaussian likelihood and a diagonal covariance.

Our implementation of the growth index largely follows that of [149]. Specifically, at any given redshift z, we re-scale the linear matter power spectrum as

$$P(\gamma, k, z) = P(k, z = 0)\, D^2(\gamma, z), \tag{4.18}$$

where $D(\gamma, z)$ is numerically integrated from Eqs. 4.1–4.2, and $P(k, z = 0)$ is the fiducial linear matter power spectrum evaluated at $z = 0$ which is specified by the standard set of cosmological parameters:

$$\{A_s, n_s, \Omega_c h^2, \Omega_b h^2, \tau, \theta_{\rm MC}\}, \tag{4.19}$$

where A_s and n_s are the amplitude and the spectral index of the primordial power spectrum, τ is the reionization optical depth, and $\theta_{\rm MC}$ is (an approximation to) the angular size of the sound horizon at recombination. We emphasize that this set of cosmological parameters are jointly constrained with (γ_0, γ_1). When sampling with `cobaya`, we compute $P(k, z)$ using the cosmological Boltzmann solver `CAMB` [131, 98]. We validate our implementation by reproducing, up to a high precision, the constraints on the standard cosmological parameters in the baseline analyses of Planck 2018 [13] and DES-Y1 [3].

Motivated by the fact that Eq. 4.2 has, so far, been validated only for sub-horizon perturbations, we exempt the primary CMB anisotropies from the rescaling in Eq. 4.18. In other words, the growth index never directly affect the *unlensed* CMB power spectra, but rather only the CMB lensing potential. Consequently, only the CMB lensing amplitude is sensitive to any change in the growth index[8] γ.

For the cosmological parameters, we adopt the same priors as specified in the Planck 2018 baseline analysis [13], which considered flat ΛCDM at fixed neutrino mass $\sum m_\nu = 0.06$ eV. Priors on all nuisance parameters also follow those in the official analyses of the corresponding data sets. We choose uniform priors on the two growth-index parameters as: $\gamma_0 \in \mathcal{U}(0.0, 2.0)$, $\gamma_1 \in \mathcal{U}(-1.0, 1.0)$.

In Figure 4.5 we present the constraints in the $\gamma_0 - \gamma_1$ plane, marginalized over all other cosmological and nuisance parameters. Allowing for redshift evolution, which is effectively controlled by the parameter γ_1 in $\gamma(z) = \gamma_0 + \gamma_1 z^2/(1 + z)$, we observe the expected degeneracy between γ_1

[7] https://cobaya.readthedocs.io/en/latest/

[8] Note that, strictly speaking, γ should also affect the integrated Sachs-Wolfe (ISW) effect but here we do not consider a separate ISW likelihood. For more details on the latter, see [53].

and γ_0 in that parameterization. Specifically, we infer $\gamma_0 = 0.621 \pm 0.03$ and $\gamma_1 = 0.149 \pm 0.235$. We find evidence for a disagreement with the standard cosmological model — which predicts $(\gamma_0 = 0.55, \gamma_1 = 0)$ — at approximately 99.8% level (corresponding to about "3.1-sigma" in a two-tailed test of statistical significance). Our finding is therefore in good statistical agreement with the conclusion from the analysis in [149] which however assumed $\gamma = \text{const.}$, i.e. no redshift evolution.

Our γ_0 constraint suggests that the growth rate of large-scale structure is recently suppressed — with the onset of dark energy — relative to the prediction by flat ΛCDM and general relativity, while the γ_1 constraint implies no (strong) evidence of redshift evolution in the growth index.

4.5 Summary and Conclusions

In order to squeeze out stringent constraints on the growth of structure from data, it will be crucial to have precise parameterizations of the evolution of the growth of structure, specifically with the goal to cleanly separate it from the background evolution. One such parameterization is $f(z) = \Omega_M(z)^\gamma$ with a constant growth index γ which, while being highly accurate for dark-energy models close to ΛCDM, is no longer such for modified gravity. In this work, we have promoted γ to a function of redshift, i.e. $\gamma(z)$. We have further identified and validated the best two-parameter fitting formula for $\gamma(z)$ that accurately describes the growth of structure across the landscape of Horndeski theories of modified gravity:

$$f(z) = \Omega_M(z)^{\gamma_0 + \gamma_1 z^2/(1+z)}. \tag{4.20}$$

We have explicitly shown that Eq. 4.20 fits the theoretical predictions of $f\sigma_8(z)$ by Horndeski models with typical errors at the sub-percent level, well-within the precision that will be reached by Stage IV and Stage V surveys.

Further, as a demonstration, we have constrained the parameters of Eq. 4.20 using modern data from galaxy clustering, weak lensing, CMB, and type Ia supernovae. The result we obtained is in tension with the concordance cosmological model of $(\gamma_0, \gamma_1) = (0.55, 0)$ — which was expected given such indications in our recent analysis which essentially assumed $\gamma(z) = \gamma_0$ [149]. Specifically, we have found evidence that $\gamma_0 > 0.55$, while the posterior of γ_1 peaks at positive values but is statistically consistent with zero.

We conclude that forthcoming data from ongoing and upcoming large-scale structure surveys [61, 87, 186, 199, 126, 188] will dramatically expand the redshift coverage and increase the precision of the growth-of-structure sector. This, in turn, will enable new opportunities to test the self-consistency of the standard cosmological model, and possibly detect deviations from general relativity from such measurements of the growth rate. Our new fitting formula should provide one reliable meeting point between data and theory.

Table 4.2: Current measurements of $f\sigma_8$ and errors at different redshifts. The data include the 6dF Galaxy Survey (6dFGS), peculiar velocities of type Ia supernovae (SNIa), Galaxy and Mass Assembly (GAMA), the WiggleZ Dark Energy Survey, the Baryon Oscillation Spectroscopic Survey (BOSS), the extended Baryon Oscillation Spectroscopic Survey (eBOSS) and the VIMOS Public Extragalactic Redshift Survey (VIPERS).

Redshift	$f\sigma_8$	$\sigma_{f\sigma_8}$	**Survey/Probe**
0	0.418	0.065	6dFGS [114]
0	0.40	0.07	SNIa [204]
0.067	0.423	0.055	6dFGS [38]
0.18	0.44	0.06	GAMA [43]
0.38	0.44	0.06	
0.22	0.42	0.07	WiggleZ [42]
0.41	0.45	0.04	
0.60	0.43	0.04	
0.78	0.38	0.04	
0.38	0.482	0.053	BOSS [40]
0.51	0.455	0.050	
0.61	0.410	0.042	
0.57	0.441	0.044	BOSS RSD [184]
0.15	0.53	0.16	eBOSS [16]
0.38	0.500	0.047	
0.51	0.455	0.039	
0.70	0.448	0.043	
0.85	0.315	0.095	
1.48	0.462	0.045	
0.80	0.47	0.08	VIPERS [65]

Table 4.3: Constraints on $f\sigma_8$ from future surveys that cover a redshift range of up to $z_{\rm max} = 5$. This is also visualized in Figure 4.2.

Redshift	**% Error in $f\sigma_8(z)$**	**Survey/Probe**
0.05	5	Taipan [61]
0.2	2.7	
0.65	1.57	DESI [69]
0.75	1.01	
0.85	1.0	
0.95	0.99	
1.05	1.11	
1.15	1.14	
1.25	1.16	
1.35	1.73	
1.45	1.87	
1.55	2.27	
1.65	3.61	
1.75	6.81	
1.85	7.07	
2.38	1.13	MegaMapper
3.12	3.33	
3.88	3.42	
4.62	5.21	

Table 4.4: Proposed fitting functions and the statistics of their fit to our sample of ∼18,000 Horndeski models.

Fitting function for $\gamma(z)$	**Best-fit χ^2 Median**	**Best-fit χ^2 95% Percentile**
γ_0	1.16	36.6
$\gamma_0 + \gamma_1 z$	0.046	4.00
$\gamma_0 + \gamma_1 z^2$	0.11	2.48
$\gamma_0 + \gamma_1 z/(1+z)$	0.22	14.7
$\gamma_0 + \gamma_1 z^2/(1+z)$	0.028	1.08
$\gamma_0 + \gamma_1 z^3/(1+z)$	0.26	6.58
$\gamma_0 + \gamma_1 \exp(z)$	0.28	6.91
$\gamma_0 + \gamma_1 z^3 \exp(-z)$	0.10	2.63

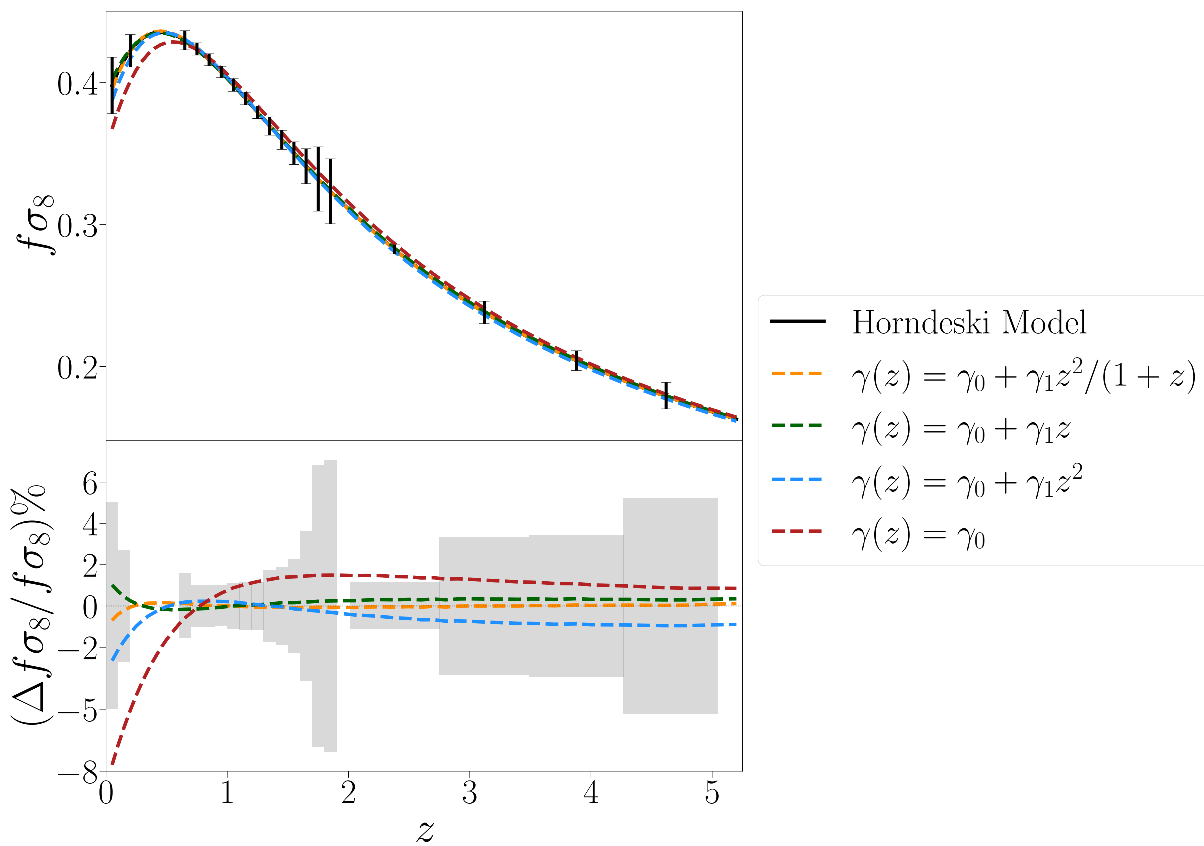

Figure 4.4: *Top panel*: The $f\sigma_8(z)$ of an example Horndeski model (black curve, based on parameters $\Omega^{\mathrm{MG},0} = 0.074$, $s_0 = 2.33$, $\gamma_1^{\mathrm{MG},0} = 0.15$, $s_1 = -0.57$, $\gamma_2^{\mathrm{MG},0} = -0.92$, $s_2 = 1.48$, $\gamma_3^{\mathrm{MG},0} = 0.75$ and $s_3 = 1.43$) computed by `EFTCAMB` with error bars forecast for future surveys from Table 4.3: Taipan, DESI and MegaMapper. We also show the best-fitting $f\sigma_8(z)$ for three fitting formulae for the growth index $\gamma(z)$, as well as the $f\sigma_8$ fit from a constant growth index, $\gamma(z) = \gamma_0$. *Bottom panel*: Relative difference between the true $f\sigma_8(z)$ and the best-fit results of each fitting formula shown in the top panel. The shaded grey area shows the forecast statistical errors associated with each survey.

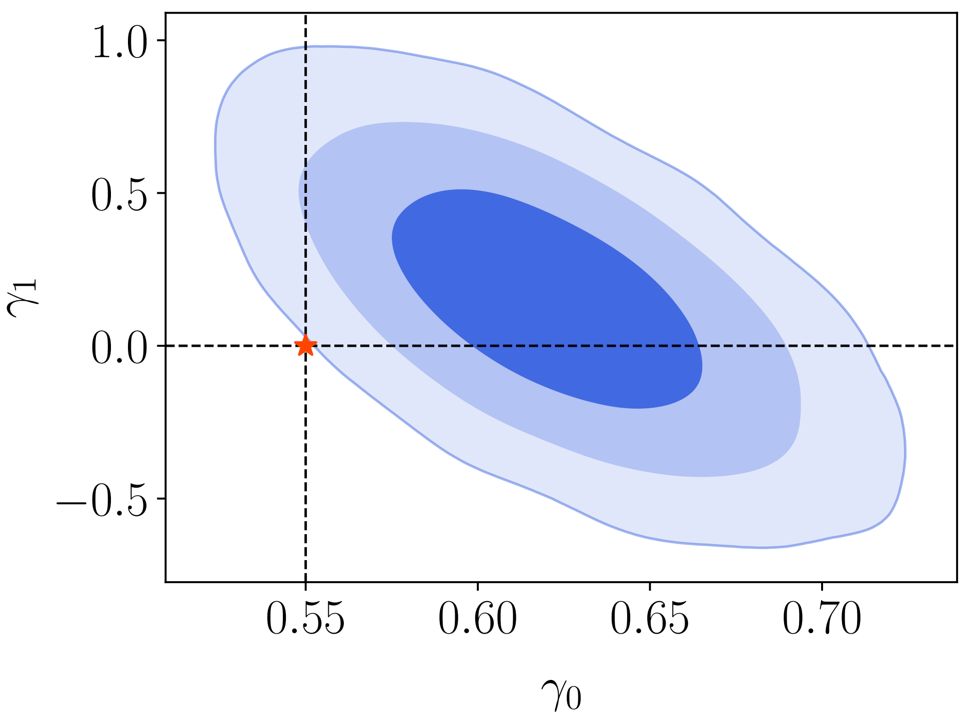

Figure 4.5: Constraints from current cosmological data on parameters (γ_0, γ_1) in the growth-index parameterization $\gamma(z) = \gamma_0 + \gamma_1 z^2/(1+z)$. Contours in the $\gamma_0 - \gamma_1$ 2D plane represent (68%, 95%, 99.73%) of the posterior volume.

CHAPTER 5

Outlook

Understanding what physically motivated the late-time accelerated expansion of the Universe is the crucial question in cosmology today. The development of precision cosmology, especially the building of large scale structure and CMB surveys, opens up enormous possibilities in front of us.

The rich data collected from existing and future surveys are essential in constraining the properties of dark energy, tracing the temporal growth of cosmic structure and testing theories beyond general relativity.

Without a consensus on the true theory behind the late-time cosmic acceleration, having a proper description of dark energy that can be easily implemented in cosmological data analysis is essential. This is exemplified in parameterizing the dark energy component with its equation of state w (or the commonly used (w_0, w_a) parameterization if incorporating time variations), allowing dark energy parameters to be constrained by different cosmological probes, as discussed in details in Section 1.1.4.

The large scale structure and its temporal evolution is a very sensitive probe of the properties of dark energy and the underlying theory of gravity. Therefore, it is also essential to parameterize growth-related quantities that can be tightly constrained by the next generation of surveys like DESI. A good parameterization should not only fit current observations well but also provide convenient inroads in probing dark energy and modified-gravity models.

The work in Chapter 3 studies the existing popular parameterization of the linear growth rate — the growth index γ. The value $\gamma = 0.55$ can model linear growth to sub-percent level for a wide range of models with dark energy that assumes general relativity and flat background. In this work, we constrain the growth index with $f\sigma_8$ data from peculiar velocities and RSD surveys plus Planck 2018 CMB and galaxy surveys. Our combined data set excludes $\gamma = 0.55$ by 3.7σ and favors a suppression of growth in late times (a higher value in γ). We also find that when γ is not fixed and allowed to vary freely, the tension in S_8 between CMB and lensing surveys is reduced from 3.2σ to 0.9σ. We then investigate the scenario when spatial curvature is allowed to be nonzero as we vary γ using only Planck CMB data, a choice motivated by the nonzero curvature concluded by Planck 2018 analysis. The result shows a trade-off relation between a positive curvature and suppressed growth, both of which produce similar oscillatory features in the CMB temperature power spectrum. When future measurements of $f\sigma_8(z)$, BAO, galaxy clustering and weak lensing from DESI, LSST and MegaMapper become available, we will be able to see whether this tension with the concordance cosmology is further enlarged or reduced, providing us with more information of what might have given rise to it.

The work in Chapter 4 studies the growth index as well, but investigates its generalized form when modifications to GR are considered. Focusing on the Horndeski class of modified-gravity theories, we demonstrate the necessity of including redshift dependence into the growth index, extending it from a constant γ to $\gamma(z, \{\gamma_0, \gamma_1\})$. The best fitting formula we have found is $\gamma(z) = \gamma_0 + \gamma_1 z^2/(1+z)$. Assuming optimistic future constraints in the redshift range $0 < z < 5$, the new parameterization improved the goodness-of-fit to Horndeski models by 40 times, compared to the popular constant form of growth index. The new parameter γ_1 can be used as an indicator for modified gravity. We use large scale structure and CMB data to constraint γ_0 and γ_1, and these constraints will be further improved by future data.

These two works together take a step in understanding and testing modified gravity theories through the cosmic growth. As current data shows evidence of suppression of growth at late times when compared to a flat ΛCDM model, its theoretical cause remains to be investigated, an endeavour that can be facilitated by the proposed two-parameter fitting formula of the growth index. For instance, a sub-class of Horndeski models can suppress growth at late times [164, 158, 157]. With improvements in measurement precision, sky coverage and analysis pipelines in future surveys, the γ_1 parameter can produce better implications for studying modified-gravity theories.

In the meantime, as major advances are made on the observational side of cosmology, there is a growing need to understand their implications on dark energy and modified-gravity models. As it is more common and relatively more straight forward to go from theory space to cosmological parameters, i.e. finding a theory's constraint on observables, mapping directly from observational parameters to a subspace of modified-gravity theories is a far more convoluted task.

The work in Chapter 2 takes a stab at this issue and provides a viable scheme to resolve it. If the true underlying theory of the Universe is described by a certain modified-gravity theory, we find that standard cosmological analysis without this knowledge can still show hints of modified gravity — shifts in best-fit values of cosmological parameters in a generally uniform direction. Scanning through a broad range of modified-gravity models and studying parameter shifts when they are misinterpreted as unmodified phenomenological dark energy models, we discover that the shifted parameter values lie along a very tight region in cosmological parameter space, indicating that a deviation in parameter values outside of this region does not arise from modified gravity but comes from other systematics. One natural expansion of the analysis pipeline we present is to incorporate more cosmological probes, such as weak lensing and galaxy clustering. And with the upcoming Stage-IV surveys, we will likely be able to identify a subspace of modified gravity theories that are more consistent with data.

All three aforementioned works have provided examples of how cosmological surveys can be employed to study and distinguish competing models of dark energy and modified gravity and how next generation of surveys could further sharpen these results. Therefore, we here give a brief overview of what to expect from these future instruments and missions.

One of the most ambitious photometric surveys in the 2020s that will probe dark energy is the Rubin Observatory's Legacy Survey of Space and Time (LSST). The Rubin telescope is wide-field and ground-based and has an 8.4-meter mirror. It will carry out a multi-band survey that will cover a large sky area of more than 18,000 deg^2, an order of magnitude improvement compared to current surveys [111]. Its goal is to provide high quality images of 40 billion objects [111], from which cosmological analysis involving major probes of dark energy — weak lensing, galaxy clustering, BAO and type Ia supernovae — can be conducted with high accuracy. When combined with other spectroscopic, IR and CMB surveys, LSST's constraints on geometry and cosmic growth will be used to probe our Universe's underlying theory of gravity.

Another future large-scale structure survey is Euclid, a space telescope that will be launched very soon in July, 2023. It will probe dark energy equation of state as well as theories of gravity through a wide-field photometric and spectroscopic survey that covers 15,000 deg^2 of the sky [185]. Providing weak lensing shear and galaxy clustering measurements, along with the "3x2 pt" analysis, Euclid will be able to constrain the expansion history of the Universe and the temporal growth of cosmic structure. Constraints on $w(z)$ and the growth index γ will be improved to the level where key aspects of the concordance cosmological model can be effectively tested [185].

Dark Energy Spectroscopic Instrument (DESI) is a Stage-IV spectroscopic galaxy survey that uses a 4-meter Mayall Telescope at Kitt Peak National Observatory in Arizona. It will map out the large-scale structure and the expansion history over the past 11 billion years through spectroscopic BAO measurements, improving by an order of magnitude the volume and number of galaxies it observes [10]. Covering a sky of 14,000 deg^2 and equipped with the capability of simultaneously taking 5,000 spectra, DESI will provide redshift measurements of millions of galaxies, which will effectively help construct the three-dimensional map of our Universe whose scope extends much beyond past surveys. Targets of DESI include bright galaxies that can be observed even during full moon up to $z \sim 0.4$, luminous red galaxies up to $z \sim 1$, bright emission line galaxies up to $z \sim 1.7$ and quasars up to $z \sim 3.5$. Measuring BAO and RSD from this wide-area and high redshift survey, DESI will be able to provide percent level distance measurements [10], which will hugely facilitate our mapping of the expansion history and hence properties of dark energy.

DESI II, a stage-V survey and an upgrade to DESI, will further expand the volume and redshift range that will be probed, going into regions of $z > 2$. Measuring the redshift of ~40 million galaxies up to high redshift, DESI-II enables more insight into inflation, dark energy and modified gravity models. For instance, mapping out galaxies and matter density distribution up to a high redshift can function as a lever arm between dark energy-dominated and matter-dominated era, potentially constraining many classes of modified gravity and early dark energy models [187]. Moreover, when combining low-redshift peculiar velocities with measurements of galaxies clustering at high redshift, both DESI and DESI-II will greatly improve constraints on cosmic growth, including the growth-index γ, which two works in this dissertation focus on.

Another high-redshift Stage-V survey is MegaMapper, a proposed ground-based survey that will use galaxies from $z \sim 2$ up to $z \sim 5$ to probe inflation and dark energy [188]. When combined with imaging from the LSST, we will be able to gain access to ~100 million spectroscopic objects in this high-redshift range. With these huge advances, MegaMapper expects to constrain the energy density parameter of dark energy Ω_{DE} to 2% up to $z \simeq 5$, as well as greatly tightening constraints on spatial curvature (compared to DESI and Planck) and dark energy equation of state [188] .

Besides large-scale structure surveys, measurements of type Ia supernovae are being greatly advanced in the upcoming epoch as well. The Wide-Field InfraRed Space Telescope (WFIRST), or the Nancy Grace Roman Space Telescope as it is named now, is a near-infrared telescope equipped with a wide-field instrument to probe dark energy. It will conduct a type Ia supernovae survey to map out the geometry of the Universe on large scales through having larger statistical samples and lower systematics [97]. Covering a redshift range up to $z \simeq 2$, WFIRST will be able to monitor the light curves of thousands of SNe Ia during its mission time and measure distance moduli to the precision of below 1% [78, 97].

Wider sky coverage, higher imaging quality, probing higher redshift regions and more precise distance measurements — all of these have laid the foundation for nailing down key properties of dark energy and potentially understanding its physical nature. The three works in this dissertation contribute to the effort of mining more deeply into the rich observational data and concretely mapping out connections between cosmological parameters and the pool of existing modified-gravity theories.

APPENDIX A

Misinterpreting Modified Gravity as Dark Energy Appendices

A.1 Fitting error of the emulator and minimization package

Here, we illustrate the extent of uncertainty in our process of finding best-fits. In each panel of Fig. A.1, there are 93 blue points, each generated from fitting the 8 standard cosmological parameters to the fiducial cosmology listed in Table 2.1. The dim light grey, green and red points in the background are the same as the corresponding points in Fig. 2.3, and in both figures they denote the best-fit parameter values to Horndeski data vectors. For a perfect fitting process, the blue points should all coincide with the grey cross-hair, which indicates the fiducial values of each parameter. Our fitting error, as indicated by level of scatter among the blue points and the historgrams, is small compared to both the best-fits to Horndeski data vectors and the parameters' allowed ranges of variation.

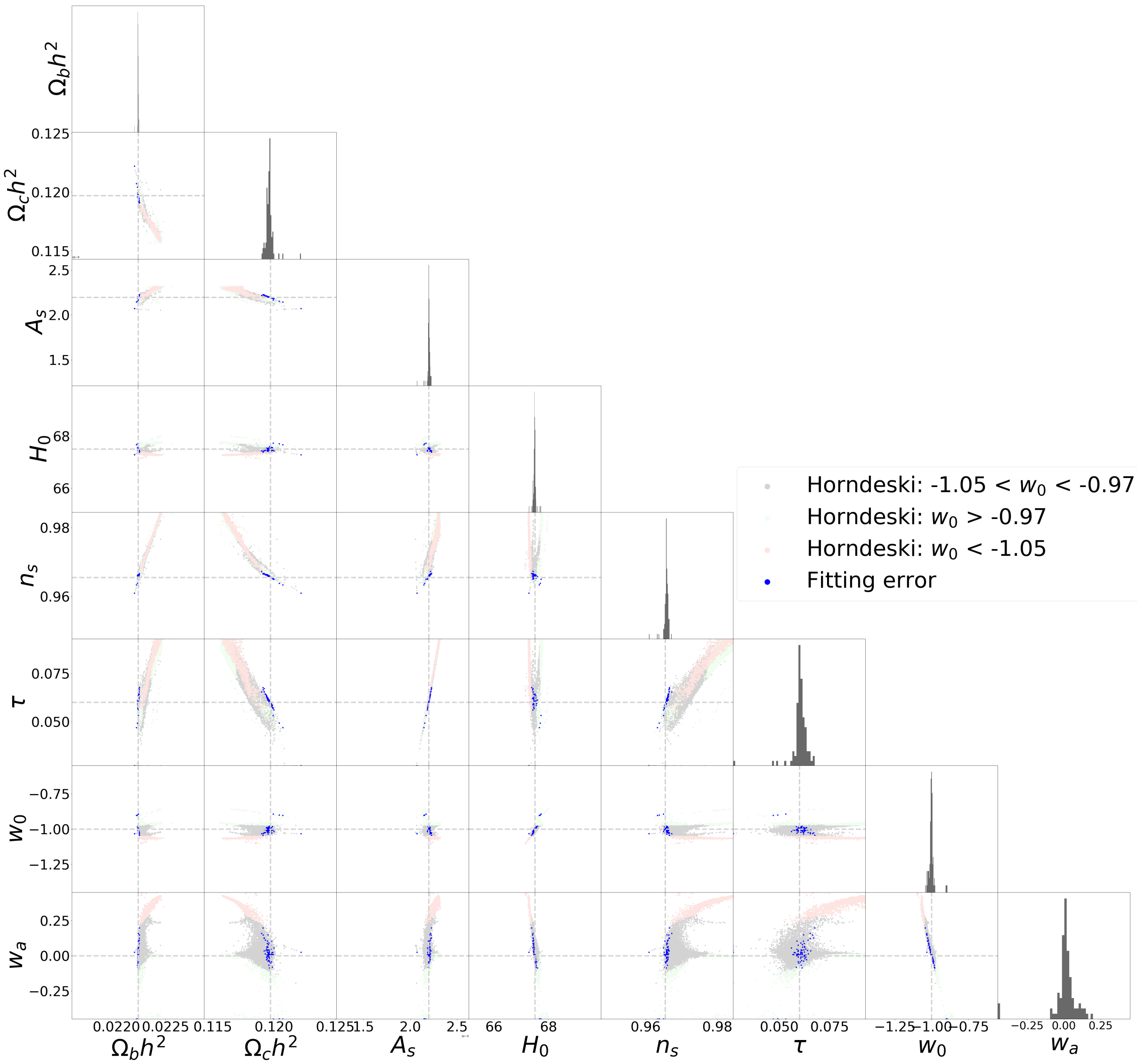

Figure A.1: A test of the performance of the emulator and our minimization tool, `iminuit`. The test consists of 93 separate fits of cosmological parameters to the same CMB power spectrum generated by `CAMB` (with input parameter values as in Table 2.1); each fit starts from a different, randomly chosen, starting point in parameter space. The best-fits parameter values are plotted as the blue points in each panel (superimposed to results from Fig. 2.3). The histograms on the diagonal show the distribution of the recovered values for the corresponding parameter on the vertical axis. These results demonstrate that the emulator and `iminuit` successfully and accurately recover the input cosmological parameter values, which are shown by the cross-hair in each panel.

.

APPENDIX B

New Parameterization of Growth Rate in Horndeski Models Appendix

B.1 Determining sampling ranges for EFTDE and Horndeski parameters

In this work, we need to sample and evaluate a large number of models from the Horndeski theory space. Therefore, it is crucial to identify the sub-space of Horndeski models that are stable and compatible with current observations, in particular those of $f\sigma_8 8$ — our main observable in the present study. We enforce this requirement following a two-step procedure:

1. First, we draw the standard cosmological parameters $\Omega_b h^2$, $\Omega_c h^2$, and H_0 in Eq. 4.8 from the 1D marginal posteriors in Planck 2018 baseline analysis [13]. We fix the rest of the background cosmological parameters, including the amplitude of the primordial power spectrum A_s (at pivot wave number $k_{\rm piv} = 0.05\ \mathrm{Mpc}^{-1}$), the scalar spectral index n_s and the optical depth to reionization τ, to the Planck 2018 baseline best-fit values (see first column of Tab. 1 in [13]). For clarity, we summarize the parameter prior ranges and values in Table 4.1. Next, we draw the EFT parameters in Eq. 4.8 from the following ranges

$$
\begin{aligned}
\Omega^{\rm MG,0} &\in \mathcal{U}[0, 0.1], & s_0 &\in \mathcal{U}[0, 3]; \\
\gamma_1^{\rm MG,0} &\in \mathcal{U}[0.0, 1.0], & s_1 &\in \mathcal{U}[-3, 3]; \\
\gamma_2^{\rm MG,0} &\in \mathcal{U}[-1.0, 1.0], & s_2 &\in \mathcal{U}[-3, 3]; \\
\gamma_3^{\rm MG,0} &\in \mathcal{U}[0.0, 1.0], & s_3 &\in \mathcal{U}[-3, 3],
\end{aligned}
\tag{B.1}
$$

   where $\mathcal{U}[a, b]$ denotes a uniform distribution between a and b.

2. In the second step, we then choose to exclude cosmological models — specified by the above

cosmological parameters and EFT parameters — that are disfavored by current data at $\geq 5\sigma$. The current $f\sigma_8$ data that we use are shown in Table 4.2. We define the goodness of fit to the theoretical model value as

$$\chi^2_{\text{current data}} \equiv \sum_i \frac{[(f\sigma_8)^{\text{current data}}(z_i) - (f\sigma_8)^{\text{model}}(z_i)]^2}{(\sigma_i^{\text{current data}})^2} \tag{B.2}$$

where $(f\sigma_8)^{\text{model}}(z)$ is the value obtained from `EFTCAMB`, and $(f\sigma_8)^{\text{current data}}$, $\sigma_i^{\text{current data}}$, and z_i are respectively the measurement, error, and redshift of current data, all of which are given in Table 4.2. Similar to [81], we typically find that — although model stability can strongly depends on $\gamma_1^{\text{MG},0}$ and s_1 — model prediction (in our case, for $f\sigma_8$) does not. With 20 $f\sigma_8$ measurements and six EFT parameters to be fit, this leaves $N_{\text{dof}} = 14$ degrees of freedom. Assuming a normal distribution of individual $f\sigma_8$ measurements, keeping the models that are within 5σ from current measurements then requires $\chi^2 \leq 60$.

During this process, we also prune regions of the Horndeski parameter space where models largely fail the stability conditions specified in Section 4.2.2. We thereby end up with the prior ranges specified in Eq. 4.14.

B.2 Scale dependence of growth

Here we take a closer look at the scale dependence of the growth rate $f(z,k)$ specifically in the context of Horndeski models. As mentioned near the end of Sec. 4.2, this scale-dependence is not guaranteed to be negligible for growth in models beyond smooth dark energy. By using `EFTCAMB` we can straightforwardly investigate the effect by directly computing the linear growth as the ratio of the matter transfer functions at two different redshifts

$$D(z,k) = \frac{T(z,k)}{T(z=0,k)} \tag{B.3}$$

and then numerically evaluating $f(z,k)$ from Eq. 4.1.

We do find significant k dependence of $f(z,k)$ near the horizon scale ($k \simeq 0.0001 - 0.001 h\,\text{Mpc}^{-1}$). However, remember that most cosmological observations of large-scale structure come from smaller scales, roughly $k \simeq 0.01 - 0.1 h\,\text{Mpc}^{-1}$ (see, for example, Fig. 19 in the Planck legacy paper [11]). Therefore, we do not need to take into account the scale dependence of $f(z)$ if we focus on this range of scales. This is clearly demonstrated in Figure B.1 where we show the k dependence of $f\sigma_8(z)$ on two scales, $k = 0.01$ and $0.1\ h\,\text{Mpc}^{-1}$, for a selection of a few Horndeski models from our priors (as well as for ΛCDM). When selecting the Horndeski models to showcase in Figure B.1, we sequentially increase each EFT parameter to its largest value allowed by the priors specified in Eq. (4.14).

The maximum scale dependence that we observe in Figure B.1 is about 0.5% — much lower than the (statistical) errors in $f\sigma_8$ of all surveys considered in this work. We thus demonstrate that for Horndeski models that deviate most from general relativity (and potentially have the most scale-dependence) but still within the our selected priors, the difference in $f\sigma_8(z)$ are well below 1% and much smaller than stringent constraints from future surveys.

We also quantitatively demonstrate the scale-independence of Horndeski models within our specified priors. Among ~18,000 Horndeski models, we find that the difference between the values of $f(z,k)$ evaluated at $k = 0.01$ and $0.1\,h\,\mathrm{Mpc}^{-1}$ (across all models and all redshifts) has a median of 0.3% and a 95% percentile of 0.5%, both at a sub-percent level.

Nevertheless, there are reasons why studying the scale dependence of the growth of structure is very interesting and should be pursued. First, modified-gravity models that are physically different from models in our Horndeski prior may lead to a much more significant scale dependence. Second, observations that probe larger spatial scales (say $k \sim 0.001\,h\,\mathrm{Mpc}^{-1}$) might also be able to observe this scale dependence behavior.

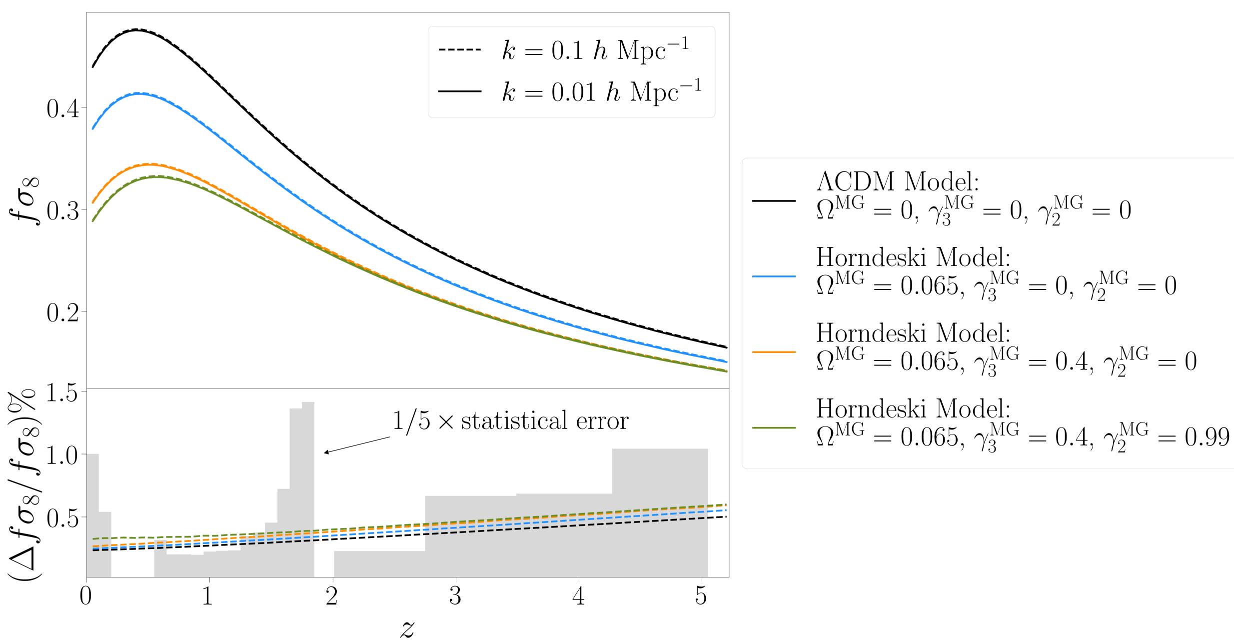

Figure B.1: *Top panel:* $f\sigma_8(z)$ of a ΛCDM and three Horndeski models calculated by `EFTCAMB` at scales $k = 0.1\ h\ \mathrm{Mpc}^{-1}$ and $k = 0.01\ h\ \mathrm{Mpc}^{-1}$. *Bottom panel:* The percent difference between $f\sigma_8(z)$ of each Horndeski model calculated at these two scales. The shaded area illustrates the constraints on $f\sigma_8(z)$ by future surveys in terms of percent error at each redshift bin, which we use in determining the goodness-of-fit of each proposed fitting formula. For visualization purposes, we scale them down to 1/5 when displayed in the bottom panel.

BIBLIOGRAPHY

[1] Kevork N. Abazajian et al. CMB-S4 Science Book, First Edition. *arXiv e-prints*, page arXiv:1610.02743, October 2016.

[2] B. P. Abbott et al. Gravitational Waves and Gamma-Rays from a Binary Neutron Star Merger: GW170817 and GRB 170817A. ApJ, 848(2):L13, October 2017.

[3] T. M. C. Abbott et al. Dark Energy Survey year 1 results: Cosmological constraints from galaxy clustering and weak lensing. Phys. Rev. D, 98(4):043526, August 2018.

[4] T. M. C. Abbott et al. Dark Energy Survey Year 1 Results: Constraints on Extended Cosmological Models from Galaxy Clustering and Weak Lensing. *Phys. Rev. D*, 99(12):123505, 2019.

[5] T. M. C. Abbott et al. Dark Energy Survey Year 3 results: Constraints on extensions to ΛCDM with weak lensing and galaxy clustering. *Phys. Rev. D*, 107(8):083504, 2023.

[6] Elcio Abdalla et al. Cosmology intertwined: A review of the particle physics, astrophysics, and cosmology associated with the cosmological tensions and anomalies. *JHEAp*, 34:49–211, 2022.

[7] P. A. R. Ade et al. Planck 2013 results. I. Overview of products and scientific results. *Astron. Astrophys.*, 571:A1, 2014.

[8] P. A. R. Ade et al. Planck 2015 results. XIII. Cosmological parameters. *Astron. Astrophys.*, 594:A13, 2016.

[9] Peter Ade et al. The Simons Observatory: science goals and forecasts. J. Cosmology Astropart. Phys., 2019(2):056, February 2019.

[10] Amir Aghamousa et al. The DESI Experiment Part I: Science,Targeting, and Survey Design. 10 2016.

[11] N. Aghanim et al. Planck 2018 results. I. Overview and the cosmological legacy of Planck. *Astron. Astrophys.*, 641:A1, 2020.

[12] N. Aghanim et al. Planck 2018 results. V. CMB power spectra and likelihoods. A&A, 641:A5, September 2020.

[13] N. Aghanim et al. Planck 2018 results. VI. Cosmological parameters. *Astron. Astrophys.*, 641:A6, 2020. [Erratum: Astron.Astrophys. 652, C4 (2021)].

[14] Simone Aiola et al. The Atacama Cosmology Telescope: DR4 maps and cosmological parameters. J. Cosmology Astropart. Phys., 2020(12):047, December 2020.

[15] Shadab Alam et al. The clustering of galaxies in the completed SDSS-III Baryon Oscillation Spectroscopic Survey: cosmological analysis of the DR12 galaxy sample. *Mon. Not. Roy. Astron. Soc.*, 470(3):2617–2652, 2017.

[16] Shadab Alam et al. Completed SDSS-IV extended Baryon Oscillation Spectroscopic Survey: Cosmological implications from two decades of spectroscopic surveys at the Apache Point Observatory. Phys. Rev. D, 103(8):083533, April 2021.

[17] Shadab Alam, Shirley Ho, and Alessandra Silvestri. Testing deviations from ΛCDM with growth rate measurements from six large-scale structure surveys at z = 0.06-1. *Monthly Notices of the RAS*, 456(4):3743–3756, March 2016.

[18] E. Allys et al. Probing Cosmic Inflation with the LiteBIRD Cosmic Microwave Background Polarization Survey. *arXiv e-prints*, page arXiv:2202.02773, February 2022.

[19] Luca Amendola. Cosmology with nonminimal derivative couplings. *Physics Letters B*, 301(2-3):175–182, March 1993.

[20] Luca Amendola, Dario Bettoni, Guillem Domènech, and Adalto R. Gomes. Doppelgänger dark energy: modified gravity with non-universal couplings after GW170817. *JCAP*, 06:029, 2018.

[21] A. Amon et al. KiDS+2dFLenS+GAMA: Testing the cosmological model with the E_{G} statistic. *Mon. Not. Roy. Astron. Soc.*, 479(3):3422–3437, 2018.

[22] A. Amon et al. Consistent lensing and clustering in a low-S_8 Universe with BOSS, DES Year 3, HSC Year 1, and KiDS-1000. *Monthly Notices of the RAS*, 518(1):477–503, January 2023.

[23] Uendert Andrade, Dhayaa Anbajagane, Rodrigo von Marttens, Dragan Huterer, and Jailson Alcaniz. A test of the standard cosmological model with geometry and growth. J. Cosmology Astropart. Phys., 2021(11):014, November 2021.

[24] Christian Arnold, Matteo Leo, and Baojiu Li. Realistic simulations of galaxy formation in f(R) modified gravity. *Nature Astronomy*, 3(10):945–954, 2019.

[25] John Baker et al. Multimessenger science opportunities with mHz gravitational waves. 3 2019.

[26] Tessa Baker, Pedro G. Ferreira, C. Danielle Leonard, and Mariele Motta. New gravitational scales in cosmological surveys. *Phys. Rev. D*, 90:124030, Dec 2014.

[27] Alexandre Barreira, Baojiu Li, Carlton M. Baugh, and Silvia Pascoli. Linear perturbations in galileon gravity models. *Phys. Rev. D*, 86:124016, Dec 2012.

[28] Spyros Basilakos. Linear growth in power law $f(T)$ gravity. *Phys. Rev. D*, 93(8):083007, 2016.

[29] Spyros Basilakos and Fotios K. Anagnostopoulos. Growth index of matter perturbations in the light of Dark Energy Survey. *European Physical Journal C*, 80(3):212, March 2020.

[30] Richard A. Battye, Francesco Pace, and Damien Trinh. Gravitational wave constraints on dark sector models. *Phys. Rev. D*, 98(2):023504, 2018.

[31] Rachel Bean and Matipon Tangmatitham. Current constraints on the cosmic growth history. *Phys. Rev.*, D81:083534, 2010.

[32] Emilio Bellini, Antonio J. Cuesta, Raul Jimenez, and Licia Verde. Constraints on deviations from ΛCDM within Horndeski gravity. *JCAP*, 02:053, 2016. [Erratum: JCAP 06, E01 (2016)].

[33] Emilio Bellini and Ignacy Sawicki. Maximal freedom at minimum cost: linear large-scale structure in general modifications of gravity. *JCAP*, 07:050, 2014.

[34] Alicia Bueno Belloso, Juan García-Bellido, and Domenico Sapone. A parametrization of the growth index of matter perturbations in various dark energy models and observational prospects using a euclid-like survey. *Journal of Cosmology and Astroparticle Physics*, 2011(10):010, oct 2011.

[35] José Luis Bernal, Licia Verde, and Antonio J. Cuesta. Parameter splitting in dark energy: is dark energy the same in the background and in the cosmic structures? J. Cosmology Astropart. Phys., 2016(2):059–059, February 2016.

[36] F. Bernardeau, S. Colombi, E. Gaztañaga, and R. Scoccimarro. Large-scale structure of the Universe and cosmological perturbation theory. Phys. Rep., 367(1-3):1–248, September 2002.

[37] Florian Beutler, Chris Blake, Matthew Colless, D. Heath Jones, Lister Staveley-Smith, Lachlan Campbell, Quentin Parker, Will Saunders, and Fred Watson. The 6dF Galaxy Survey: baryon acoustic oscillations and the local Hubble constant. *Monthly Notices of the RAS*, 416(4):3017–3032, October 2011.

[38] Florian Beutler, Chris Blake, Matthew Colless, D. Heath Jones, Lister Staveley-Smith, Gregory B. Poole, Lachlan Campbell, Quentin Parker, Will Saunders, and Fred Watson. The 6dF Galaxy Survey: $z \approx 0$ measurement of the growth rate and σ_8. *Mon. Not. Roy. Astron. Soc.*, 423:3430–3444, 2012.

[39] Florian Beutler, Chris Blake, Matthew Colless, D. Heath Jones, Lister Staveley-Smith, Gregory B. Poole, Lachlan Campbell, Quentin Parker, Will Saunders, and Fred Watson. The 6dF Galaxy Survey: z$\approx$ 0 measurements of the growth rate and σ_8. *Monthly Notices of the RAS*, 423(4):3430–3444, July 2012.

[40] Florian Beutler et al. The clustering of galaxies in the completed SDSS-III Baryon Oscillation Spectroscopic Survey: Anisotropic galaxy clustering in Fourier-space. *Mon. Not. Roy. Astron. Soc.*, 466(2):2242–2260, 2017.

[41] Florian Beutler et al. The clustering of galaxies in the completed SDSS-III Baryon Oscillation Spectroscopic Survey: baryon acoustic oscillations in the Fourier space. *Mon. Not. Roy. Astron. Soc.*, 464(3):3409–3430, 2017.

[42] Chris Blake et al. The WiggleZ Dark Energy Survey: the growth rate of cosmic structure since redshift z=0.9. *Mon. Not. Roy. Astron. Soc.*, 415:2876, 2011.

[43] Chris Blake et al. Galaxy And Mass Assembly (GAMA): improved cosmic growth measurements using multiple tracers of large-scale structure. *Monthly Notices of the RAS*, 436(4):3089–3105, December 2013.

[44] M. Blanton and the Sloan Digital Sky Survey. SDSS Galaxy Map. Online; accessed May 13, 2023.

[45] Jolyon K. Bloomfield, Éanna É. Flanagan, Minjoon Park, and Scott Watson. Dark energy or modified gravity? An effective field theory approach. *JCAP*, 08:010, 2013.

[46] Supranta S. Boruah, Michael J. Hudson, and Guilhem Lavaux. Cosmic flows in the nearby Universe: new peculiar velocities from SNe and cosmological constraints. *Monthly Notices of the RAS*, 498(2):2703–2718, October 2020.

[47] Matteo Braglia, Mario Ballardini, Fabio Finelli, and Kazuya Koyama. Early modified gravity in light of the H_0 tension and LSS data. *Phys. Rev. D*, 103(4):043528, 2021.

[48] C. Brans and R. H. Dicke. Mach's principle and a relativistic theory of gravitation. *Phys. Rev.*, 124:925–935, Nov 1961.

[49] Dillon Brout et al. The Pantheon+ Analysis: Cosmological Constraints. *Astrophys. J.*, 938(2):110, 2022.

[50] R. Calderon, D. Felbacq, R. Gannouji, D. Polarski, and A. A. Starobinsky. Global properties of the growth index: mathematical aspects and physical relevance. *Phys. Rev. D*, 101(10):103501, 2020.

[51] Robert Caldwell, Asantha Cooray, and Alessandro Melchiorri. Constraints on a New Post-General Relativity Cosmological Parameter. *Phys. Rev.*, D76:023507, 2007.

[52] Sean M. Carroll. The Cosmological constant. *Living Rev. Rel.*, 4:1, 2001.

[53] Julien Carron, Antony Lewis, and Giulio Fabbian. Planck integrated Sachs-Wolfe-lensing likelihood and the CMB temperature. *Phys. Rev. D*, 106(10):103507, 2022.

[54] Shi-Fan Chen, Martin White, Joseph DeRose, and Nickolas Kokron. Cosmological analysis of three-dimensional BOSS galaxy clustering and Planck CMB lensing cross correlations via Lagrangian perturbation theory. J. Cosmology Astropart. Phys., 2022(7):041, July 2022.

[55] Clifford Cheung, Paolo Creminelli, A. Liam Fitzpatrick, Jared Kaplan, and Leonardo Senatore. The Effective Field Theory of Inflation. *JHEP*, 03:014, 2008.

[56] Takeshi Chiba, Takahiro Okabe, and Masahide Yamaguchi. Kinetically driven quintessence. *Phys. Rev. D*, 62:023511, 2000.

[57] Timothy Clifton, Pedro G. Ferreira, Antonio Padilla, and Constantinos Skordis. Modified gravity and cosmology. *Physics Reports*, 513(1-3):1–189, 2012.

[58] Asantha Cooray, Dragan Huterer, and Daniel Baumann. Growth rate of large scale structure as a powerful probe of dark energy. *Phys. Rev. D*, 69:027301, 2004.

[59] Asantha R. Cooray and Dragan Huterer. Gravitational lensing as a probe of quintessence. *Astrophys. J. Lett.*, 513:L95–L98, 1999.

[60] Edmund J. Copeland, M. Sami, and Shinji Tsujikawa. Dynamics of dark energy. *International Journal of Modern Physics D*, 15(11):1753–1935, 2006.

[61] Elisabete da Cunha et al. The taipan galaxy survey: Scientific goals and observing strategy. *Publications of the Astronomical Society of Australia*, 34, 06 2017.

[62] Scott F. Daniel and Eric V. Linder. Confronting General Relativity with Further Cosmological Data. *Phys. Rev. D*, 82:103523, 2010.

[63] Scott F. Daniel and Eric V. Linder. Constraining Cosmic Expansion and Gravity with Galaxy Redshift Surveys. *JCAP*, 1302:007, 2013.

[64] Scott F. Daniel, Eric V. Linder, Tristan L. Smith, Robert R. Caldwell, Asantha Cooray, Alexie Leauthaud, and Lucas Lombriser. Testing General Relativity with Current Cosmological Data. *Phys. Rev.*, D81:123508, 2010.

[65] S. de la Torre et al. The VIMOS Public Extragalactic Redshift Survey (VIPERS). Galaxy clustering and redshift-space distortions at z=0.8 in the first data release. *Astron. Astrophys.*, 557:A54, 2013.

[66] Claudia de Rham and Scott Melville. Gravitational Rainbows: LIGO and Dark Energy at its Cutoff. *Phys. Rev. Lett.*, 121(22):221101, 2018.

[67] Cédric Deffayet, Oriol Pujolàs, Ignacy Sawicki, and Alexander Vikman. Imperfect dark energy from kinetic gravity braiding. J. Cosmology Astropart. Phys., 2010(10):026, October 2010.

[68] J. DeRose et al. Dark Energy Survey Year 3 results: Cosmology from combined galaxy clustering and lensing validation on cosmological simulations. *Phys. Rev. D*, 105(12):123520, 2022.

[69] DESI Collaboration. The DESI Experiment Part I: Science,Targeting, and Survey Design. *arXiv e-prints*, page arXiv:1611.00036, October 2016.

[70] Eleonora Di Valentino et al. Cosmology Intertwined III: $f\sigma_8$ and S_8. *Astropart. Phys.*, 131:102604, 2021.

[71] Eleonora Di Valentino, William Giarè, Alessandro Melchiorri, and Joseph Silk. Health checkup test of the standard cosmological model in view of recent cosmic microwave background anisotropies experiments. Phys. Rev. D, 106(10):103506, November 2022.

[72] Eleonora Di Valentino, Alessandro Melchiorri, and Joseph Silk. Planck evidence for a closed Universe and a possible crisis for cosmology. *Nature Astronomy*, 4:196–203, February 2020.

[73] Eleonora Di Valentino, Olga Mena, Supriya Pan, Luca Visinelli, Weiqiang Yang, Alessandro Melchiorri, David F. Mota, Adam G. Riess, and Joseph Silk. In the realm of the Hubble tension - a review of solutions. *Class. Quant. Grav.*, 38(15):153001, 2021.

[74] Scott Dodelson. *Modern Cosmology*. Academic Press, Amsterdam, 2003.

[75] Jason Dossett, Mustapha Ishak, Jacob Moldenhauer, Yungui Gong, Anzhong Wang, and Yungui Gong. Constraints on growth index parameters from current and future observations. *JCAP*, 04:022, 2010.

[76] D. Scolnic et al. SUPERCAL: CROSS-CALIBRATION OF MULTIPLE PHOTOMETRIC SYSTEMS TO IMPROVE COSMOLOGICAL MEASUREMENTS WITH TYPE ia SUPERNOVAE. *The Astrophysical Journal*, 815(2):117, dec 2015.

[77] N. Suzuki et al. *The Astrophysical Journal*, 746(1):85, jan 2012.

[78] Rachel Akeson et al. The wide field infrared survey telescope: 100 hubbles for the 2020s, 2019.

[79] Jose María Ezquiaga and Miguel Zumalacárregui. Dark Energy in light of Multi-Messenger Gravitational-Wave astronomy. *Frontiers in Astronomy and Space Sciences*, 5:44, December 2018.

[80] Joshua Frieman, Michael Turner, and Dragan Huterer. Dark Energy and the Accelerating Universe. *Ann. Rev. Astron. Astrophys.*, 46:385–432, 2008.

[81] Noemi Frusciante, Georgios Papadomanolakis, and Alessandra Silvestri. An Extended action for the effective field theory of dark energy: a stability analysis and a complete guide to the mapping at the basis of EFTCAMB. *JCAP*, 07:018, 2016.

[82] Noemi Frusciante, Simone Peirone, Santiago Casas, and Nelson A. Lima. Cosmology of surviving Horndeski theory: The road ahead. Phys. Rev. D, 99(6):063538, March 2019.

[83] Noemi Frusciante and Louis Perenon. Effective field theory of dark energy: A review. *Phys. Rept.*, 857:1–63, 2020.

[84] J. N. Fry. Dynamical measures of density in exotic cosmologies. *Physics Letters B*, 158(3):211–214, August 1985.

[85] R. Gannouji, B. Moraes, and D. Polarski. The growth of matter perturbations in f(R) models. *JCAP*, 02:034, 2009.

[86] Carlos García-García, Jaime Ruiz-Zapatero, David Alonso, Emilio Bellini, Pedro G. Ferreira, Eva-Maria Mueller, Andrina Nicola, and Pilar Ruiz-Lapuente. The growth of density perturbations in the last 10 billion years from tomographic large-scale structure data. J. Cosmology Astropart. Phys., 2021(10):030, October 2021.

[87] Karl Gebhardt et al. The Hobby-Eberly Telescope Dark Energy Experiment (HETDEX) Survey Design, Reductions, and Detections. ApJ, 923(2):217, December 2021.

[88] Yungui Gong. Growth factor parametrization and modified gravity. Phys. Rev. D, 78(12):123010, December 2008.

[89] Yungui Gong, Mustapha Ishak, and Anzhong Wang. Growth factor parametrization in curved space. Phys. Rev. D, 80(2):023002, July 2009.

[90] Giulia Gubitosi, Federico Piazza, and Filippo Vernizzi. The Effective Field Theory of Dark Energy. *JCAP*, 02:032, 2013.

[91] Jacek Guzik, Bhuvnesh Jain, and Masahiro Takada. Tests of Gravity from Imaging and Spectroscopic Surveys. *Phys. Rev.*, D81:023503, 2010.

[92] Will Handley. Curvature tension: Evidence for a closed universe. *"Phys. Rev. D"*, 103(4):L041301, February 2021.

[93] Katrin Heitmann, David Higdon, Martin White, Salman Habib, Brian J. Williams, Earl Lawrence, and Christian Wagner. The coyote universe. II. cosmological models and precision emulation of the nonlinear matter power spectrum. *Astrophysical Journal*, 705(1):156–174, 2009.

[94] Catherine Heymans et al. KiDS-1000 Cosmology: Multi-probe weak gravitational lensing and spectroscopic galaxy clustering constraints. A&A, 646:A140, February 2021.

[95] Alireza Hojjati, Aaron Plahn, Alex Zucca, Levon Pogosian, Philippe Brax, Anne-Christine Davis, and Gong-Bo Zhao. Searching for scalar gravitational interactions in current and future cosmological data. *Phys. Rev.*, D93(4):043531, 2016.

[96] Jiamin Hou, Bautista Julian, Berti Maria, Cuesta-Lazaro Carolina, Hernández-Aguayo César, Tröster Tilman, and Zheng Jinglan. Probes of Structure Growth and tests of Gravity. under review.

[97] R. Hounsell et al. Simulations of the WFIRST Supernova Survey and Forecasts of Cosmological Constraints. *Astrophys. J.*, 867(1):23, 2018.

[98] Cullan Howlett, Antony Lewis, Alex Hall, and Anthony Challinor. CMB power spectrum parameter degeneracies in the era of precision cosmology. J. Cosmology Astropart. Phys., 1204:027, 2012.

[99] Cullan Howlett, Ashley J. Ross, Lado Samushia, Will J. Percival, and Marc Manera. The clustering of the SDSS main galaxy sample - II. Mock galaxy catalogues and a measurement of the growth of structure from redshift space distortions at z = 0.15. *Monthly Notices of the RAS*, 449(1):848–866, May 2015.

[100] Bin Hu, Marco Raveri, Noemi Frusciante, and Alessandra Silvestri. Effective Field Theory of Cosmic Acceleration: an implementation in CAMB. *Phys. Rev. D*, 89(10):103530, 2014.

[101] Bin Hu, Marco Raveri, Noemi Frusciante, and Alessandra Silvestri. EFT-CAMB/EFTCosmoMC: Numerical Notes v3.0. 5 2014.

[102] Wayne Hu and Ignacy Sawicki. Models of $f(r)$ cosmic acceleration that evade solar system tests. *Phys. Rev. D*, 76:064004, Sep 2007.

[103] Edwin Hubble. A relation between distance and radial velocity among extra-galactic nebulae. *Proc. Nat. Acad. Sci.*, 15:168–173, 1929.

[104] Michael J. Hudson and Stephen J. Turnbull. The Growth Rate of Cosmic Structure from Peculiar Velocities at Low and High Redshifts. *The Astrophysical Journal*, 751(2):L30, June 2012.

[105] Dragan Huterer. Growth of Cosmic Structure. 12 2022.

[106] Dragan Huterer. *A Course in Cosmology*. Cambridge University Press, 3 2023.

[107] Dragan Huterer and Eric V. Linder. Separating Dark Physics from Physical Darkness: Minimalist Modified Gravity vs. Dark Energy. *Phys. Rev. D*, 75:023519, 2007.

[108] Dragan Huterer, Daniel Shafer, Daniel Scolnic, and Fabian Schmidt. Testing ΛCDM at the lowest redshifts with SN Ia and galaxy velocities. *JCAP*, 1705(05):015, 2017.

[109] Dragan Huterer and Daniel L Shafer. Dark energy two decades after: Observables, probes, consistency tests. *Rept. Prog. Phys.*, 81(1):016901, 2018.

[110] Dragan Huterer and Glenn Starkman. Parameterization of dark-energy properties: A Principal-component approach. *Phys. Rev. Lett.*, 90:031301, 2003.

[111] Željko Ivezić et al. LSST: from Science Drivers to Reference Design and Anticipated Data Products. *Astrophys. J.*, 873(2):111, 2019.

[112] Harold Jeffreys. *Theory of Probability*. Oxford University Press, 1939.

[113] Andrew Johnson, Chris Blake, Jason Dossett, Jun Koda, David Parkinson, and Shahab Joudaki. Searching for modified gravity: scale and redshift dependent constraints from galaxy peculiar velocities. *"Mon. Not. Roy. Astron. Soc."*, 458(3):2725–2744, May 2016.

[114] Andrew Johnson, Chris Blake, Jun Koda, Yin-Zhe Ma, Matthew Colless, Martin Crocce, Tamara M. Davis, Heath Jones, Christina Magoulas, John R. Lucey, Jeremy Mould, Morag I. Scrimgeour, and Christopher M. Springob. The 6dF Galaxy Survey: cosmological constraints from the velocity power spectrum. MNRAS, 444(4):3926–3947, November 2014.

[115] Shahab Joudaki et al. KiDS-450: Testing extensions to the standard cosmological model. *Mon. Not. Roy. Astron. Soc.*, 471(2):1259–1279, 2017.

[116] Austin Joyce, Bhuvnesh Jain, Justin Khoury, and Mark Trodden. Beyond the cosmological standard model. *Physics Reports*, 568:1–98, 2015.

[117] Austin Joyce, Lucas Lombriser, and Fabian Schmidt. Dark Energy Versus Modified Gravity. *Ann. Rev. Nucl. Part. Sci.*, 66:95–122, 2016.

[118] Joshua A. Kable, Giampaolo Benevento, Noemi Frusciante, Antonio De Felice, and Shinji Tsujikawa. Probing modified gravity with integrated Sachs-Wolfe CMB and galaxy cross-correlations. J. Cosmology Astropart. Phys., 2022(9):002, September 2022.

[119] Alexander Yu. Kamenshchik, Ugo Moschella, and Vincent Pasquier. An Alternative to quintessence. *Phys. Lett. B*, 511:265–268, 2001.

[120] Ryotaro Kase and Shinji Tsujikawa. Dark energy in Horndeski theories after GW170817: A review. *Int. J. Mod. Phys. D*, 28(05):1942005, 2019.

[121] Justin Khoury and Amanda Weltman. Chameleon cosmology. Phys. Rev. D, 69(4):044026, February 2004.

[122] Wompherdeiki Khyllep and Jibitesh Dutta. Linear growth index of matter perturbations in Rastall gravity. *Phys. Lett. B*, 797:134796, 2019.

[123] Wompherdeiki Khyllep, Andronikos Paliathanasis, and Jibitesh Dutta. Cosmological solutions and growth index of matter perturbations in $f(Q)$ gravity. *Phys. Rev. D*, 103(10):103521, 2021.

[124] Tsutomu Kobayashi. Horndeski theory and beyond: a review. *Rept. Prog. Phys.*, 82(8):086901, 2019.

[125] C. D. Kreisch and E. Komatsu. Cosmological Constraints on Horndeski Gravity in Light of GW170817. *JCAP*, 12:030, 2018.

[126] R. Laureijs et al. Euclid Definition Study Report. *arXiv e-prints*, page arXiv:1110.3193, October 2011.

[127] A. Leauthaud et al. Lensing without borders - I. A blind comparison of the amplitude of galaxy-galaxy lensing between independent imaging surveys. *Monthly Notices of the RAS*, 510(4):6150–6189, March 2022.

[128] S. Lee et al. Probing gravity with the DES-CMASS sample and BOSS spectroscopy. 4 2021.

[129] Seokcheon Lee and Kin-Wang Ng. Growth index with the exact analytic solution of sub-horizon scale linear perturbation for dark energy models with constant equation of state. *Physics Letters B*, 688(1):1–3, April 2010.

[130] Antony Lewis. GetDist: a Python package for analysing Monte Carlo samples. *arXiv e-prints*, 2019.

[131] Antony Lewis, Anthony Challinor, and Anthony Lasenby. Efficient computation of CMB anisotropies in closed FRW models. ApJ, 538:473–476, 2000.

[132] Xiaolei Li, Noah Weaverdyck, Saroj Adhikari, Dragan Huterer, Jessica Muir, and Hao-Yi Wu. The Quest for the Inflationary Spectral Runnings in the Presence of Systematic Errors. *Astrophys. J.*, 862(2):137, 2018.

[133] Alan P. Lightman and Paul L. Schechter. The Omega Dependence of Peculiar Velocities Induced by Spherical Density Perturbations. ApJS, 74:831, December 1990.

[134] Meng-Xiang Lin, Marco Raveri, and Wayne Hu. Phenomenology of Modified Gravity at Recombination. *Phys. Rev. D*, 99(4):043514, 2019.

[135] Eric V. Linder. Exploring the expansion history of the universe. *Phys. Rev. Lett.*, 90:091301, 2003.

[136] Eric V. Linder. Cosmic growth history and expansion history. *Phys. Rev.*, D72:043529, 2005.

[137] Eric V. Linder. Biased Cosmology: Pivots, Parameters, and Figures of Merit. *Astropart. Phys.*, 26:102–110, 2006.

[138] Eric V. Linder. The Mirage of w=-1. 8 2007.

[139] Eric V. Linder and Robert N. Cahn. Parameterized Beyond-Einstein Growth. *Astropart. Phys.*, 28:481–488, 2007.

[140] Eric V. Linder and David Polarski. End of cosmic growth. Phys. Rev. D, 99(2):023503, January 2019.

[141] Eric V. Linder, Gizem Sengör, and Scott Watson. Is the Effective Field Theory of Dark Energy Effective? *JCAP*, 05:053, 2016.

[142] Nareg Mirzatuny and Elena Pierpaoli. An accurate fitting function for scale-dependent growth rate in Hu-Sawicki f(R) gravity. J. Cosmology Astropart. Phys., 2019(9):066, September 2019.

[143] Myles A. Mitchell, Christian Arnold, and Baojiu Li. A general framework to test gravity using galaxy clusters V: A self-consistent pipeline for unbiased constraints of $f(R)$ gravity. *Mon. Not. Roy. Astron. Soc.*, 508:4157, 2021.

[144] Jeongin Moon et al. First Detection of the BAO Signal from Early DESI Data. 4 2023.

[145] Michele Moresco and Federico Marulli. Cosmological constraints from a joint analysis of cosmic growth and expansion. *Mon. Not. Roy. Astron. Soc.*, 471(1):L82–L86, 2017.

[146] Michael J. Mortonson, Wayne Hu, and Dragan Huterer. Falsifying paradigms for cosmic acceleration. Phys. Rev. D, 79(2):023004, January 2009.

[147] Eva-Maria Mueller, Will Percival, Eric Linder, Shadab Alam, Gong-Bo Zhao, Ariel G. Sánchez, Florian Beutler, and Jon Brinkmann. The clustering of galaxies in the completed SDSS-III Baryon Oscillation Spectroscopic Survey: constraining modified gravity. *Mon. Not. Roy. Astron. Soc.*, 475(2):2122–2131, 2018.

[148] J. Muir et al. DES Y1 results: Splitting growth and geometry to test Λ CDM. Phys. Rev. D, 103(2):023528, January 2021.

[149] Nhat-Minh Nguyen, Dragan Huterer, and Yuewei Wen. Evidence for suppression of structure growth in the concordance cosmological model. *arXiv e-prints*, February 2023.

[150] Johannes Noller and Andrina Nicola. Cosmological parameter constraints for Horndeski scalar-tensor gravity. *Phys. Rev. D*, 99(10):103502, 2019.

[151] Teppei Okumura et al. The Subaru FMOS galaxy redshift survey (FastSound). IV. New constraint on gravity theory from redshift space distortions at z ∼ 1.4. PASJ, 68(3):38, June 2016.

[152] Minjoon Park, Kathryn M. Zurek, and Scott Watson. A Unified Approach to Cosmic Acceleration. *Phys. Rev. D*, 81:124008, 2010.

[153] P. J. E. Peebles. The Peculiar Velocity Field in the Local Supercluster. ApJ, 205:318–328, April 1976.

[154] P. J. E. Peebles. *The large-scale structure of the universe*. Princeton University Press, 1980.

[155] P. J. E. Peebles. *Principles of physical cosmology*. 1994.

[156] L. Perenon, S. Ilić, R. Maartens, and A. de la Cruz-Dombriz. Improvements in cosmological constraints from breaking growth degeneracy. A&A, 642:A116, October 2020.

[157] Louis Perenon, Julien Bel, Roy Maartens, and Alvaro de la Cruz-Dombriz. Optimising growth of structure constraints on modified gravity. *JCAP*, 06:020, 2019.

[158] Louis Pèrenon, Federico Piazza, Christian Marinoni, and Lam Hui. Phenomenology of dark energy: general features of large-scale perturbations. J. Cosmology Astropart. Phys., 2015(11):029–029, November 2015.

[159] S. Perlmutter et al. Measurements of the cosmological parameters Omega and Lambda from the first 7 supernovae at z>=0.35. *Astrophys. J.*, 483:565, 1997.

[160] S. Perlmutter et al. Measurements of Ω and Λ from 42 high redshift supernovae. *Astrophys. J.*, 517:565–586, 1999.

[161] Saul Perlmutter and Brian P. Schmidt. Measuring cosmology with supernovae. *Lect. Notes Phys.*, 598:195–217, 2003.

[162] A. Pezzotta et al. The VIMOS Public Extragalactic Redshift Survey (VIPERS): The growth of structure at $0.5 < z < 1.2$ from redshift-space distortions in the clustering of the PDR-2 final sample. *Astron. Astrophys.*, 604:A33, 2017.

[163] M. M. Phillips. The absolute magnitudes of Type IA supernovae. *Astrophys. J. Lett.*, 413:L105–L108, 1993.

[164] Federico Piazza, Heinrich Steigerwald, and Christian Marinoni. Phenomenology of dark energy: exploring the space of theories with future redshift surveys. J. Cosmology Astropart. Phys., 2014(5):043, May 2014.

[165] Levon Pogosian, Marco Raveri, Kazuya Koyama, Matteo Martinelli, Alessandra Silvestri, and Gong-Bo Zhao. Imprints of cosmological tensions in reconstructed gravity. 7 2021.

[166] Levon Pogosian and Alessandra Silvestri. What can cosmology tell us about gravity? Constraining Horndeski gravity with Σ and μ. *Phys. Rev. D*, 94(10):104014, 2016.

[167] David Polarski and Radouane Gannouji. On the growth of linear perturbations. *Physics Letters B*, 660(5):439–443, March 2008.

[168] Athina Pouri, Spyros Basilakos, and Manolis Plionis. Precision growth index using the clustering of cosmic structures and growth data. *JCAP*, 08:042, 2014.

[169] David Rapetti, Chris Blake, Steven W. Allen, Adam Mantz, David Parkinson, and Florian Beutler. A combined measurement of cosmic growth and expansion from clusters of galaxies, the CMB and galaxy clustering. *Mon. Not. Roy. Astron. Soc.*, 432:973, 2013.

[170] Marco Raveri. Reconstructing Gravity on Cosmological Scales. *Phys. Rev. D*, 101(8):083524, 2020.

[171] Marco Raveri, Bin Hu, Noemi Frusciante, and Alessandra Silvestri. Effective Field Theory of Cosmic Acceleration: constraining dark energy with CMB data. *Phys. Rev. D*, 90(4):043513, 2014.

[172] Reinabelle Reyes, Rachel Mandelbaum, Uros Seljak, Tobias Baldauf, James E. Gunn, Lucas Lombriser, and Robert E. Smith. Confirmation of general relativity on large scales from weak lensing and galaxy velocities. *Nature*, 464:256–258, 2010.

[173] Adam G. Riess et al. *Astrophys. J. Lett.*, 934(1):L7, 2022.

[174] Adam G. Riess, William H. Press, and Robert P. Kirshner. A Precise distance indicator: Type Ia supernova multicolor light curve shapes. *Astrophys. J.*, 473:88, 1996.

[175] Adam G. Riess, Wenlong Yuan, Lucas M. Macri, Dan Scolnic, Dillon Brout, Stefano Casertano, David O. Jones, Yukei Murakami, Gagandeep S. Anand, Louise Breuval, Thomas G. Brink, Alexei V. Filippenko, Samantha Hoffmann, Saurabh W. Jha, W. D'arcy Kenworthy, John Mackenty, Benjamin E. Stahl, and WeiKang Zheng. A Comprehensive Measurement of the Local Value of the Hubble Constant with 1 km s^{-1} Mpc^{-1} Uncertainty from the Hubble Space Telescope and the SH0ES Team. *The Astrophysical Journal*, 934(1):L7, July 2022.

[176] Ashley J. Ross et al. The clustering of galaxies in the completed SDSS-III Baryon Oscillation Spectroscopic Survey: Observational systematics and baryon acoustic oscillations in the correlation function. *Mon. Not. Roy. Astron. Soc.*, 464(1):1168–1191, 2017.

[177] Ashley J. Ross, Lado Samushia, Cullan Howlett, Will J. Percival, Angela Burden, and Marc Manera. The clustering of the SDSS DR7 main Galaxy sample - I. A 4 per cent distance measure at z = 0.15. *Monthly Notices of the RAS*, 449(1):835–847, May 2015.

[178] Eduardo J. Ruiz and Dragan Huterer. Testing the dark energy consistency with geometry and growth. Phys. Rev. D, 91(6):063009, March 2015.

[179] Jaime Ruiz-Zapatero, Carlos García-García, David Alonso, Pedro G. Ferreira, and Richard D. P. Grumitt. Model-independent constraints on Ω_m and H(z) from the link between geometry and growth. *Monthly Notices of the RAS*, 512(2):1967–1984, May 2022.

[180] Jaime Ruiz-Zapatero, Benjamin Stölzner, Benjamin Joachimi, Marika Asgari, Maciej Bilicki, Andrej Dvornik, Benjamin Giblin, Catherine Heymans, Hendrik Hildebrandt, Arun Kannawadi, et al. Geometry versus growth. Internal consistency of the flat ΛCDM model with KiDS-1000. A&A, 655:A11, November 2021.

[181] B. Ryden. *Introduction to cosmology*. Cambridge University Press, 1970.

[182] Khaled Said, Matthew Colless, Christina Magoulas, John R. Lucey, and Michael J. Hudson. Joint analysis of 6dFGS and SDSS peculiar velocities for the growth rate of cosmic structure and tests of gravity. *Monthly Notices of the RAS*, 497(1):1275–1293, September 2020.

[183] Valentina Salvatelli, Federico Piazza, and Christian Marinoni. Constraints on modified gravity from Planck 2015: when the health of your theory makes the difference. *JCAP*, 1609(09):027, 2016.

[184] Lado Samushia et al. The clustering of galaxies in the SDSS-III Baryon Oscillation Spectroscopic Survey: measuring growth rate and geometry with anisotropic clustering. *Mon. Not. Roy. Astron. Soc.*, 439(4):3504–3519, 2014.

[185] R. Scaramella et al. Euclid preparation - I. The Euclid Wide Survey. *Astron. Astrophys.*, 662:A112, 2022.

[186] David J. Schlegel et al. A Spectroscopic Road Map for Cosmic Frontier: DESI, DESI-II, Stage-5. *arXiv e-prints*, page arXiv:2209.03585, September 2022.

[187] David J. Schlegel et al. A Spectroscopic Road Map for Cosmic Frontier: DESI, DESI-II, Stage-5. 9 2022.

[188] David J. Schlegel et al. The MegaMapper: A Stage-5 Spectroscopic Instrument Concept for the Study of Inflation and Dark Energy. *arXiv e-prints*, page arXiv:2209.04322, September 2022.

[189] Michael D. Schneider, Óskar Holm, and Lloyd Knox. Intelligent design: On the emulation of cosmological simulations. *Astrophysical Journal*, 728(2), 2011.

[190] D. M. Scolnic et al. The Complete Light-curve Sample of Spectroscopically Confirmed SNe Ia from Pan-STARRS1 and Cosmological Constraints from the Combined Pantheon Sample. ApJ, 859(2):101, June 2018.

[191] Dan Scolnic et al. The Pantheon+ Analysis: The Full Data Set and Light-curve Release. *Astrophys. J.*, 938(2):113, 2022.

[192] Mohit Kumar Sharma and Sourav Sur. Imprints of interacting dark energy on cosmological perturbations. *Int. J. Mod. Phys. D*, 31(03):2250017, 2022.

[193] Alessandra Silvestri, Levon Pogosian, and Roman V. Buniy. Practical approach to cosmological perturbations in modified gravity. *Phys. Rev. D*, 87:104015, May 2013.

[194] Alessandra Silvestri and Mark Trodden. Approaches to understanding cosmic acceleration. *Reports on Progress in Physics*, 72(9), 2009.

[195] Yong-Seon Song and Will J. Percival. Reconstructing the history of structure formation using Redshift Distortions. *JCAP*, 10:004, 2009.

[196] Thomas P. Sotiriou and Valerio Faraoni. f(R) Theories Of Gravity. *Rev. Mod. Phys.*, 82:451–497, 2010.

[197] A. Spurio Mancini, F. Köhlinger, B. Joachimi, V. Pettorino, B. M. Schäfer, R. Reischke, Edo van Uitert, S. Brieden, M. Archidiacono, and J. Lesgourgues. KiDS + GAMA: constraints on horndeski gravity from combined large-scale structure probes. *Mon. Not. Roy. Astron. Soc.*, 490(2):2155–2177, 2019.

[198] Alessio Spurio Mancini, Davide Piras, Justin Alsing, Benjamin Joachimi, and Michael P. Hobson. $CosmoPower$: emulating cosmological power spectra for accelerated Bayesian inference from next-generation surveys. 6 2021.

[199] Masahiro Takada et al. Extragalactic science, cosmology, and Galactic archaeology with the Subaru Prime Focus Spectrograph. PASJ, 66(1):R1, February 2014.

[200] Jesús Torrado and Antony Lewis. Cobaya: code for Bayesian analysis of hierarchical physical models. J. Cosmology Astropart. Phys., 2021(5):057, May 2021.

[201] Tilman Tröster et al. KiDS-1000 Cosmology: Constraints beyond flat ΛCDM. *Astron. Astrophys.*, 649:A88, 2021.

[202] Shinji Tsujikawa. Modified gravity models of dark energy. *Lect. Notes Phys.*, 800:99–145, 2010.

[203] Shinji Tsujikawa. Quintessence: a review. *Classical and Quantum Gravity*, 30(21):214003, November 2013.

[204] Stephen J. Turnbull, Michael J. Hudson, Hume A. Feldman, Malcolm Hicken, Robert P. Kirshner, and Richard Watkins. Cosmic flows in the nearby universe from Type Ia Supernovae. *Mon. Not. Roy. Astron. Soc.*, 420:447–454, 2012.

[205] Michael S. Turner. The Road to Precision Cosmology. 1 2022.

[206] Michael S. Turner and Martin J. White. CDM models with a smooth component. *Phys. Rev. D*, 56(8):R4439, 1997.

[207] Ryan J. Turner, Chris Blake, and Rossana Ruggeri. A local measurement of the growth rate from peculiar velocities and galaxy clustering correlations in the 6dF Galaxy Survey. *Monthly Notices of the RAS*, 518(2):2436–2452, January 2023.

[208] Li-Min Wang and Paul J. Steinhardt. Cluster abundance constraints on quintessence models. *Astrophys. J.*, 508:483–490, 1998.

[209] Sheng Wang, Lam Hui, Morgan May, and Zoltán Haiman. Is modified gravity required by observations? An empirical consistency test of dark energy models. Phys. Rev. D, 76(6):063503, September 2007.

[210] Steven Weinberg. The Cosmological Constant Problem. *Rev. Mod. Phys.*, 61:1–23, 1989.

[211] Yuewei Wen, Eva Nesbit, Dragan Huterer, and Scott Watson. Misinterpreting modified gravity as dark energy: a quantitative study. *JCAP*, 03(03):042, 2022.

[212] Yuewei Wen, Nhat-Minh Nguyen, and Dragan Huterer. Sweeping Horndeski Canvas: New Growth-Rate Parameterization for Modified-Gravity Theories. 4 2023.

[213] Martin White, Rongpu Zhou, Joseph DeRose, Simone Ferraro, Shi-Fan Chen, Nickolas Kokron, Stephen Bailey, David Brooks, Juan García-Bellido, Julien Guy, Klaus Honscheid, Robert Kehoe, Anthony Kremin, Michael Levi, Nathalie Palanque-Delabrouille, Claire Poppett, David Schlegel, and Gregory Tarle. Cosmological constraints from the tomographic cross-correlation of DESI Luminous Red Galaxies and Planck CMB lensing. J. Cosmology Astropart. Phys., 2022(2):007, February 2022.

[214] Puxun Wu, Hong Wei Yu, and Xiangyun Fu. A Parametrization for the growth index of linear matter perturbations. *JCAP*, 06:019, 2009.

[215] Pengjie Zhang. Testing $f(R)$ gravity against the large scale structure of the universe. *Phys. Rev.*, D73:123504, 2006.

[216] Pengjie Zhang, Michele Liguori, Rachel Bean, and Scott Dodelson. Probing Gravity at Cosmological Scales by Measurements which Test the Relationship between Gravitational Lensing and Matter Overdensity. *Phys. Rev. Lett.*, 99:141302, 2007.

[217] Gong-Bo Zhao, Robert G. Crittenden, Levon Pogosian, and Xinmin Zhang. Examining the evidence for dynamical dark energy. *Phys. Rev. Lett.*, 109:171301, 2012.

[218] Gong-Bo Zhao et al. Dynamical dark energy in light of the latest observations. *Nat. Astron.*, 1(9):627–632, 2017.

[219] Gong-Bo Zhao, Tommaso Giannantonio, Levon Pogosian, Alessandra Silvestri, David J. Bacon, Kazuya Koyama, Robert C. Nichol, and Yong-Seon Song. Probing modifications of General Relativity using current cosmological observations. *Phys. Rev.*, D81:103510, 2010.